Project No. 13-4955

Component and Technology Development for Advanced Liquid Metal Reactors

Reactor Concepts

Mark Anderson
University of Wisconsin, Madison

Brian Robinson, Federal POC
Christopher Grandy, Technical POC

NEUP Nuclear Energy University Programs
U.S. Department of Energy

Thermal Hydraulics Laboratory

THL report issued:
January 30, 2017

Report: Final Report for NEUP Project 13-4955

Project Number: NU-13-WI-UWM_-0301-04 (Project 13-4955)

Project Title: Component and Technology Development for Advanced Liquid Metal Reactors

Report Authors: Matthew Weathered, Aidan Boyle, Bryan Coddington, Paul Brooks, Jordan Rein, and Mark Anderson

Technical Point of Contact information:

Mark Anderson, PhD
University of Wisconsin – Madison
Director, Thermal Hydraulics Laboratory
Dept. Engineering Phyiscs
1500 Engineering Dr
Madison WI 53706
608-263-2802
manderson@engr.wisc.edu

TABLE OF CONTENTS

INTRODUCTION

The following report details the significant developments to Sodium Fast Reactor (SFR) technologies made throughout the course of this funding.

This report will begin with an overview of the sodium loop and the improvements made over the course of this research to make it a more advanced and capable facility. These improvements have much to do with oxygen control and diagnostics. Thus a detailed report of advancements with respect to the cold trap, plugging meter, vanadium equilibration loop, and electrochemical oxygen sensor is included. Further analysis of the university's moving magnet pump was performed and included in a section of this report. A continuous electrical resistance based level sensor was built and tested in the sodium with favorable results. Materials testing was done on diffusion bonded samples of metal and the results are presented here as well.

A significant portion of this work went into the development of optical fiber temperature sensors which could be deployed in an SFR environment. Thus, a section of this report presents the work done to develop an encapsulation method for these fibers inside of a stainless steel capillary tube. High temperature testing was then done on the optical fiber ex situ in a furnace. Thermal response time was also explored with the optical fiber temperature sensors. Finally these optical fibers were deployed successfully in a sodium environment for data acquisition.

As a test of the sodium deployable optical fiber temperature sensors they were installed in a sub-loop of the sodium facility which was constructed to promote the thermal striping effect in sodium. The optical fibers performed exceptionally well, yielding unprecedented 2 dimensional temperature profiles with good temporal resolution. Finally, this thermal striping loop was used to perform cross correlation velocimetry successfully over a wide range of flow rates.

SODIUM LOOP OVERVIEW

The sodium facility at the University of Wisconsin-Madison (UW), Figure 1 and Figure 2, was developed throughout the course of this work. Table 1 presents the specifications of the UW sodium loop as of the end of this project funding. Improvement of the oxide control and diagnostics was a major focus throughout the course of this work and will be detailed in subsequent sections.

Figure 1: Developed sodium loop

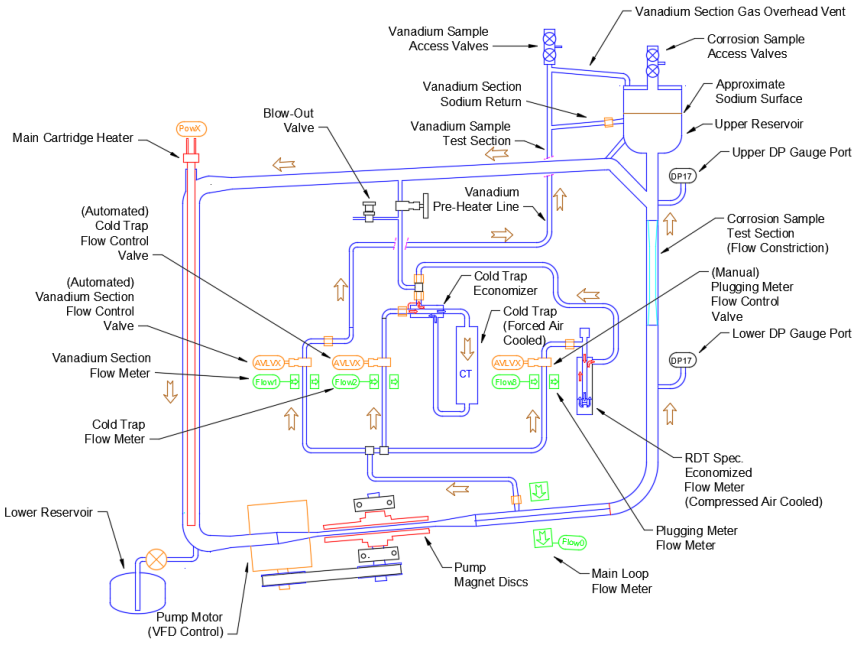

Figure 2: Functional Diagram of Sodium Loop

Table 1: UW Sodium Loop System Specifications

Loop Parameter	Value
Construction Material	316 Stainless Steel
Temperature Range	100-700 [C]
Sodium Loop Volume	7 [L]
Maximum Flow Rate	40 [GPM]
Oxide Control	0.82 [L] Cold Trap
Oxide Level Reading	RDT Spec. Plugging Meter
Pump Type	Moving 24x SmCo Magnets
Heater Types	4 [kW] AC Cartridge 1 [kW] AC Tape Heaters DC Nichrome Heaters
Sodium Flowmeters	3x Permanent Magnet Type

The original loop, Figure 3 provided an excellent foundation from which to construct the improved sodium loop. The original features are detailed thoroughly by Hvasta in his PhD thesis from 2013 [1]. A major revision for the new loop was the exclusion of compression fittings wherever possible. Welding was the new preferred method of construction as operational experience yielded minor sodium leaks at the many Swagelok and Grayloc fittings on the old loop. The only fittings included during construction of the new loop were medium pressure coned and threaded fittings from HIP. These provided satisfactory service at elevated temperature (600C+) but were used sparsely only when frequent connection/disconnection was required. Another modification was the addition of a 4 kW AC cartridge heater to reduce the load on the AC tape and Nichrome wire heaters. It has been labeled in the functional diagram given in Figure 2.

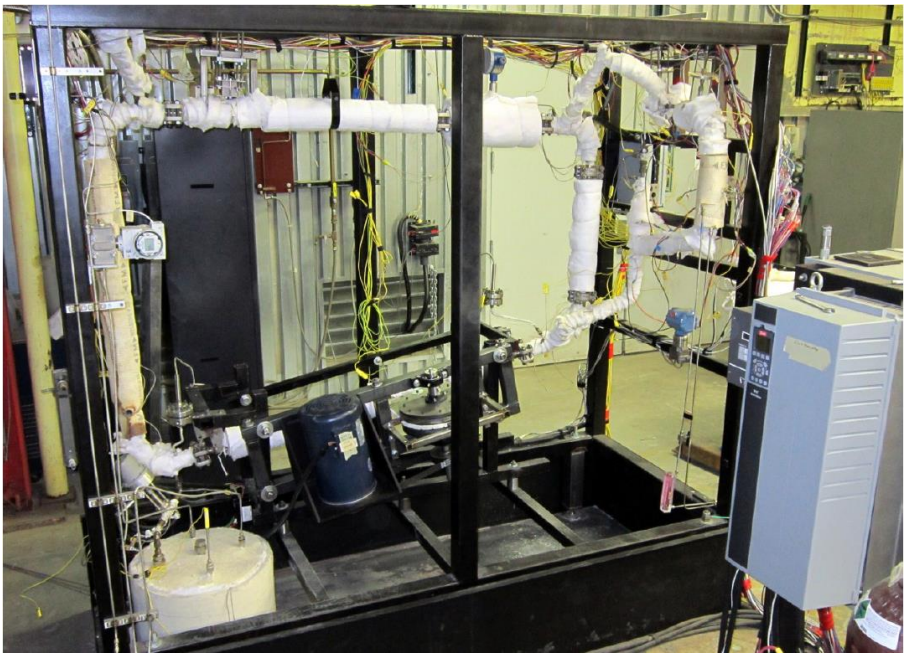

Figure 3: Sodium loop prior to NEUP funding

DIAGNOSTIC LOOP DEVELOPMENT

The following section details the development of the diagnostic loop. The main function of the diagnostic loop is oxygen content control and determination. An overview schematic of the diagnostic loop can be found in Figure 4.

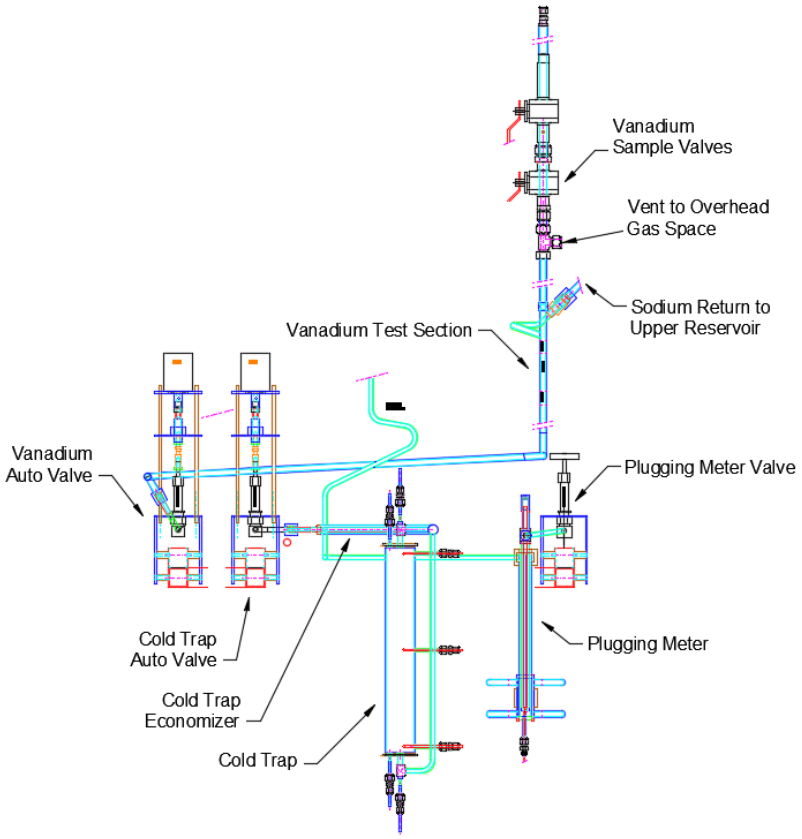

Figure 4: Diagnostic Loop Schematic

Cold Trap

Theory

A cold trap controls the oxide level in a sodium loop by maintaining a lower than loop temperature to promote oxide deposition. This oxide deposition is dictated by the temperature of saturation for the particular oxide level flowing through the loop. This temperature of saturation is defined throughout this work by the RDT F3-40 Standard Correlation, given in Eq. (1). The RDT standard was developed by the DOE and has been used successfully in historical reactors and other sodium tests loops.

$$log_{10}C_O[wppm] = 7.0058 - \frac{2820.1}{T[K]} \qquad (1)$$

Where C_O is the oxide concentration in parts per million by weight and T *the* saturation temperature in Kelvin. The RDT F3-40 oxygen impurity vs sodium temperature in Celsius has been plotted in Figure 5.

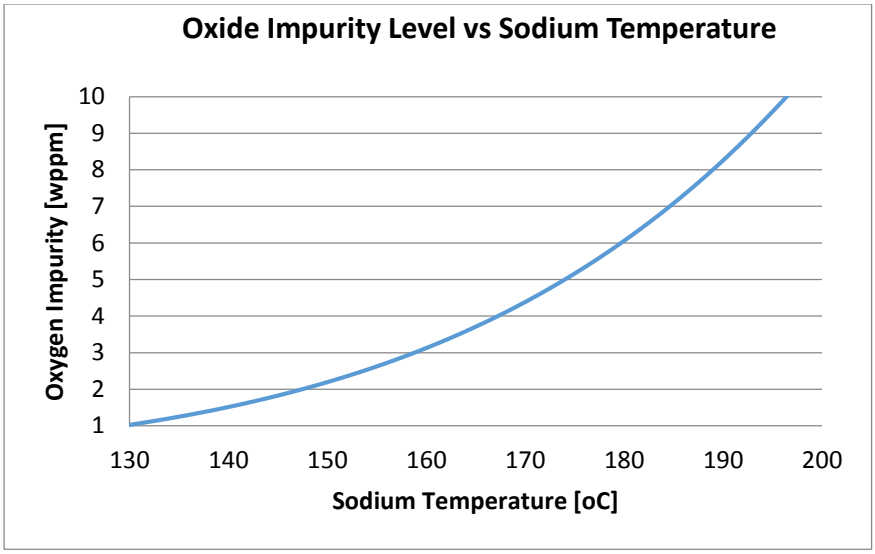

Figure 5: RDT F3-40 Standard Correlation

Usually a cold trap is packed with a stainless steel wool to increase the surface area available for oxide deposition. Typical packing density for packing material has been given in Table 2 [1]

Table 2: Packing material density for cold trap [1]

Packing Material	Packing Density [kg/m^3]	Reference
Steel chips	70-200	[2]
304-SS 30-40 mesh	180-250	[3]
316-SS 4-5 mil wire	320	[4]

Packing material for the cold trap used in this work was chosen as 4 mil 316SS wool with a packing density of 130 kg/m^3. This value falls in the range given in literature from Table 2 and provided a good balance between giving adequate surface area for oxide deposition while allowing sodium to flow easily through the cold trap to prevent plugging.

A minimum residency time of sodium in the cold trap of 5 minutes was achieved with the use of a metering valve on the cold trap line to control flow rate.

Redesign

The cold trap design was modified to improve functionality and reliability. The old design, pictured in Figure 6, flowed sodium from the bottom up and used liquid glycol for cooling. Glycol cooling required a stepper motor to meter sodium flow to control cold trap temperature. This feedback loop proved difficult to control over long periods of time thus oxide levels in loop were more variable. A bottom up flow scheme is not ideal as this creates a stratified cold layer at the top of the cold trap. Buoyancy driven flows begin forming in the cold trap as the denser cold sodium at the top begins to sink due to natural circulation at lower cold trap flow rates.

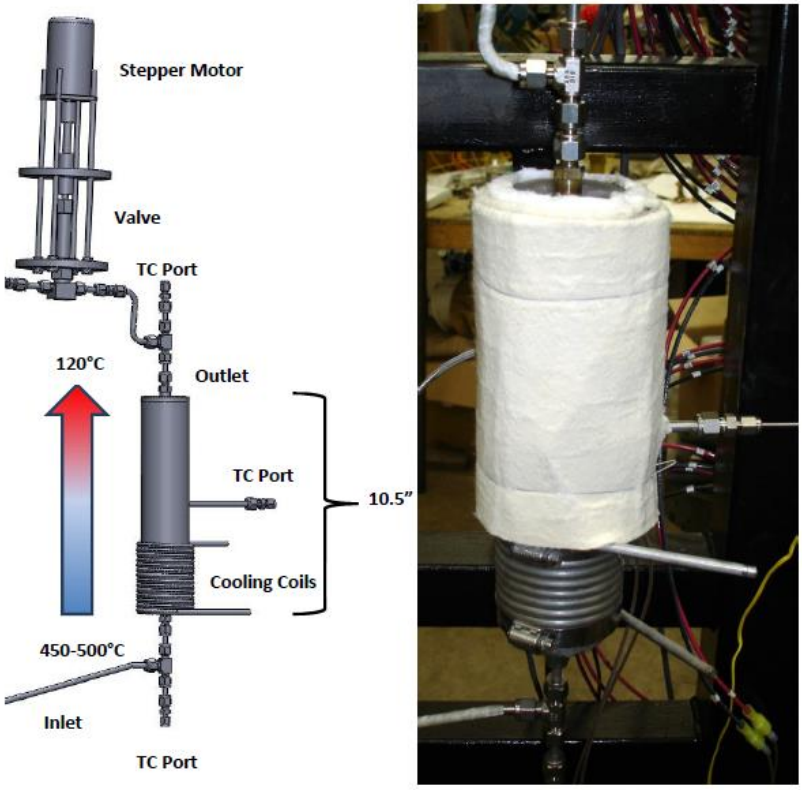

Figure 6: Original cold trap design: [1]

Like the old cold trap, the new cold trap was fabricated from 2" sch 40, 316SS pipe and again contained 316SS wool to increase surface area and promote entrapment of excess sodium oxide from the main loop. In the new design, a concentric tube economizer was placed upstream of the cold trap to both reduce the energy loss in the cold trap, and to allow variable cooling rates. Figure 7 gives a picture of the newly manufactured cold trap. The new cold trap has a downward flow to ensure the cold sodium zone is maintained at the bottom of the cold trap, Figure 8 gives a CAD drawing with the flow scheme labeled. A CAD drawing of the concentric tube economizer has been included in Figure 9. Note that the economizer has a 3.75" radius curvature to reduce thermal expansion stresses at the welded ends.

Figure 7: New cold trap with economizer

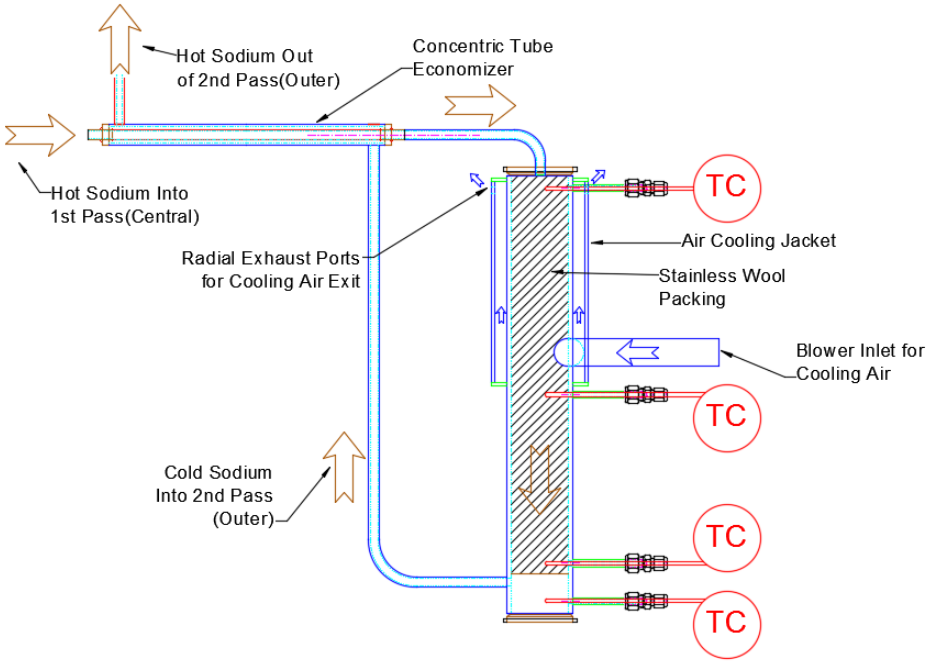

Figure 8: CAD drawing of new cold trap with flow scheme

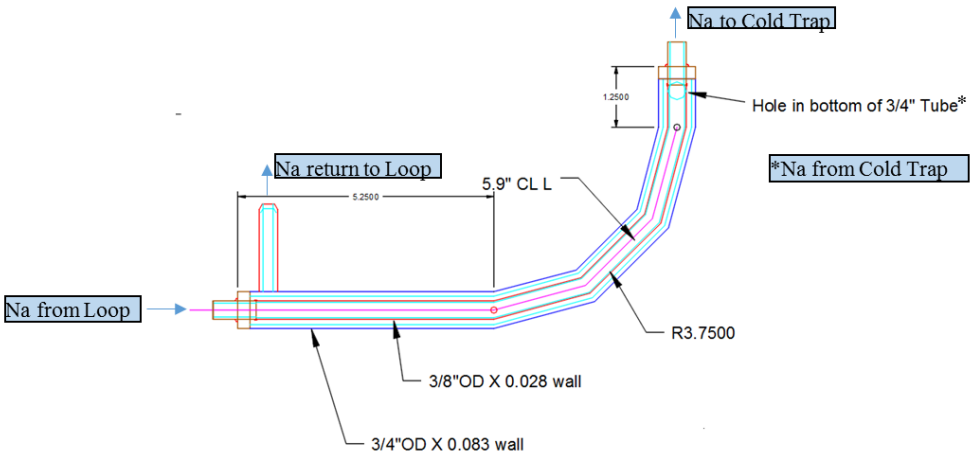

Figure 9: Concentric tube economizer for cold trap

Due to the reduced cooling load, low pressure air could be utilized to control cold trap temperature. A stainless jacket was placed around the upper half of the cold trap (entrance side) to form an annular jacket to direct the air over the exterior of the 2"NPS pipe, Figure 10. Cooling air was forced through this annular path via a blower with a variable frequency drive (VFD) controlled motor. The blower can be seen in front of the rebuilt sodium loop in Figure 1. This frequency output of the VFD (cooling air flow rate) is controlled by a PID within the LabVIEW code referencing the mid-point internal thermocouple in the cold trap.

To minimize axial temperature gradients in the cold trap, a heater tape was placed on the lower half of the cold trap. This was also controlled via a PID within the Labview code referencing the internal thermocouple just above the cold trap exit line. This configuration allows for excellent control of the cold trap temperatures with a minimal temperature gradient. Prior to the cooling jacket occupying half the length of the cold trap a full length cooling jacket was used, as seen on the left side of Figure 10. This created a range of temperature between the bottom and middle thermocouple. Table 3 compares the full length and half-length thermocouple temperature spread at typical operating conditions.

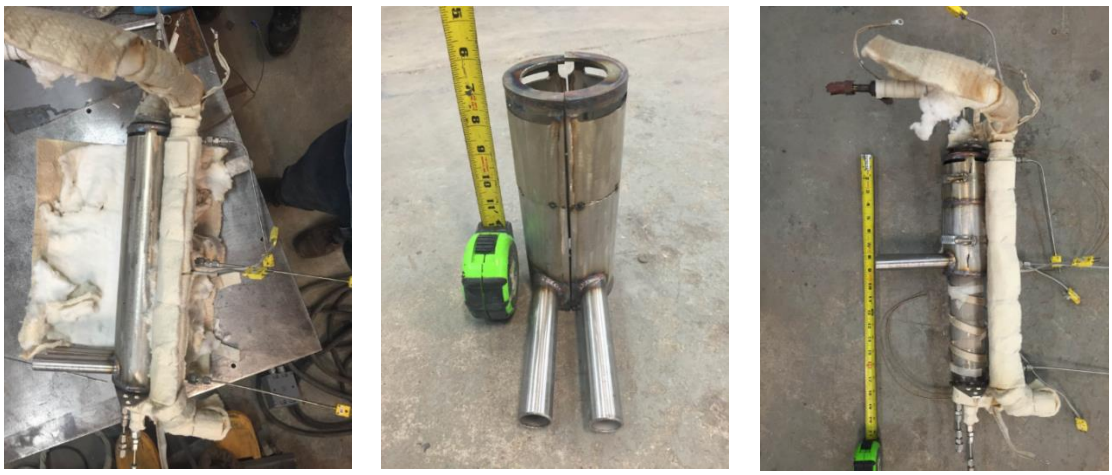

Figure 10: Cooling jacket for cold trap. Left: Original cooling jacket running full length of cold trap. Middle: Cooling jacket shortened. Left: Shortened cooling jacket installed.

Table 3: Cold trap cooling jacket configuration thermocouple temperature spread comparison

Cold Trap Cooling	Full Length Cooled	Top Half Cooled
Loop Temperature	633 C	656 C
Cold Trap Flow Rate	0.047 m/s	0.050 m/s
Top Cold Trap TC	237 C	276 C
Mid Cold Trap TC	221 C	189 C
Btm Cold Trap TC	190 C	189 C
ΔT b/t Lower TCs	31 C	0 C

Figure 11 shows data from 2 optical fiber temperature sensors installed in the cold trap. The cold trap velocity was set to 0.04 m/s with a loop temperature at 650 C. One sensor was installed concentric to the cold trap and another was installed 1/8" away from the inner wall of the cold trap. The fibers run along the axial length of the cold trap tube. The fibers were deployed in 1/32" OD, 0.020" ID 316SS capillary tubes to protect them from the liquid sodium. A more detailed description of the optical fibers can be found in the Optical Fiber Development section of this report.

The fibers provide a 1 dimensional spatial resolution of 2.56 mm thus temperature gradients in the axial direction of the cold trap are very well defined. In order to attain a 2 dimensional contour plot MATLAB was used to define a mesh with a radial and axial resolution of 2.56 mm. The data from the 2 optical fibers was then linearly interpolated to fill in the rest of the mesh. The temperature profile was assumed symmetric thus the data from the left side optical fiber was filled into the mesh on the right side of the cold trap before interpolation. Linear interpolation works well as there is very little temperature gradient in the radial direction due to sodium's low Prandtl number and the narrow geometry of the cold trap.

As can be seen on the left side of Figure 11 temperature data from steady state operation of the cold trap set to 184 C has been included. The cooling section in the top 20 cm of the cold trap cools the sodium down from ~210 C to 184 C by the time it reaches the middle internal thermocouple. The heater section then maintains the sodium at 184 C. This bottom 20 cm is thus isothermal and provides approximately 0.44 L of volume for oxygen deposition. Given the loop contains approximately 7 L of sodium this cold trap to loop volume ratio is approximately 0.06. The middle of Figure 11 shows the 2D temperature distribution of the cold trap operating at a set point of 4 wppm O2. Again, an isothermal zone is developed in the bottom 20 cm of the cold trap for oxide deposition. The rights side of Figure 11 displays the non isothermal nature of the cold trap with the bottom heater zone turned off. This shows the importance of having a separate cooling zone and isothermal zone.

In order to maintain a minimum residency time of 5 minutes within the cold trap, the flow was throttled through a Swagelok 4-UW 316 stainless steel bellows valve. This valve was manually operated and only needed adjustment in the event that the sodium pump speed was drastically changed. The robust nature of this setup is due to the variable cooling delivered by the regenerative air blower and the reduction in inlet sodium temperatures provided by the upstream economizer. Overall, this new cold trap proved a much better system than the previous cold trap in Figure 6.

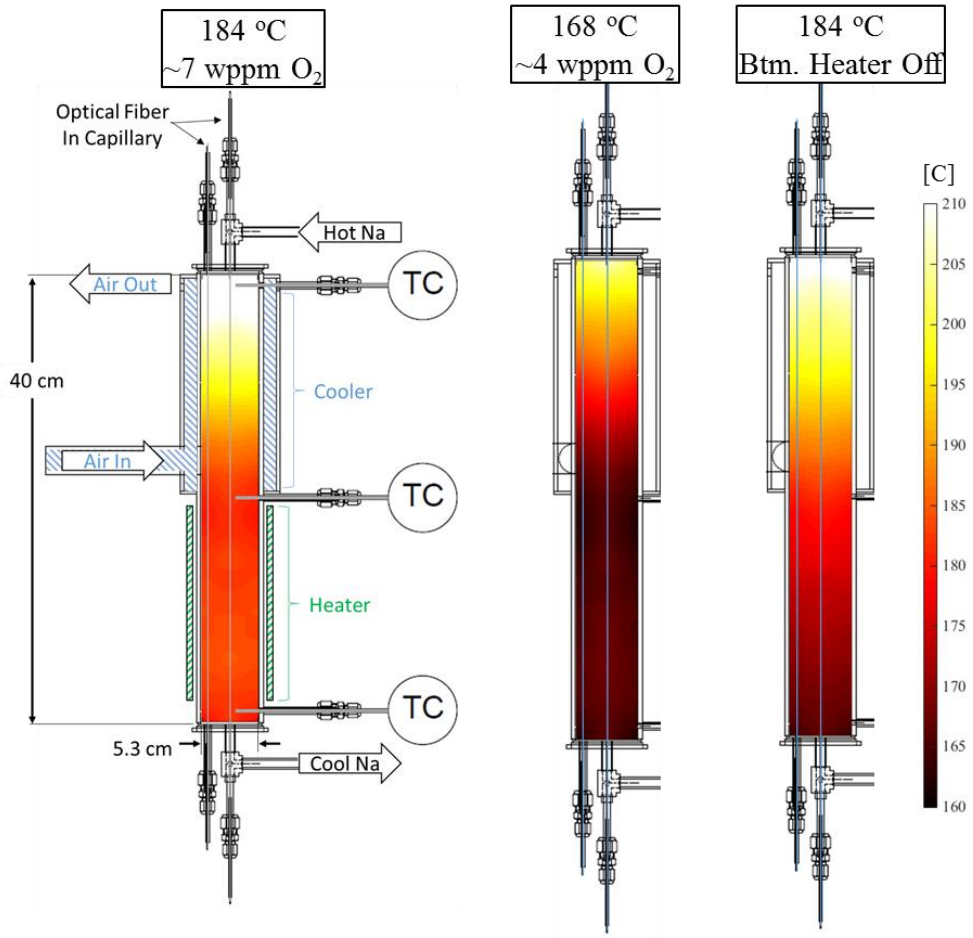

Figure 11: Optical fiber temperature data from cold trap. Left: cold trap set to 184 C. Middle: cold trap set to 168 C. Right: Cold trap set to 184 C with bottom heater off to show non-isothermal gradient.

Computer Model of Economizer

A computational fluid dynamic study was performed using ANSYS CFX on the cold trap economizer to assess its performance. Two simulation cases were assessed with 1.19 g/s and 2.38 g/s chosen as sodium mass flow rates, typical mass flow rates for cold trap velocity in the previous sodium loop. Input parameters and calculated results Inlet sodium temperature to economizer was chosen to be 590°C. Temperature distribution at steady state for 1.19 g/s case can be found in Figure 3. Note that $T_{h,I}$ is defined as the hot sodium coming from loop into economizer, $T_{c,i}$ is defined as the cold sodium coming from the cold trap back into the economizer, $T_{h,o}$ is the sodium from the economizer to cold trap and $T_{c,o}$ is the sodium from the economizer to the loop.

Assuming a perfectly insulated cold trap, one may calculate the amount of power lost by the economizer using Eq. (2).

$$P_{lost} = \dot{m} c_p (T_{h,i} - T_{c,o}) \qquad (2)$$

Where $\dot{m}$ is the sodium mass flow rate and c_p is the sodium specific heat. Results for power lost by economizer for each simulation can be found in Table 4. The actual average power

transferred between the two fluids in the economizer can be calculated using Eq. (3) and the corresponding optimal heat transfer for this case can be solved using Eq. (4). Eqs. (3) and (4) can then be used to calculate the effectiveness of the economizer, ε, using Eq. (5).

$$P_{actual} = \dot{m} c_p (T_{h,i} - T_{h,o}) \quad (3)$$

$$P_{optimal} = \dot{m} c_p (T_{h,i} - T_{c,i}) \quad (4)$$

$$\varepsilon = \frac{P_{actual}}{P_{optimal}} \quad (5)$$

Table 4: ANSYS CFX parameters and results for cold trap economizer simulation

Input Parameters	***Simulation 1***	***Simulation 2***	***Units***
Sodium Inlet Velocity	0.02	0.04	*[m/s]*
Mass Flow Rate	0.00119	0.00238	*[kg/s]*
Na Specific Heat	1289.92		*[J/kg K]*
Na Density	864.6347		*[kg/m³]*
Na Conductivity	71.175		*[W/m K]*
Na Viscosity	2.93E-4		*[Pa s]*
$T_{h,i}$	590		*[C]*
$T_{c,i}$	147.4		*[C]*
Calculated Results	***Simulation 1***	***Simulation 2***	***Units***
$T_{h,o}$	178.407	187.266	*[C]*
$T_{c,o}$	582.321	586.743	*[C]*
P_{lost}	11.7873	9.99899	*[W]*
P_{actual}	631.795	1236.39	*[W]*
$P_{optimal}$	679.391	1358.78	*[W]*
Effectiveness	0.92994	0.90993	*[-]*

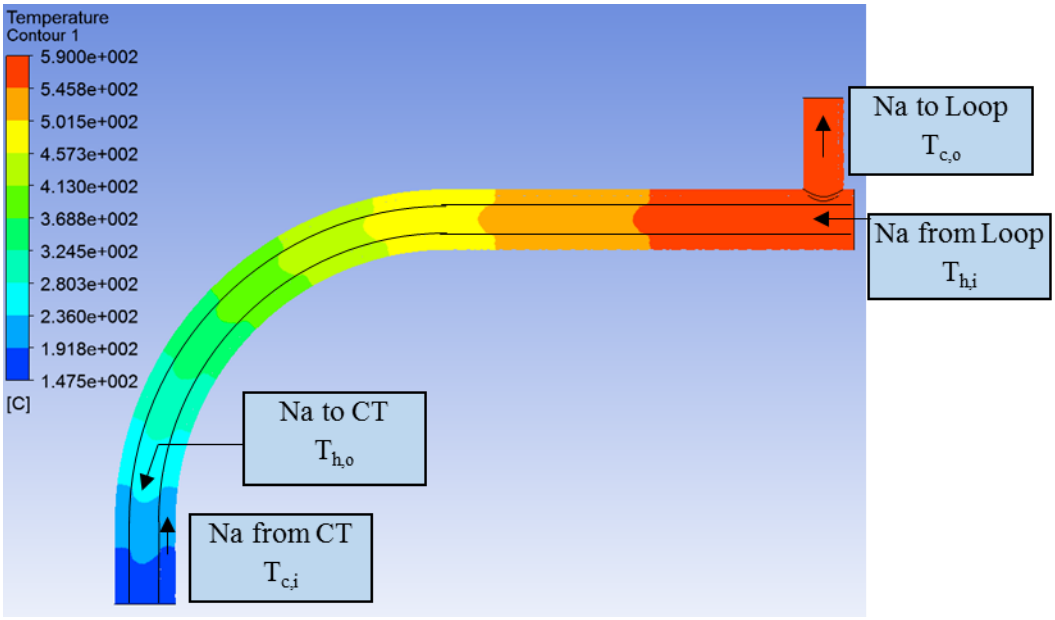

Figure 12: Simulation 1 steady state temperature of cold trap economizer

Plugging Meter

Design

A new plugging meter was designed and built to follow the RDT E 4-19T standard and specifications, Figure 13 [5]. This allows for easy comparison to plugging meters from literature with this design and to base operating procedure off of Reactor Development and Technology protocol. This plugging meter improved upon the original design, Figure 14, in a few key ways. Most importantly, the RDT design is economized, thus allowing for more precise control of sodium cooling rate. The economizer reduced the propensity for oxide particles to plate out prior to reaching the orifice plate. Additionally, an economized design reduces heating losses in the loop. Another key feature of the RDT design is a clearing pin which allows the user to easily clear a plugging orifice. A picture of the bottom of the clearing pin, inner tube which separates the 2 flow streams in the economizer and 2 plugging orifices can be found in Figure 15. Notice the central hole in the plugging orifice which provides a seat for the beveled clearing pin to rest in during standard operation. The orifice plate and clearing pin dimensions were taken directly from the RDT standard on plugging temperature indicators. A drawing from the RDT standard for orifice plate dimensions can be found in Figure 16 [5].

During testing sodium enters the plugging meter and runs down the central annulus towards the orifice plate. Once through the orifice plate the sodium turns 180° and runs up the outer annulus then exiting the plugging meter. Compressed air is supplied to the air cooling jacket to facilitate cooling of the sodium passing through the orifice plate to below the oxide saturation temperature. This air supply is metered by a Jordan control valve, Figure 17, to provide precise temperature control at the orifice plate which is measured by a calibrated, sodium wetted 1/16” stainless steel sheathed K-type thermocouple.

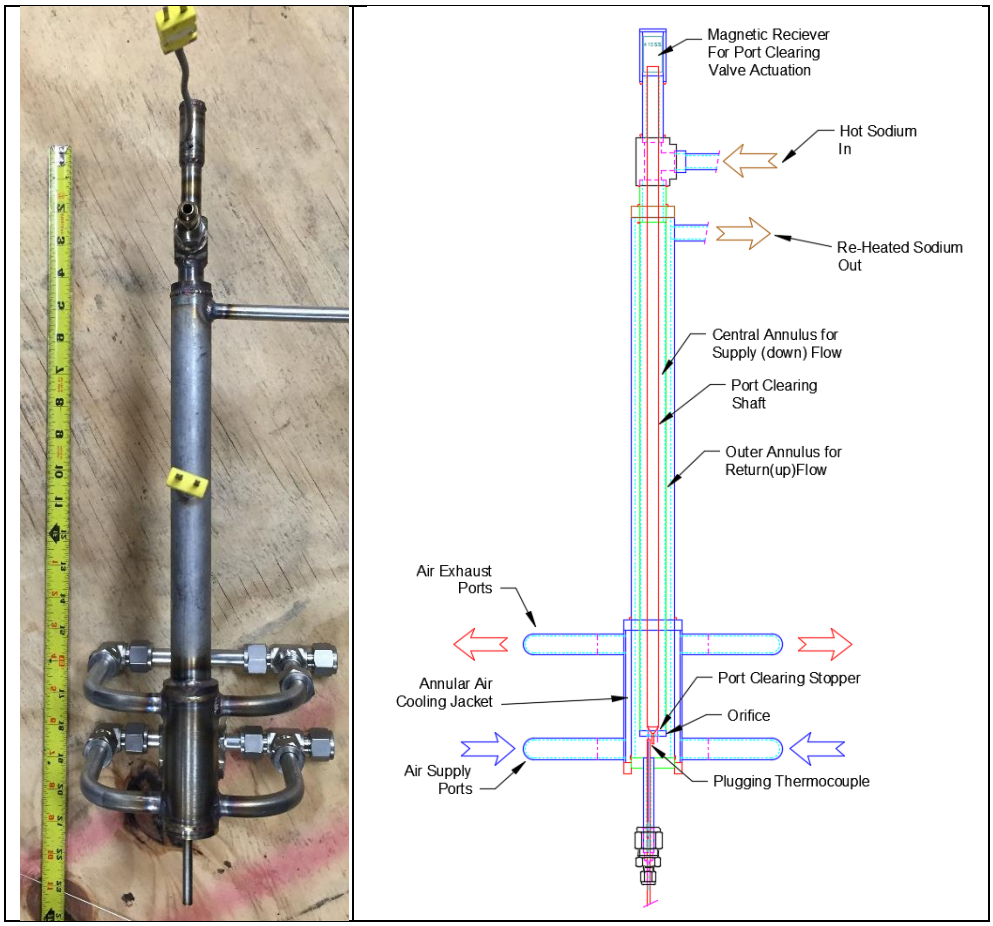

Figure 13: Plugging meter designed to RDT specification

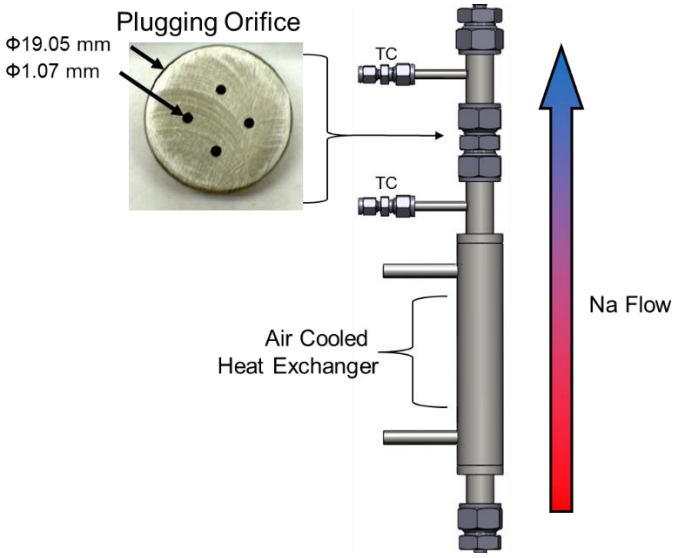

Figure 14: Old plugging meter design

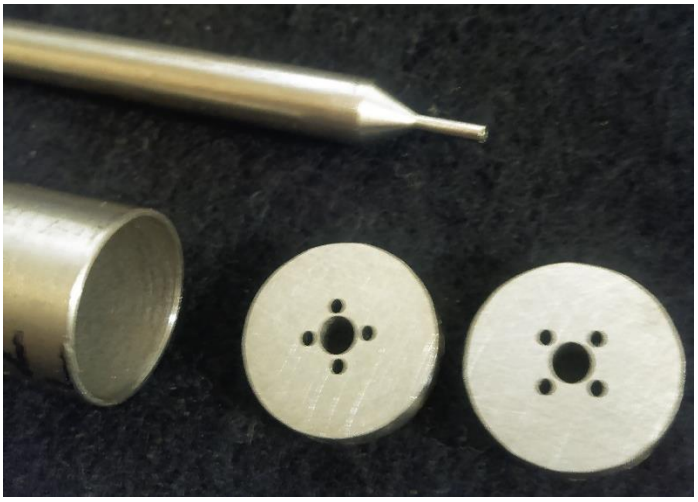

Figure 15: Hot/cold sodium interface tube, clearing pin, and 2 plugging orifices

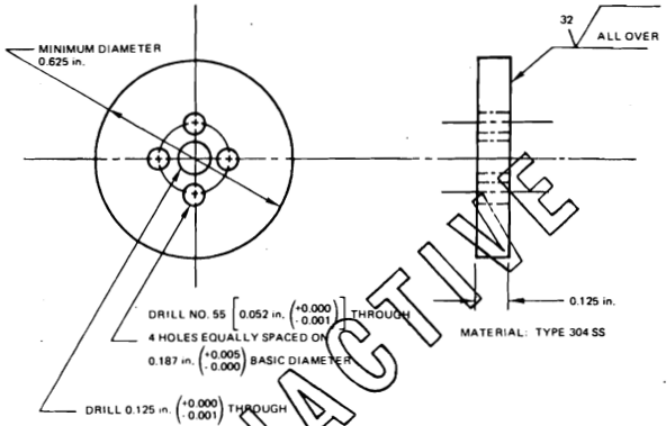

Figure 16: RDT Standard plugging orifice [5]

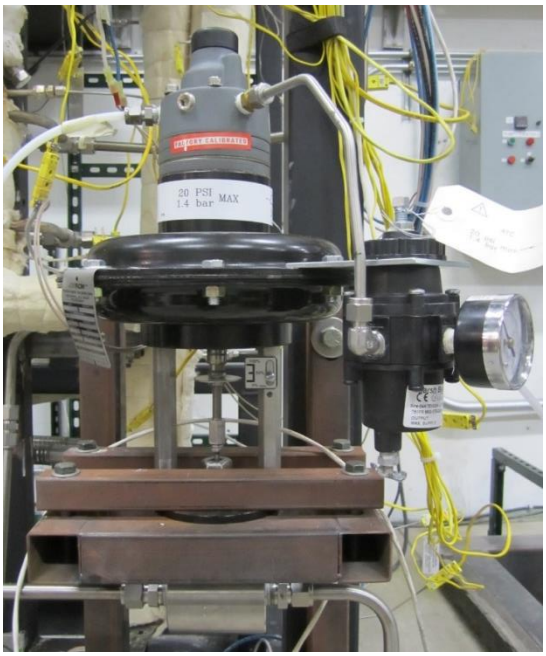

Figure 17: Pressurized air control valve

Computer Simulation

The plugging meter height was determined based on ANSYS CFX analysis to maximize economizer efficiency. Cooling jacket dimensions were also based on ANSYS CFX calculations to maximize efficiency and provide the cooling necessary for low oxide concentration testing. The parameters used for the ANSYS CFX computer simulation have been given in Table 5. Note that the values used in the table for material properties were taken for 370°C; this temperatures was chosen as it is halfway between the 590°C inlet temperature and 147.5°C saturation temperature of sodium at 2 wppm oxygen concentration.

A sodium inlet temperature of 590 C was used which is a typical sodium temperature when the main loop is operating at 650 C. A typical sodium inlet velocity of 0.045 m/s was used. The inlet boundary condition for the pressured air heat exchanger was set to 25 C air at 30 PSIG. In practice the pressurized air inlet may be set as high as 80 PSIG, limited by the air compressor. A drawing of the simulation geometry can be found in Figure 18.

Table 5: Parameters for plugging meter computer simulation

Parameter	***Input***	***Ref***
Sodium Inlet Temperature	**590 [C]**	-
Sodium Inlet Mass Flow Rate	0.00254 [kg/s]	-
Sodium Inlet Velocity	**0.045 [m/s]**	-
Air Inlet Temperature	25 [C]	-
Air Inlet Pressure	30 [PSIG]	-
Sodium Density	864.6347 [kg/m3]	[1]
Sodium Specific Heat	1289.916 [J/kg K]	[1]
Sodium Thermal Conductivity	71.175 [W/m K]	[1]
Sodium Dynamic Viscosity	2.93E-4 [Pa s]	[1]

Air Density	1.185 [kg/m3]	*
Air Specific heat	1004.4 [J/kg K]	*
Air Thermal Conductivity	2.61E-2 [W/m K]	*
Air Dynamic Viscosity	1.831E-5 [Pa s]	*
SS-316 Density	7811.82 [kg/m3]	*
SS-316 Specific Heat	551.36 [J/kg K]	*
SS-316 Thermal Conductivity	18.165 [W/m K]	*
*Default ANSYS Workbench Values		

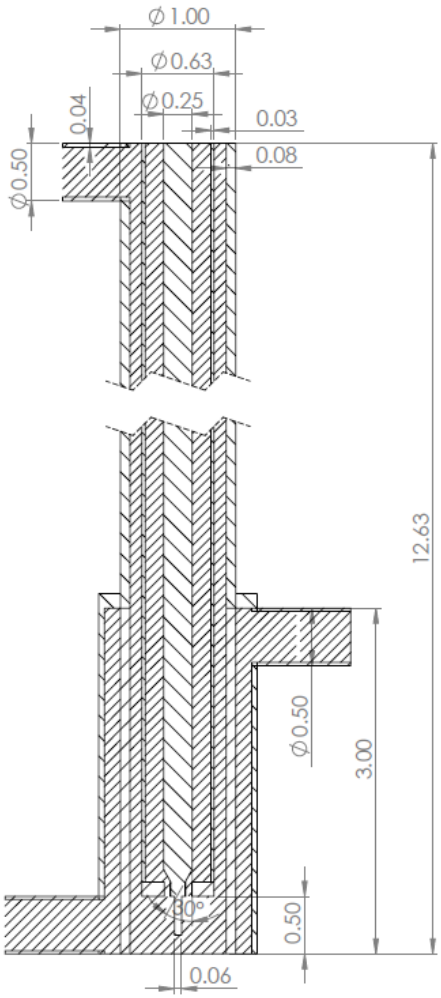

Figure 18: Drawing of plugging meter ANSYS simulation geometry

Results from the computer simulation can be found in Figure 19. The transient simulation was run for a period of 120 sec, results for the 120 sec time step can be found on the left side of Figure 19. At this time the sodium reached a temperature of approximately 380 C at the plugging orifice. Given a constant cooling time a plugging period of 300 seconds should be expected for these particular system conditions. Note that the air inlet pressure may be increased to speed up

plugging turnaround times. A steady state solution was found and the temperature profile can be found on the right side of Figure 19. Note that temperatures of 45 C were found at steady state, thus if the plugging meter were to be run in a steady state operation, just above plugging temperature, the regulator dictating air inlet pressure may be lowered to increase efficiency. This would reduce air compressor workload.

120 Seconds into Plugging Test:

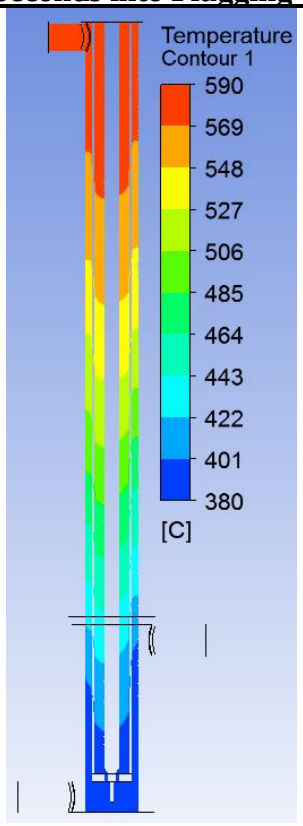

Steady State Plugging Meter:

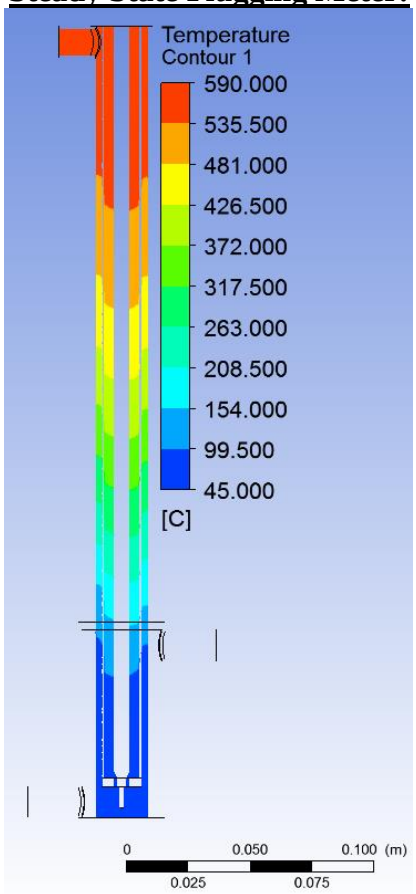

Figure 19: Plugging meter, transient at 120 seconds and steady state temperature solution

Plugging Meter Operation

A plugging meter operation procedure was created over the period of this work which was based off of RDT protocol. Typical parameters for running the plugging meter have been included in Table 6. A typical run procedure of the plugging meter with 10 wppm O2 loop concentration has been included in Figure 20 for reference.

Table 6: Plugging meter testing parameters

	Low Flow	High Flow
PM Velocity (m/s)	0.127	0.405
Sub cool (C)	20	20
Trip Velocity – Low (m/s)	0.035	0.150
Quick heat (C)	10	10
Trip Velocity – High (m/s)	0.070	0.220
Heat Rate (C/min)	3	3
Loop Temperature (C)	650	350

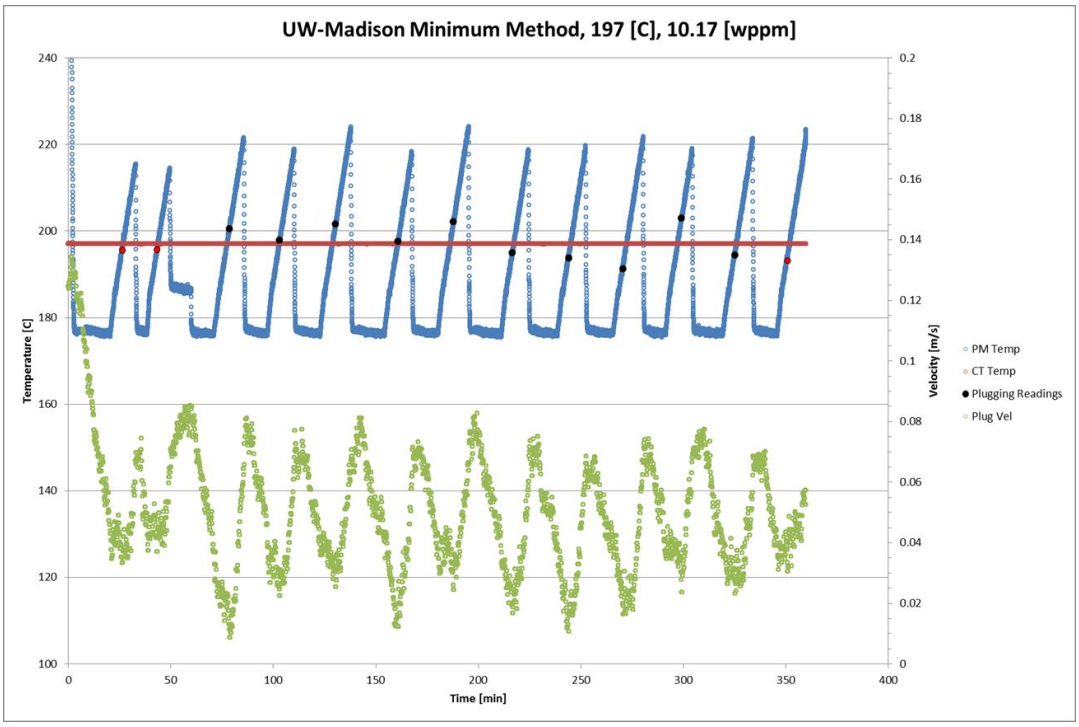

Figure 20: Typical operation of plugging meter at 10 wppm O2 loop concentration

Electrochemical Oxygen Sensor

A continuous electrochemical oxygen sensor was created based on the yttria stabilized zirconia design featuring a copper/copper oxide electrode by Nollet [6]. The new design features an yttria stabilized zirconia (YSZ) tube inside of a stainless steel sheath. A custom stainless steel piece was machined to create a graphite seal inside of a swage to separate the sodium loop from the YSZ tube opening and a system of swages were used to separate the electrode atmosphere from the outside (Figure 21). The stainless steel sheath was chosen to be 13 inches to insure a sodium freeze seal would occur as a backup to the graphite seal. A cage was welded onto the bottom of the sensor sheath that would allow contact with liquid sodium, but also catch YSZ fragments if the sensor were to break due to thermal shock.

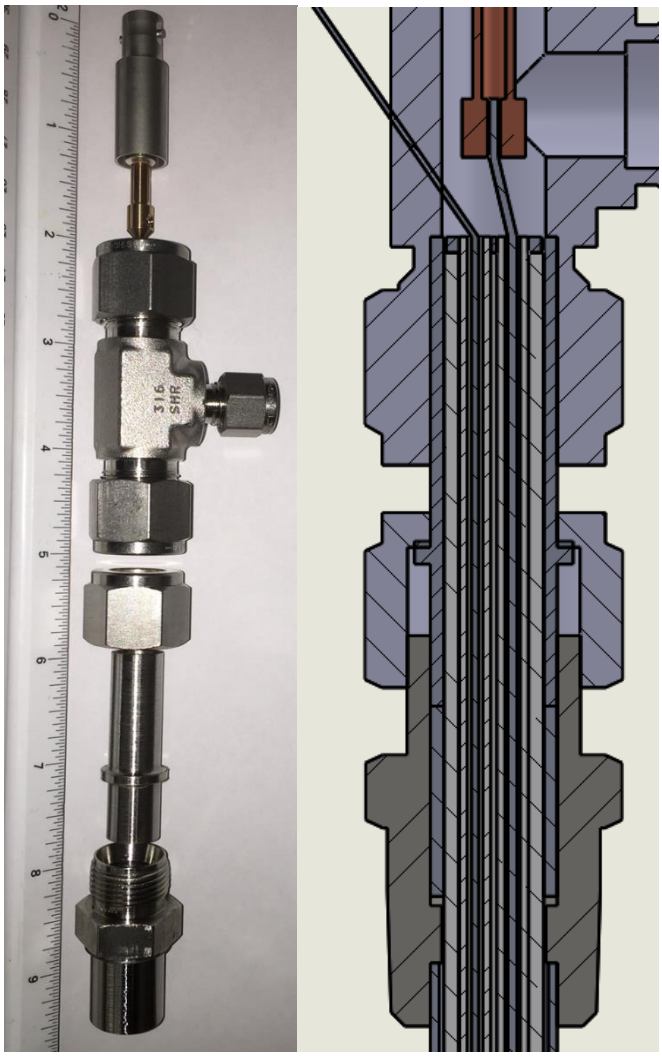

Figure 21: Wire Coupling and Homemade Graphite Seal

Rather than using a copper/copper oxide electrode, an indium/indium oxide mixture was chosen (Figure 23). This mixture is a liquid at operating temperatures, which it was hoped would allow for more consistent results across different sensors. Molybdenum was chosen for the sensor wire as it is stable in indium. Because there was an intersection of dissimilar metals, the Seebeck effect was an important consideration. An internal thermocouple was placed inside of the YSZ tube inside of an alumina sheath to allow for accurate temperature measurements of the electrode to correct for the Seebeck effect (Figure 22). Alumina spacers were used to keep the molybdenum wire isolated from the thermocouple. An argon cover gas was used over the electrode so that there was a known quantity of oxygen in the indium mixture.

Figure 22: Molybdenum Wire and Internal Thermocouple with Alumina Spacers

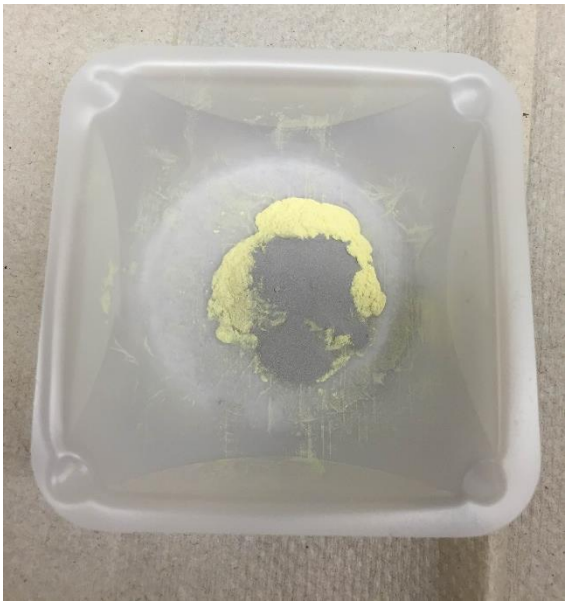

Figure 23: Indium/Indium Oxide Mixture Prior to Filling Sensor Electrode

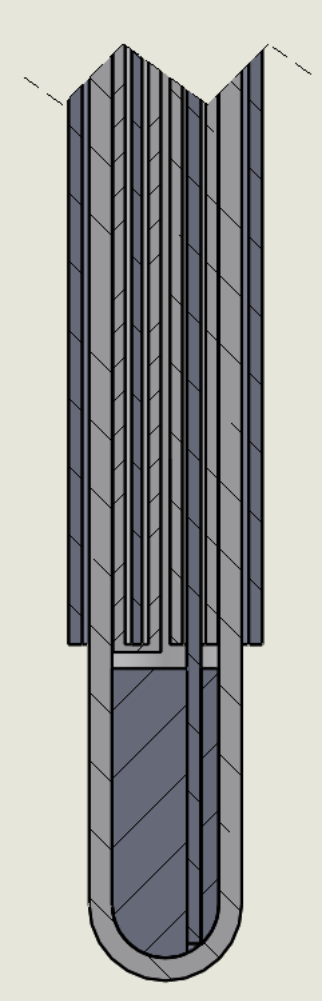

Figure 24: Drawing of electrode section of oxygen sensor. Molybdenum wire is the only piece in contact with indium mixture

The oxygen sensor was placed into the upper reservoir of the sodium loop prior to the sodium fill as seen in Figure 25. The temperature of the loop and the upper reservoir were slowly brought to match the fill temperature of 250C. It was necessary to have the sensor match the sodium temperature as closely as possible to minimize the risk of failure due to thermal shock. When the temperatures matched closely, the loop was filled with sodium.

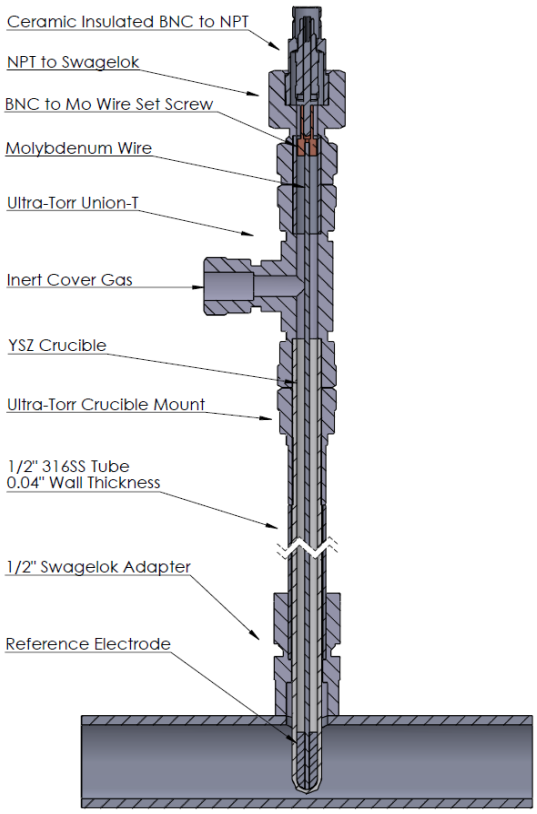

Figure 25: Complete drawing of electrochemical oxygen sensor in loop

The oxygen content of the loop was changed by altering the temperature of the cold trap. The oxygen sensor showed a response to changes in oxygen that can easily be seen when the oxygen concentration is changed drastically (2ppm to 10ppm), but the change in voltage is smaller than what is predicted by theory. This change becomes much harder to resolve for changes of 2ppm. In addition, the voltage of the sensor is reading higher than what is predicted by theory, and it is further increasing over time. 170 hours of oxygen sensor testing can be seen in Figure 26

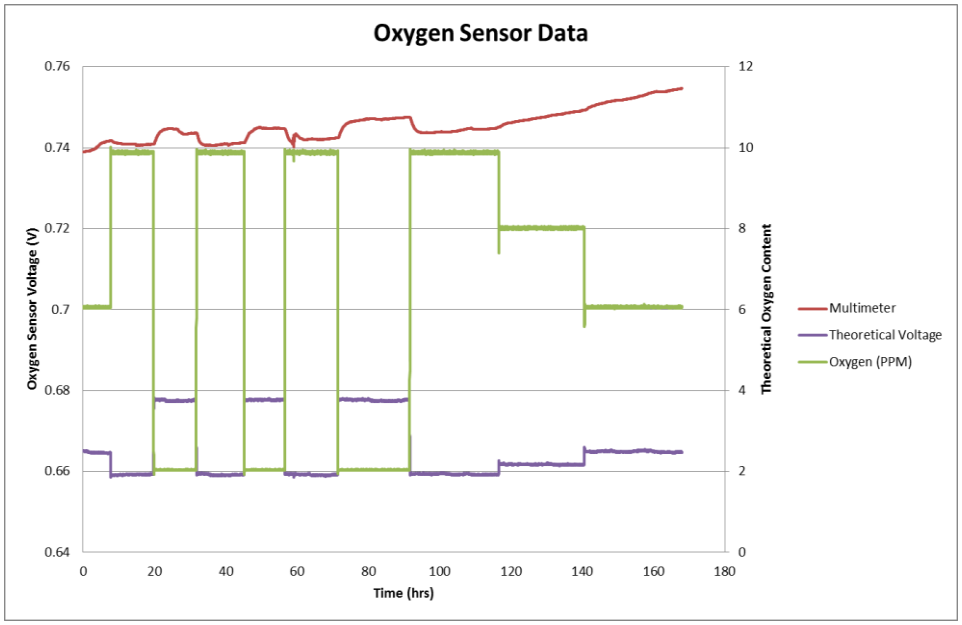

Figure 26: Electrochemical sensor data

Taylor and Thompson [7] saw similar increases in voltage over time, and found that intergranular penetration of the sensor was responsible for the changes.

Vanadium Equilibration

Measurement of the oxygen content of the sodium was attempted using the vanadium equilibration method. Vanadium, being a strong oxygen getter, will pull oxygen out of the sodium until equilibrium is reached. The vanadium can be removed from the loop, and various methods can be used to measure the oxygen concentration of the vanadium.

The conversion from vanadium oxygen concentration to sodium oxygen concentration can be done by starting with

$$\frac{a_{o-v}}{a_{o-na}} = \frac{a_{osat-v}}{a_{osat-na}} * e^{\frac{F_{Na_2O}-F_{V_5O}}{RT}}$$

Where a is the activity of the oxygen in the materials and F is the free energy of formation of different molecules. Note that

$$a_i = y_i * N_i$$

Where y is the activity coefficient and N is the atom fraction. Substitute into the first equation to get

$$\frac{y_{o-v}}{y_{o-na}}\frac{N_{o-v}}{N_{o-na}} = \frac{y_{osat-v}}{y_{osat-na}}\frac{N_{osat-v}}{N_{osat-na}} * e^{\frac{F_{Na_2O}-F_{V_5O}}{RT}}$$

Note that F for V_5O are unavailable so exponential must be determined experimentally

At small concentrations, this obeys raoults law so

$$K_A = \frac{N_{o-v}}{N_{o-na}} = \frac{N_{osat-v}}{N_{osat-na}} * e^{\frac{F_{Na_2O}-F_{V_5O}}{RT}}$$

It was experimentally determined from Smith's figure 3 and 4 below that

$$\ln(N_{osat-v}) = -1.89 - \frac{1210}{T}$$

Where saturation is determined to be at the point of onset of V_5O protective layer

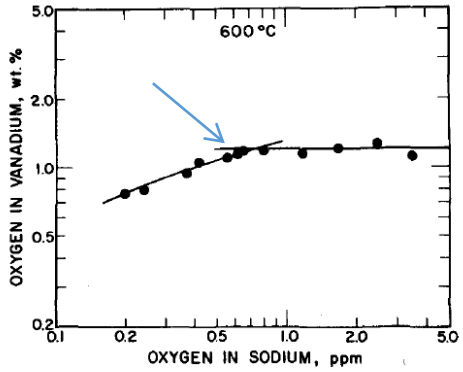

Fig. 3—Measured oxygen concentration in vanadium after exposure to sodium with various oxygen concentrations.

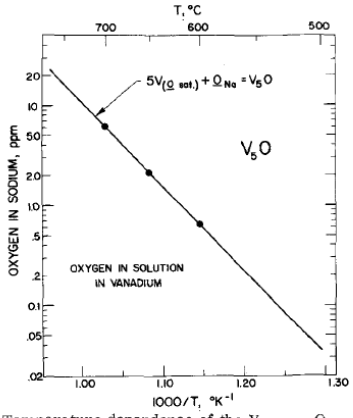

Fig. 4—Temperature dependence of the $V_{(\underline{O}\ sat)} - \underline{O}_{Na} - V_5O$ equilibrium.

At saturation, the third equation can be reduced to

$$1 = \frac{y'_{o-Na}}{y_{osat-na}} \frac{N'_{o-na}}{N_{osat-na}} * B$$

Where B is the value of the exponential at a given temperature and y' and N' are values for oxygen in sodium at vanadium saturation. Using this it can be seen that

$$\frac{y_{o-v}}{y_{osat-v}} = \frac{N_{o-Na}}{N'_{o-na}} \frac{N_{osat-v}}{N_{o-v}} = \frac{N_{osat-v}}{N'_{o-na}} \left(\frac{1}{K_A}\right)$$

Using saturation values determined experimentally (above) we get

$$\frac{y_{o-v}}{y_{osat-v}} = \left(\frac{1}{K_A}\right) * e^{-9.567+17560*\left(\frac{1}{T}\right)}$$

Taking y_{osat-v}=1 this simplifies to

$$\ln(y_{o-v}) = 17560 * \left(\frac{1}{T}\right) - 9.567 - \ln(K_A)$$

A second equation for y_{o-v} was experimentally determined from Figure 27 obtained from Smith [X].

$$\ln(y_{o-v}) = -\frac{30070}{T}[(1 - N_{o-v})^2 - (1 - N_{osat-v})^2]$$

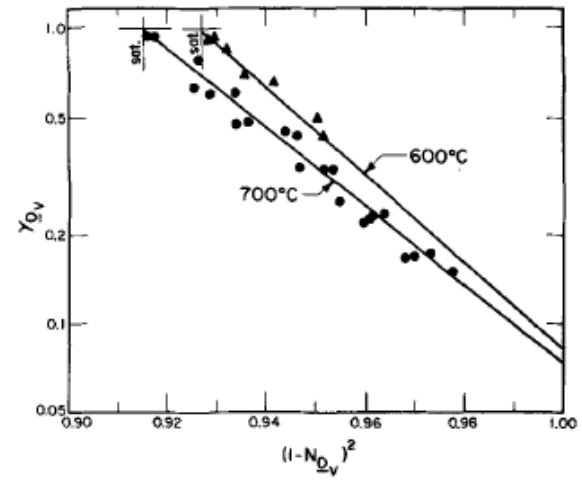

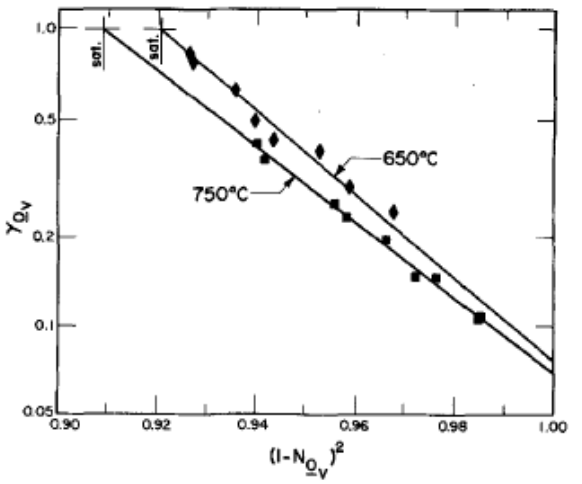

Figure 27: Plots of y

Combining the two equations above and solving for K_A gives us

$$\ln(K_A) = \{17560 + 30070[(1 - N_{o-v})^2 - (1 - N_{osat-v})^2]\}\left(\frac{1}{T}\right) - 9.567$$

Where K_A is the ratio of oxygen concentration of vanadium over that of sodium. Note that this ratio loses meaning when above the onset of V_5O protective layer, which is temperature dependent. To measure higher oxygen concentrations, it is necessary to go to higher temperatures. It is easy to tell when this limit has been exceeded because a brittle black layer forms on the sample which falls off during post test cleaning.

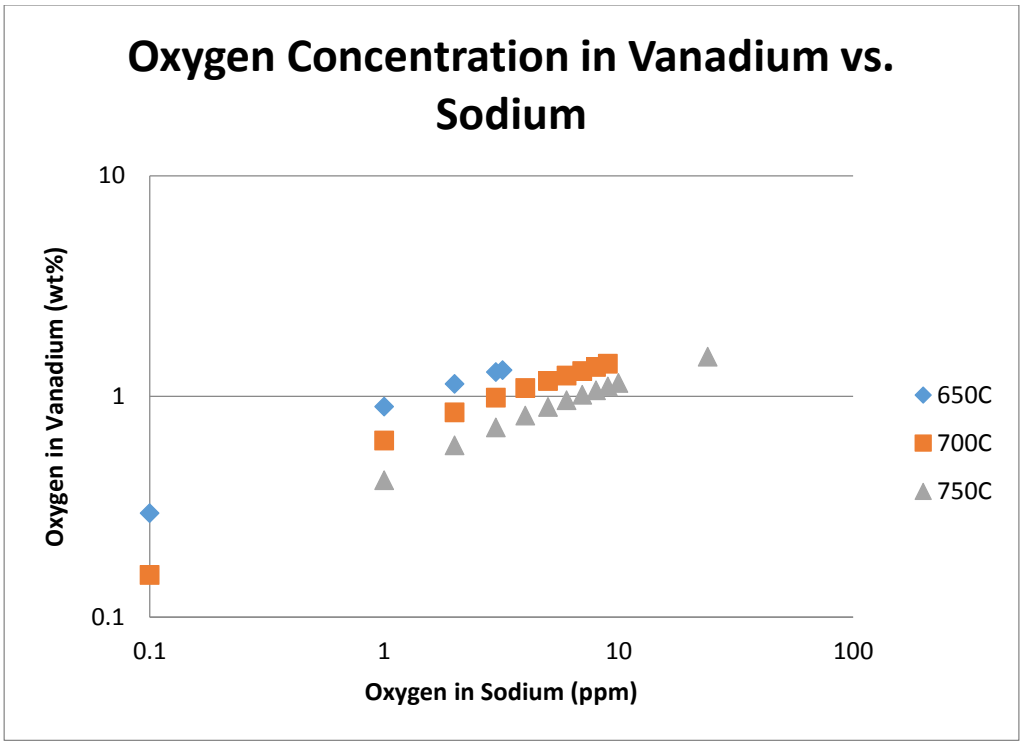

Several vanadium samples have been tested in varying oxygen contents in the sodium. Samples were cleaned in ethanol prior to testing. Samples were weighed before and after testing and the weight change was compared when possible. A thin layer was electropolished off using the method described in Smith [Z]. Samples were sent for inert gas fusion testing to determine the oxygen content of the vanadium.

Initial vanadium equilibration testing was done with 0.04 inch wires. After several tests, it was determined that equilibrium in the samples was not being reached. To solve this problem, testing with thinner 0.01 inch wires has begun.

Table 7: Results from 0.04 in vanadium wire testing

Sample #	Test Fluid	PPM Level	Test Time	Temperature	Expected Oxygen Weight %	Mass reading Oxygen Weight %	IGF Oxygen Weight %
1	Gas	62.2	24 Hours	905C	1.161	Negative	0.0135
2	Sodium	6	8 Hours	714C	1.162	0.237	0.41
3	Sodium	6	8 Hours	714C	1.162	0.257	0.304
4	Sodium	4	8 Hours	697C	1.109	0.246	0.367
5	Sodium	4	18 Hours	697C	1.109	0.254	0.724
6	Sodium	3	18 Hours	695C	1.01	Negative	NA
7	Sodium	2	18 Hours	695C	0.8753	Negative	NA

The first test of the 0.01 inch wire was done at 10 ppm and 714C. Inert gas fusion of this sample shows an oxygen content of 1.53 wt% compared to an expected value of 1.375 wt%. The

measured value corresponds to an oxygen concentration of 14 ppm in the sodium. The value is higher than expected, but does indicate that the sample reached an equilibrium concentration with the sodium.

MOVING MAGNET PUMP DEVELOPMENT

Pump Curves

Pump curves were acquired for the UW moving magnet pump (MMP) at a variety of system conditions. A graphite packed gate valve was installed in the main loop of the sodium facility to adjust pressure drop across the MMP duct. Differential pressure across the pump duct and corresponding flow rate was recorded for a variety of pump speeds and loop temperatures. The permanent magnet flowmeters used to record flow rate were previously calibrated with a vortex shedding flowmeter [1]. The diagnostic loop was valved off throughout this work. Pump curves are found in Figure 29.

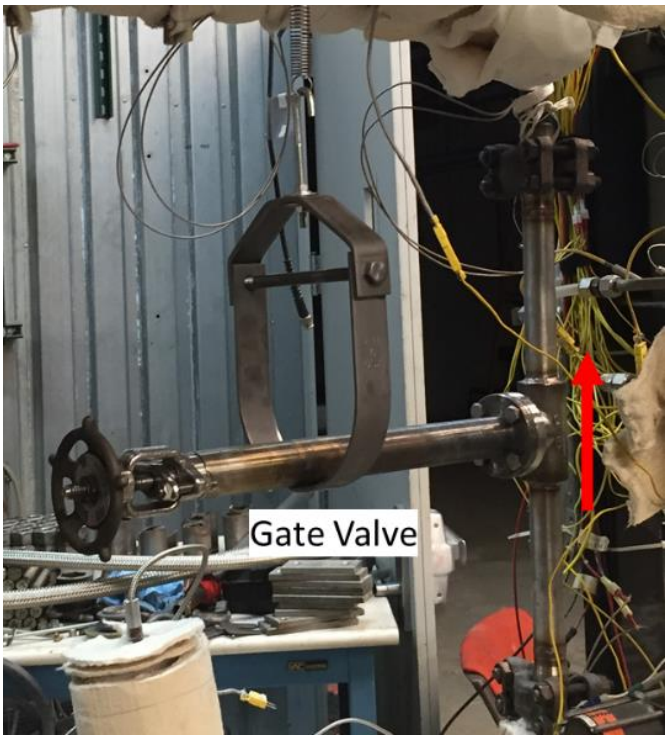

Figure 28: Gate valve installed for MMP pump curve acquisition

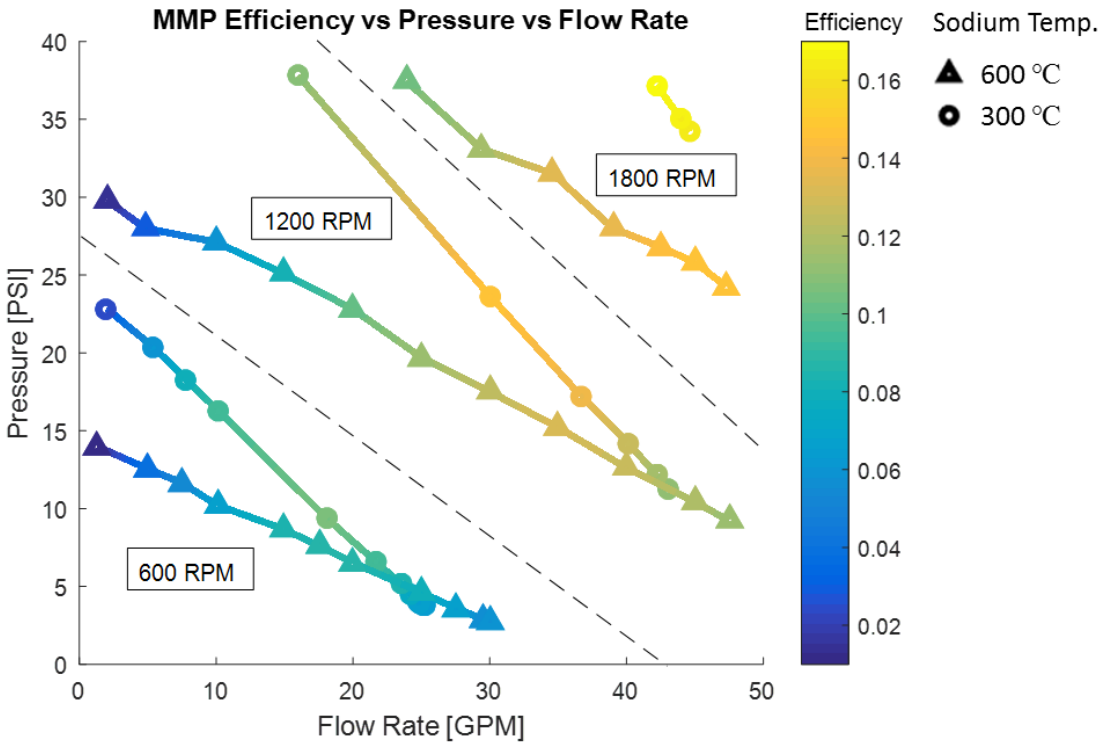

Figure 29: Moving magnet pump curves

Notice that two sodium temperatures were tested, 300C and 600 C, as labeled in Figure 29. Three different pump speeds were tested, 600 RPM, 1200 RPM and 1800 RPM. Efficiency was found using Eq. (6).

$$\eta = \frac{\dot{v}\Delta P}{P_{IN}} \tag{6}$$

Where η is the efficiency, $\dot{v}$ is the flow rate, ΔP is the pressure drop and P_{IN} is the power put into the pump. A maximum efficiency of 17% was found.

Magnet Temperature

An infrared camera was used to acquire temperature readings of the permanent magnets on the moving magnet pump during operation. The pump motor on the MMP was set to 300 RPM while the sodium temperature in the loop was set to 600C. The infrared camera was only able to acquire a photo of the circumferential temperature of the MMP magnets, yielding a temperature of 47C. This is well below the Curie temperature of 80C for neodymium and 350C for samarium cobalt magnets. This is the temperature at which the magnets begin to lose their power, thus efficiency of the MMP suffers.

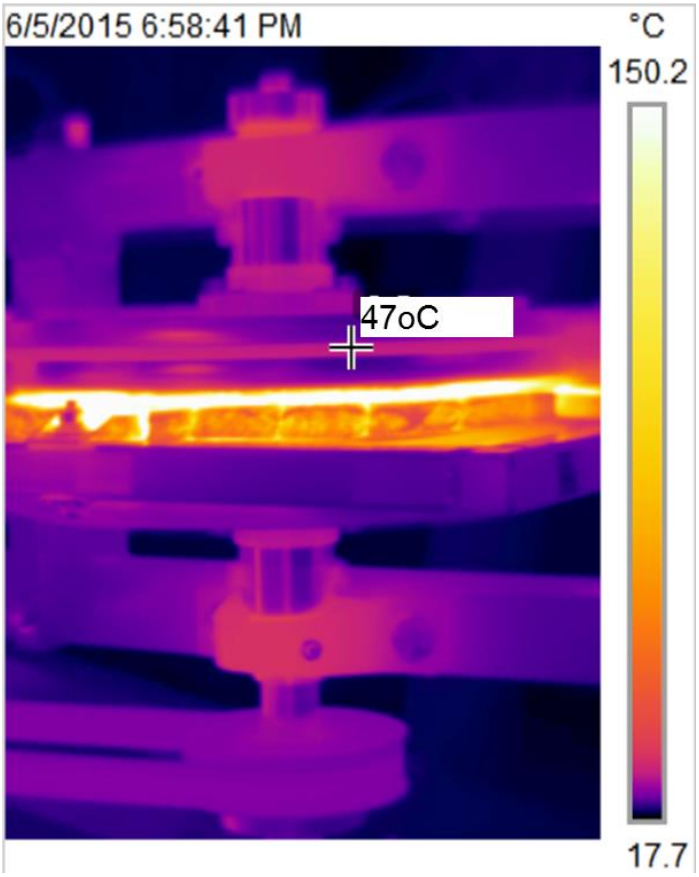

Figure 30: Moving magnet pump, permanent magnet temperature at circumference

LEVEL SENSOR DEVELOPMENT

A level sensor is an important component in a sodium loop. Without the ability to have port holes for level viewing and given the material compatibility issues of sodium, level sensing can prove to be a difficult task. Generally electrical point sensors are utilized in a sodium system. These sensors are used in the UW sodium loop, however in order to acquire continuous level sensing a resistance based continuous electric level sensor was developed.

Continuous Electric Level Sensor

A continuous resistive level sensor works as a potentiometer, with sodium providing a variable resistance dependent on level in a vessel. The level sensor built at UW was modeled after the "I-Tube" level sensor in the Sodium-NaK Engineering Handbook [8]. A simplified wiring diagram is included in Figure 31. The sensor works by submerging a hollow sheath into liquid sodium with 2 wires running the length of the sheath, Figure 32. The 2 wires are electrically isolated from the sheath except at the base where they are brought together at a junction. The entire assembly is sealed from sodium and electrically isolated from the vessel. A known current is sent through the input wire. The voltage across the sheath and reference wire is then measured. Since the current is known the resistance can then be calculated which correlates with the sodium height as a higher sodium level along the length of the probe will yield a lower resistance. It is important to take into account the vessel electrical resistivity under the sodium level, the resistance of the total sodium covering the probe as well as the resistance of the sheath.

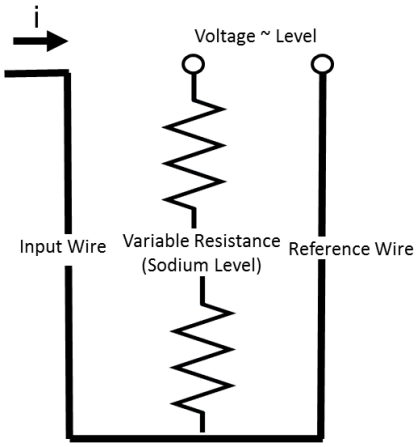

Figure 31: Continuous electric level meter wiring diagram

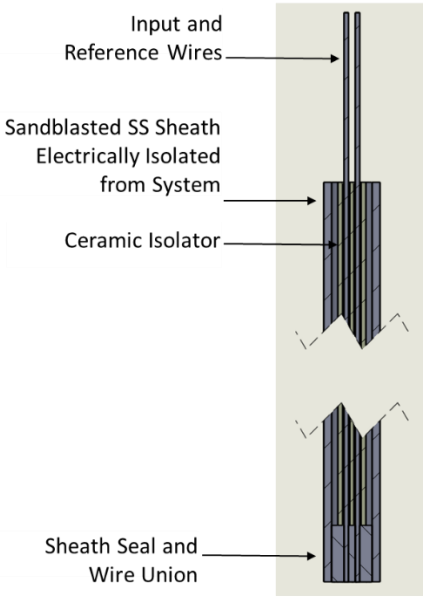

Figure 32: Schematic of continuous electric level meter

In the UW design, Figure 33, there are two 0.02” diameter 316 stainless steel wires running parallel down a 0.25” diameter (0.035” wall thickness) 316 stainless steel tube. The wires are electrically isolated from the outer sheath by a 0.125” outer diameter thermocouple insulator (Omega Model No. TRX-13218). A junction for the two wires was made from a cylindrical slug of length 0.25” with diameter on the order of 0.18” to provide an interference fit inside of the 0.25” level meter tube. Two 0.03” holes were drilled at the same spacing as the thermocouple insulator so that the wires could be pulled through the holes for welding. includes a picture of the e-level sensor components.

The level wires can be excited by AC or DC power supply. Note that DC excitation can cause errors via a thermoelectric EMF generated between the sheath and the sodium due to temperature gradients existing along the sheath and sodium. A DC power supply has been utilized

so far and it is assumed that the isothermal nature of the single heater zone expansion tank will reduce the contribution from this described effect.

Note that the "I-Tube" sensor included in the sodium handbook is mounted at the base of the vessel. This proves difficult to implement in the expansion tank geometry therefore the e-level probe was mounted from the top of the vessel. However, if the probe is not isolated from the loop when installed at the top of the vessel it can be shunted by the resistance of the vessel wall, causing the sensitivity of the probe to vary with level which makes the calibration curve of voltage versus sodium height non-linear.

To alleviate this issue the probe was mounted with a Teflon front ferrule to isolate the level sensor from the vessel. A simple fin heat transfer calculation was performed to ensure that the Teflon ferrule would not come close to its deterioration temperature of 260 oC when the sodium was at 600 oC. Note that an increased standoff can be used from the vessel to isolation ferrule increase the factor of safety in ferrule temperature.

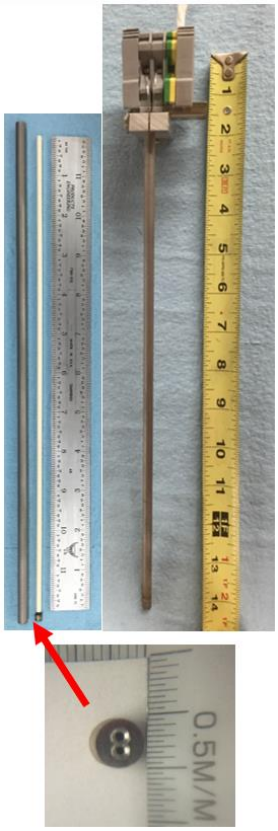

Figure 33: UW built continuous electric level sensor

In order to determine the functionality of the continuous electric level sensor, two resistive point sensors were manufactured and installed into the expansion reservoir on the sodium loop. The point sensors are electrically isolated from the system and complete an electric circuit when sodium shorts them to ground. A schematic showing the two point sensors and their orientation with respect to the continuous electric level sensor has been included in Figure 34. A photo of the two point level sensors can be found in Figure 35.

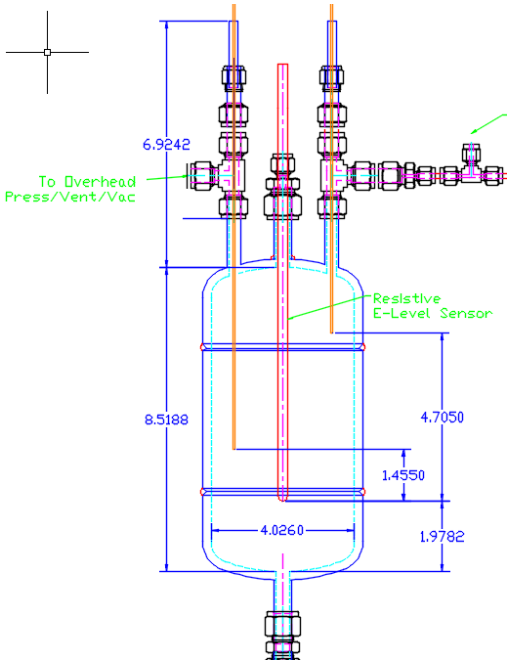

Figure 34: CAD drawing of continuous resistive electric level sensor and 2 point sensors

Figure 35: Photo of 2 electric point sensors

Sodium was slowly added to the overhead expansion reservoir until the continuous resistive level sensor was shorted to ground. This resistance reading gave a baseline measurement of resistance. The level of sodium was then slowly increased until the long point sensor signaled on. This process has been included in Figure 36, showing the point sensor voltage and continuous level sensor resistance as a function of time. The sodium was then raised further until the shorter point level sensor signaled on. The results of this analysis are included in Figure 37. A theoretical curve was created using the system and probe geometry along with the electrical resistivities of sodium and stainless steel at system temperature (300 C) in EES. The theoretical results were shifted to match the baseline resistance measurement when no sodium was around the sensor. Both the theoretical curve with and without this zeroing were included in Figure 37. This slight offset of ~0.002 ohms was due to the resistance of the electrical connections in the system and the measurement wire. The linear slope is the same for theoretical and actual data.

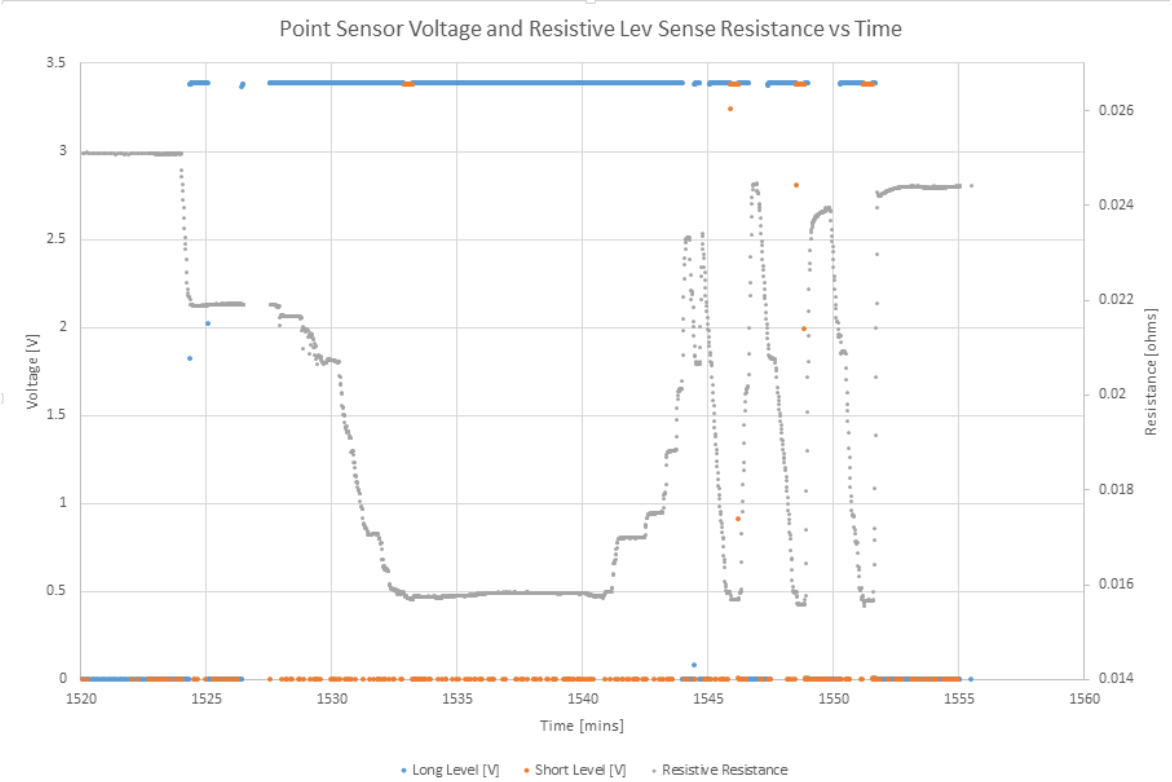

Figure 36: Voltage and resistance of level sensors vs time

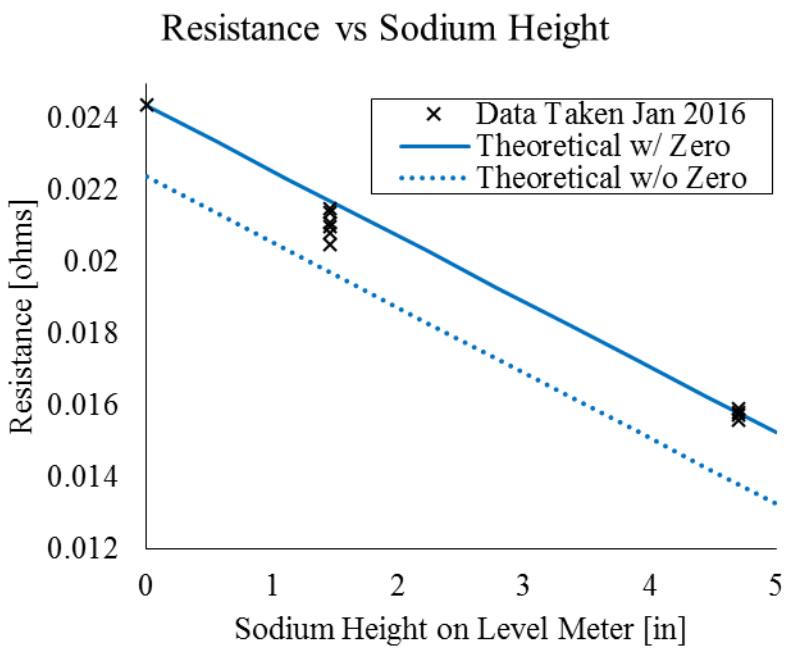

Figure 37: Resistance vs sodium height, data from sodium loop compared to theoretical fit

MATERIALS TESTING

Diffusion Bonded Samples

Diffusion bonded samples were tested in the sodium loop to determine how the properties of the bond would be effected. Two different types of sample were tested. The first consisted of Haynes 230 bonded to itself and the second was 316 stainless steel bonded to itself. Prior to testing, samples had to be cut to fit into the corrosion sample holders previously designed for the sodium loop. Wire EDM was used to cut slices to 0.070in, the sample faces were then polished to 0.0625in thickness with a surface finish from 1200 grit SiO sandpaper. A total of 4 slices were taken of each material to be tested.

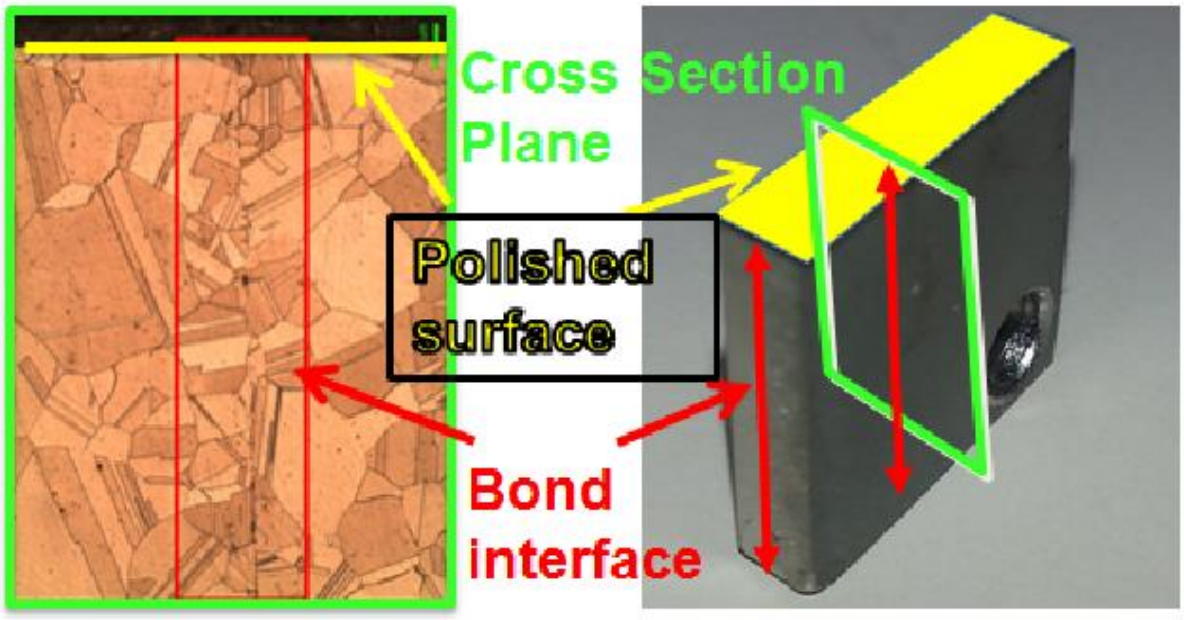

Figure 38: Diffusion bonded sample L - cross section view after slicing, R - Sample prior to slicing

After slicing and polishing, samples were sonicated in ethanol for 30 minutes to remove surface contaminants. Samples were weighed on a mitutoyo scale (Figure 39) with an accuracy of $2x10^{-6}$g. Samples were placed into the sample holder and prepared for insertion into the sodium loop.

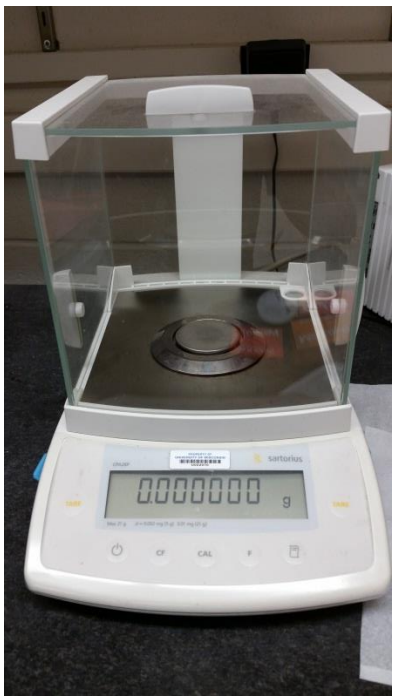

Figure 39: Mitutoyo scale used to weigh samples

Prior to testing, the cold trap in the loop was set at 5ppm overnight. Plugging meter measurements confirmed that the oxygen level was at 5ppm as expected. The samples were inserted into the loop through the sample insertion port in the upper reservoir. The samples were exposed for a total of 200 hours at 650C and 5ppm oxygen. After the allotted time had been reached, the sample holder was withdrawn through the sample insertion port and allowed to cool under argon atmosphere. The sample holder was rinsed in a series of ethanol and DI water baths to remove sodium that would hold the samples in place. When the samples could be removed, they were placed into an ethanol bath and sonicated for 30 minutes once again.

To compare the samples before and after exposure, weight change, optical microscopy, SEM, EDS, and microhardness testing were used to characterize the samples. Of special interest were results at the diffusion bonded interface compared to those of the bulk sample.

Both the 316 and 230 samples showed mass loss after exposure to sodium. The 230 samples appeared to be affected more by the sodium than the 316 samples. Previous corrosion testing showed similar results for the 316 samples, but there were no previous 230 samples to compare to. Because of this, it is believed that the diffusion bonding process does not significantly affect corrosion effects in the samples.

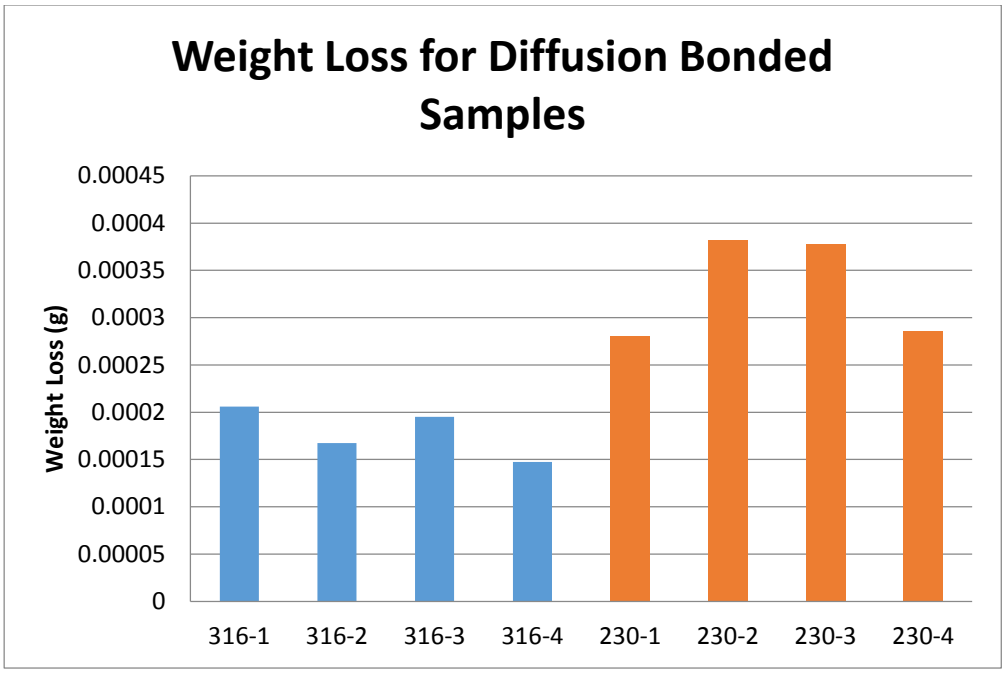

Microhardness testing was done on the first sample of each type. The samples were tested in a five by six array near the edge of the sample as seen in Figure 40: Microhardness testing pattern. The middle row was on the diffusion bonded interface. This allowed for identification of differences between the interface and the bulk material.

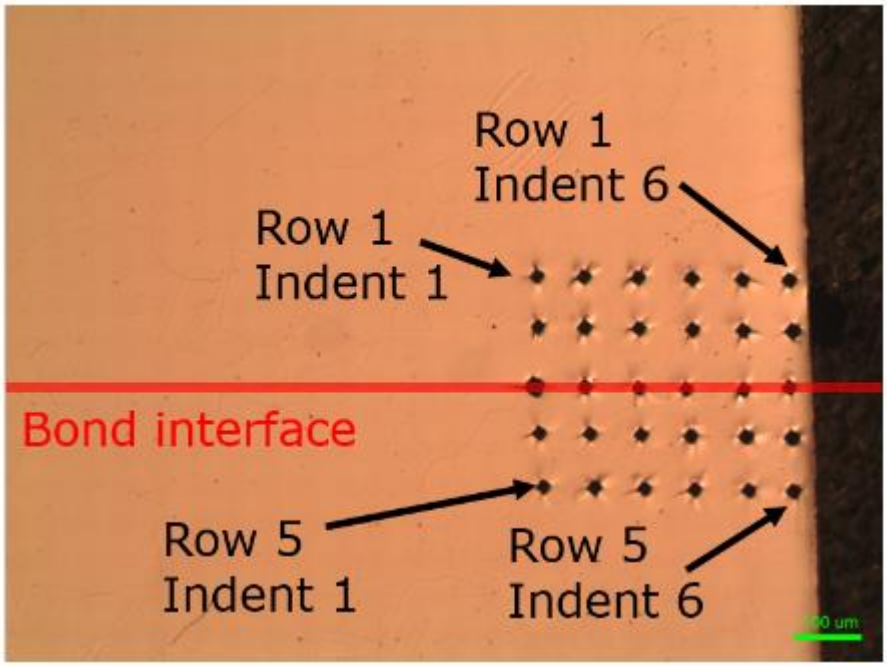

Figure 40: Microhardness testing pattern

In Figure 41: Comparison of microhardness before and after diffusion bonding process it can be seen that the microhardness of the 316 sample is significantly reduced by the diffusion bonding process, where the 230 sample is largely unchanged.

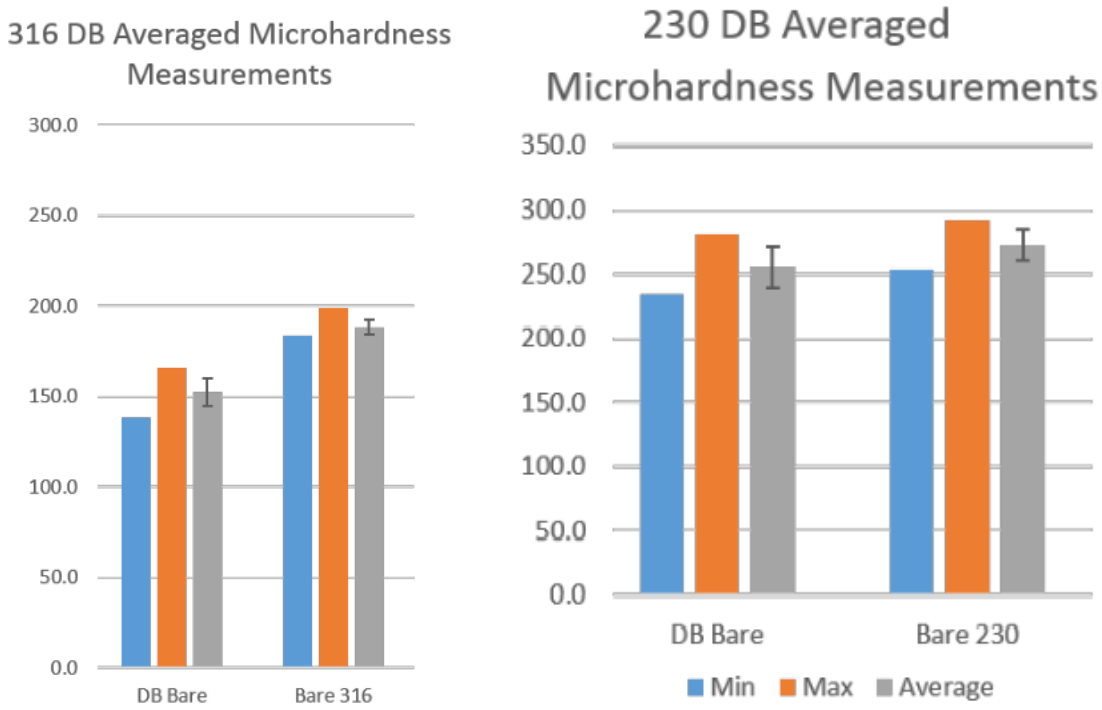

Figure 41: Comparison of microhardness before and after diffusion bonding process

Post testing results in Figure 42 indicate that both the 316 sample and the 230 sample increased in hardness from exposure to sodium. For the 316 sample, it should be noted that the maximum values occurred on the seam where the diffusion bonding took place and the minimum values occurred at the farthest locations. For the 230 sample, this trend was reversed.

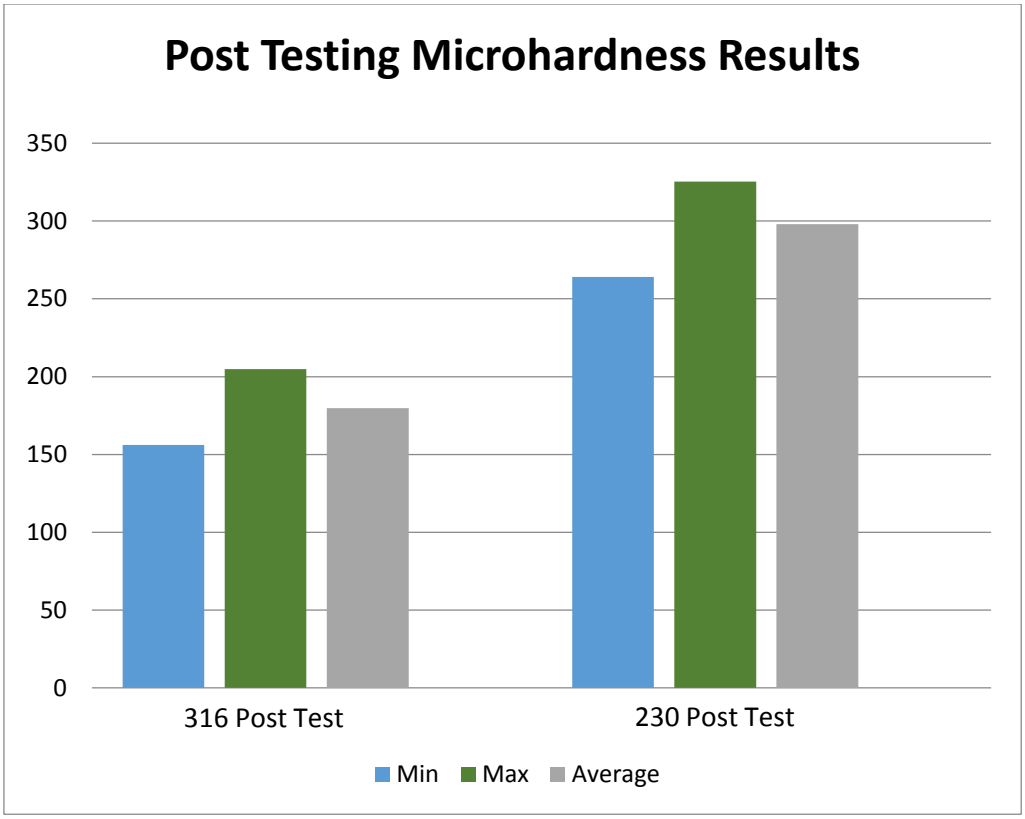

Figure 42: Post testing results

The optical microscopy, SEM, and EDS results all showed very little. In the optical and SEM images seen in Figure 43 and Figure 44, the bond became impossible to distinguish from the bulk of the sample when the edge was not visible

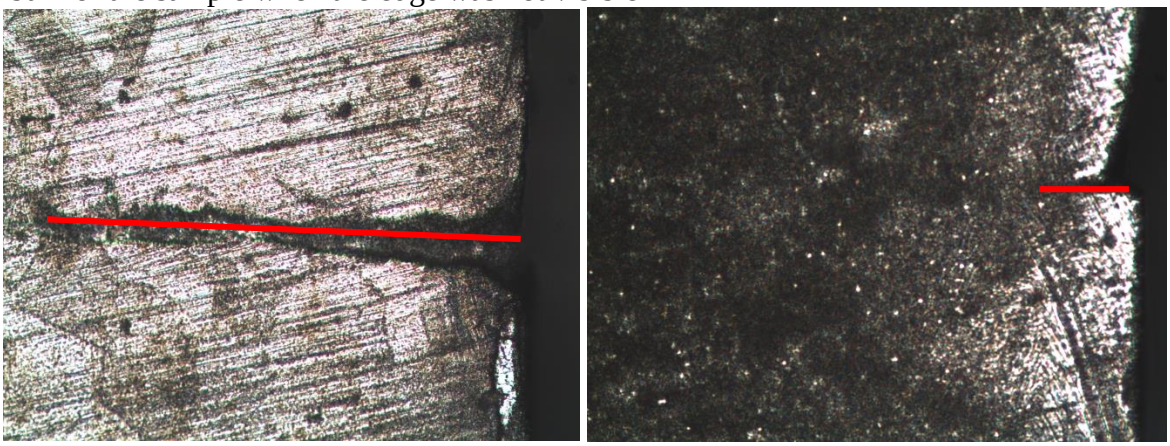

Figure 43: Optical images of diffusion bond at sample edge L – 316, R – 230

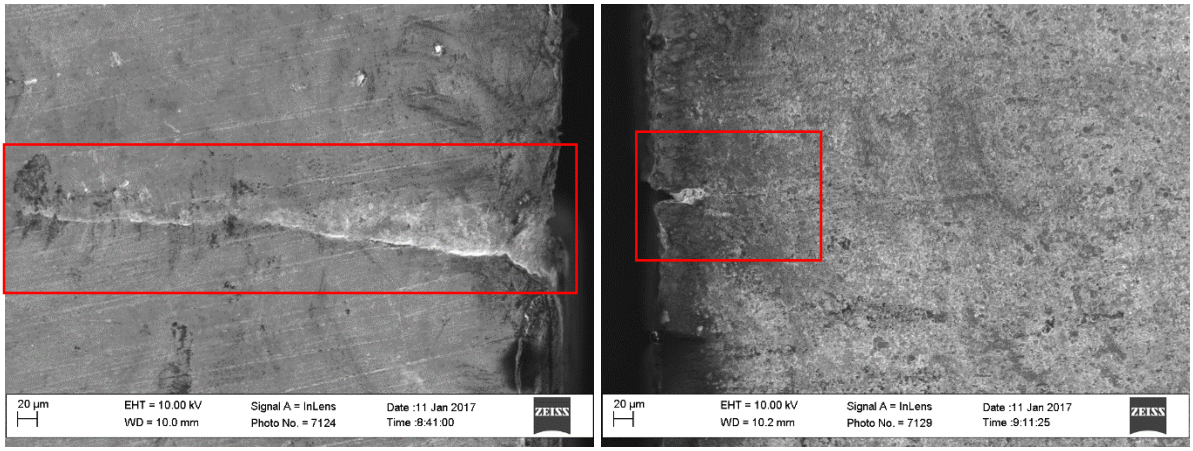

Figure 44: SEM images of diffusion bond on sample edge L - 316, R – 230

The EDS mapping of the 316 sample (Figure 45) showed that there was some carbon and chromium enrichment near the bond. It showed lower iron content in the same areas. Overall, this effect was difficult to distinguish, and does not signify significant compositional changes near the bond.

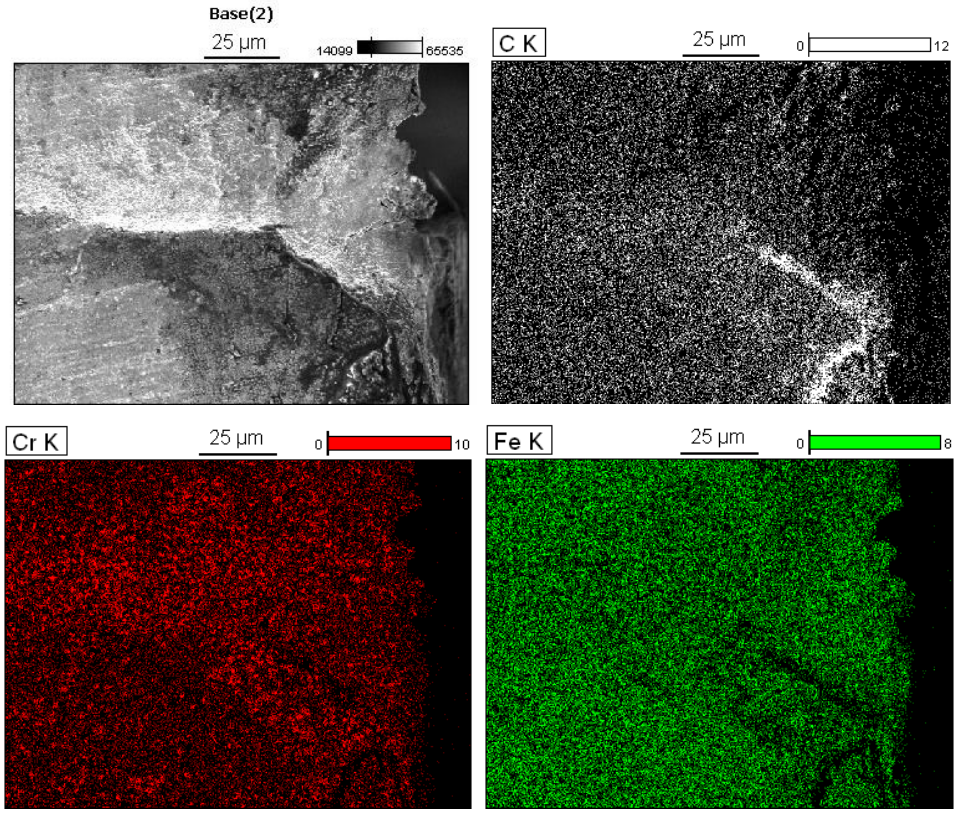

Figure 45: EDS mapping of 316 sample

The EDS mapping of the 230 sample (Figure 46) showed depletion of nickel and iron. The nickel depletion appeared to be spread across the sample surface irregularly. In these locations, oxygen was seen by the EDS scan indicating a nickel oxide buildup on the surface. This did not appear to be related to the diffusion bond. The chromium content appeared to be mostly

unchanged, with possibly a slight enrichment near the diffusion bond. The iron content is slightly depleted near the diffusion bond.

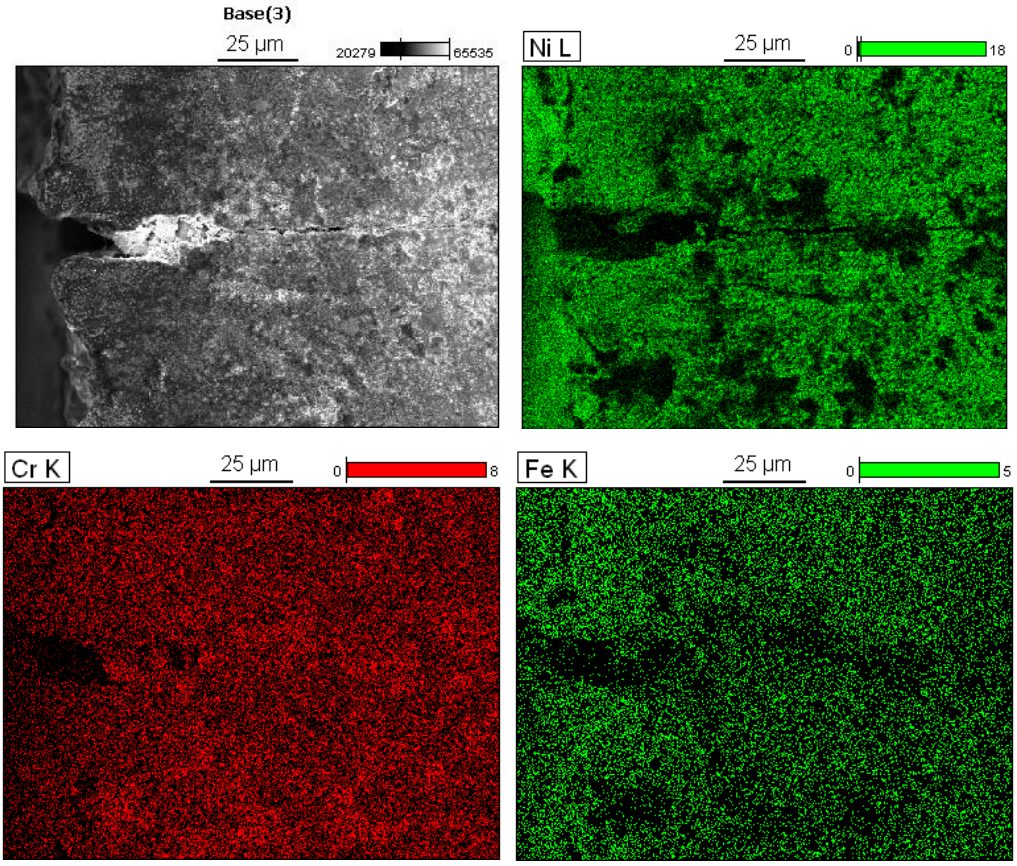

Figure 46: EDS mapping of 230 sample

OPTICAL FIBER DEVELOPMENT

Optical Fiber Temperature Sensor System Overview

The ODiSI-B system from Luna Innovations, pictured in Figure 47, was chosen as the optical fiber interrogator to perform distributed temperature measurements. This particular system analyzes Rayleigh backscatter of a near infrared laser beam to acquire temperature measurements. The ODiSI-B possesses a variety of sensing modes, included for reference in Table 8. These modes allow the user to strategically choose the spatial and temporal resolution as well as the maximum sensing length which is best suited for the particular application. The ODiSI-B allows the user to create optical fiber sensors in house. This reduces cost, reduces system down time when a fiber breaks and allows for the testing of experimental fiber sensors not available commercially.

Figure 47: Luna Innovations ODiSI-B optical fiber interrogator shown with standoff cable and control computer

Table 8: ODiSI-B Specifications

PARAMETER	SPECIFICATION				UNITS
Performance					
Standoff	50				meters
Wavelength Accuracy[1,2]	1.5				pm
Strain Range[3]	± 10,000				µStrain
Temperature Range[4,5]	-268 to 900				°C
Mode of Operation[6]	**Standard**	**High-Speed**	**High-Resolution**	**Extended Length**	
Maximum Sensing Length	10	2	10	20	meters
Acquisition Rate	100	250	23.8	50	Hz
Sensor Spacing	2.56	2.56	0.64	2.56	mm
Gage Length	5.12	5.12	1.28	5.12	mm
Strain Repeatability (Single-scan)	± 5	± 5	± 20	± 10	µStrain
Temperature Repeatability (Single-scan)	± 0.4	± 0.4	± 1.6	± 0.8	°C
Electrical Trigger					
Acquisition	TTL compatible				
Event	TTL compatible				
Physical					
Dimensions	14.42 x 13.60 x 6.55				in
Weight	17.1				lb
Power Consumption	50				W

1 Calibration is performed internally using a NIST-traceable HCN gas cell.

2 Temperature and strain accuracies from spectral shift of Rayleigh scatter are 0.15 °C and 1.25 µStrain, calculated using the default conversion coefficients 1 GHz = 0.8 °C = 6.58 µStrain [Othonos and K Kalli, Fiber Bragg Gratings (Artech House, Boston, 1999)].

3 Based on an effective spectral range of +/-12000 pm.

4 Based on realistic physical limitations of typical optical fiber as observed by Luna. Actual performance range will depend on sensor type, coating, and bonding adhesive used in application.

5 Luna's standard temperature sensors are polyimide coated, low bend loss fiber and operate in a temperature range of -50 to 200 °C. Please contact Luna for information regarding non-standard sensors.

6 Base configuration includes one mode of operation. Additional modes are upgrade options.

Optical Fiber Temperature Sensor Theory

Optical fibers are predominately used in the telecommunications industry to send a signal over long distances. Thus, minimizing signal attenuation has been the driving force in developing the optical fiber. Absorption, radiation and scattering losses all contribute to optical fiber attenuation.

Absorption of the light signal is mainly caused by photo-molecular interaction in the fiber, dissipating the light energy as heat. This absorption occurs in both the pure silica molecules which make up the optical fiber as well as impurities such as hydroxide ions (OH^-). These impurities

make their way into the fiber during fabrication and create particular absorption bands around 700 nm, 900 nm and 1400 nm light [9].

Scattering losses in fibers are due to microscopic inhomogeneities in the fiber core known as scatter sites. Given the high manufacturing quality of modern optical fibers these scattering sites are generally much smaller than the incident light. Thus the dominant loss mechanism of light propagating along a single mode optical fiber is Rayleigh scattering. Rayleigh scattering is an elastic interaction and the scattering intensity is proportional to the inverse of the wavelength to the fourth power. Thus shorter wavelengths are scattered more strongly.

These absorption and scattering losses dictate locations where low loss occurs, show in Figure 48 [9]. Notice the lowest loss window occurs at 1550 nm. This is the reason the ODiSI-B possesses a laser with a center wavelength of 1550 nm.

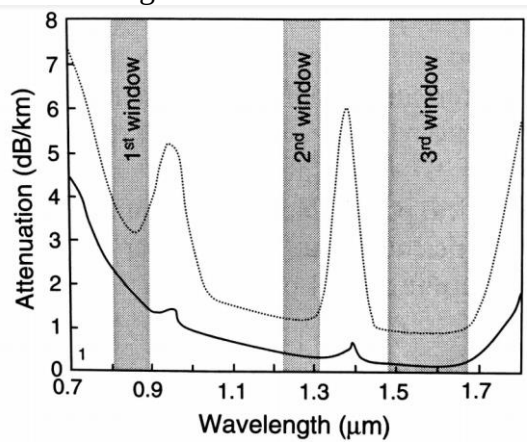

Figure 48: Wavelength dependence of light attenuation in a silica fiber. Dotted: Old silica fibers, Solid: modern silica fibers [9]

Radiation losses result mostly from mechanical irregularities in the fiber introduced during the fiber drawing process. Larger mechanical irregularities introduced via bending occur when deploying a fiber in a non-linear shape.

Backscattered light from Rayleigh scattering is utilized by the optical fiber sensors used throughout this work. Optical Frequency Domain Reflectometry (OFDR) is the technique utilized to acquire the Rayleigh backscatter and prepare it for analysis to produce continuous temperature measurements.

OFDR uses a near infrared laser coupled into a fiber optic Mach-Zehnder interferometer. This interferometer consists of a reference fiber, a fiber under test (FUT) and an optical coupler. Light from the laser is split into the reference and FUT by the coupler. Light then Rayleigh backscatters along both fibers. The backscattered light from the reference fiber and FUT are recoupled, allowing the signals to form an interference pattern. The laser light wavelength is continually swept over a particular range to produce a periodic backscatter signal. The frequency of this signal depends on the location of the scatter site. A location further away from the detector results in a higher interference frequency. The interference signal is sent to the computer via a photodiode to perform a Fast Fourier Transform (FFT). An illustration of this technique can be seen in Figure 49.

After the FFT we are left with signal amplitude as a function of frequency (distance along fiber). A so-called “key” or reference scan can then be taken at a stable condition (room temperature). At increased temperatures the local variations in the index of refraction in the optical fiber core begin to migrate apart from one another. This is due to thermal expansion of the fiber.

The OFDR scans reveal a "stretched" amplitude vs frequency plot at locations at elevated temperature, having the same general shape but with amplitude spikes at slightly different frequencies due to the migration of scatter sites. This at-temperature scan can then be cross correlated with the key to reveal the amount of scatter site movement, thus local temperature can be calculated. As Rayleigh scattering is a completely elastic process, the backscattering encountered in a particular fiber at a specific temperature will always be identical given the mechanical integrity of the silica fiber core has not been compromised. A figure depicting the FFT signal can be found in Figure 50 [10].

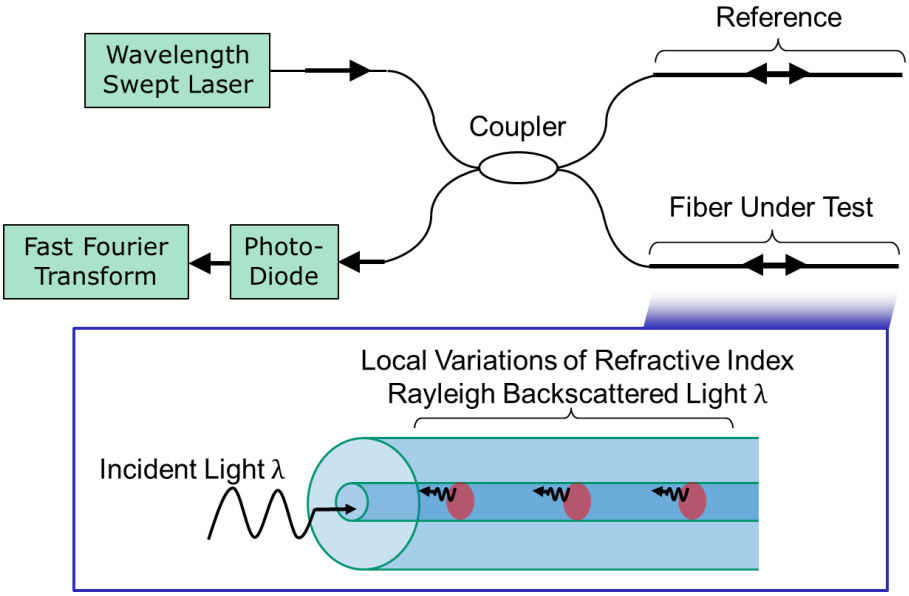

Figure 49: Illustration depicting OFDR and Rayleigh Backscatter

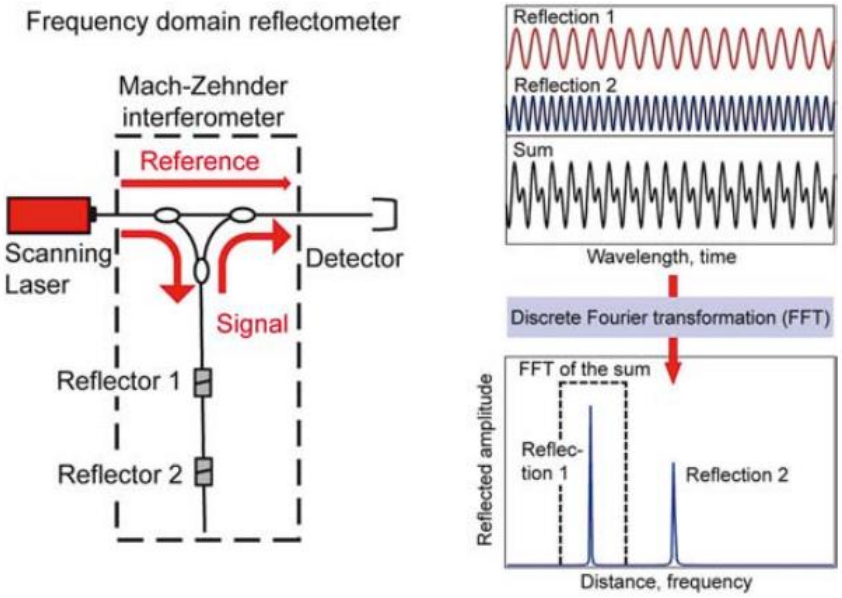

Figure 50: Illustration of interferometer and FFT signal [10]

Optical Fiber Temperature Sensor Manufacture and Deployment

In order to manufacture optical fiber temperature sensors in-house, a Fujikura 70s fusion splicer was purchased, as pictured in Figure 51. The fusion splicer allows for fiber-to-fiber and fiber-to-connector splicing. Connectors used throughout this work were AFL's LC/APC FUSEconnects (item# FUSELC2SMA60). This connector type was dictated by the female LC/APC connection at the input of the ODiSI-B. The fibers used throughout this work are detailed in Table 9. LC is a nominal connector type while APC stands for angled polished connector. The silica is polished and angled at the mating face so that reflected light is directed out of the waveguide, thus reducing noise in the signal.

Notice that acrylate, polyimide and carbon/polyimide coatings were used. The acrylate coating possess a manufacturer specified maximum temperature of 85C while the polyimide and carbon/polyimide possess a maximum temperature of 300C. Above this temperature the integrity of the optical fiber coating is compromised, exposing the cladding and core to the environment.

In order to splice an optical fiber to another fiber or to a connector the end must be prepared. This is done by first removing approximately 50 mm of coating. To remove acrylate from a fiber a pair of single mode fiber coating strippers will suffice. Any acrylate residue may then be wiped away with an alcohol coated lint free wipe. The strippers will not remove polyimide coating as the polyimide to too hard. Passing the end of a polyimide coated fiber over a small flame, such as from a Bic lighter or candle, will carburize the coating enough to allow for the removal with acetone and a lint free wipe. This same procedure can be used with the carbon/polyimide coated fiber. Care must be taken so as not to damage the fragile silica fiber with the flame. It will become obvious if the fiber has been damage as it will break upon subsequent handling or the fusion splicer will read a poor splice.

Once the coating has been removed the AFL CT-30 precision fiber optic cleaver may be used to create a clean, 90 degree cut in the fiber end at approximately 10 mm away from the start of the fiber coating. This precision cleave is essential for a good splice with minimal reflection and/or absorption of the propagating light. A fiber can then be installed on one side of the fusion splicer, along with another fiber or connector. The process of splicing with the Fujikura is automated, and assuming the cleaves are of high quality and there is no debris on the fiber ends should not be difficult, see splicer manual for further instructions. Images of the fiber before and after splicing on the splicer display show a precision splice with low losses estimated, Figure 52.

Figure 51: Fujikura 70s Fusion Splicer with AFL CT-30 Precision Fiber Optic Cleaver

Table 9: Optical fibers used throughout this work

Fiber Coating	Brand	Item #	Coating OD [µm]	Clad OD [µm]	Core OD [µm]	NA [-]
Acrylate	Corning	SMF-28e+	245	125	8.2	0.14
Polyimide	OFS	BF06160-02	155	125	4.6	0.21
Carbon/ Polyimide	OFS	F21972	155	125	4.6	0.17
Acrylate	OFS	552HP WR040	250	125	0 (coreless)	core-less

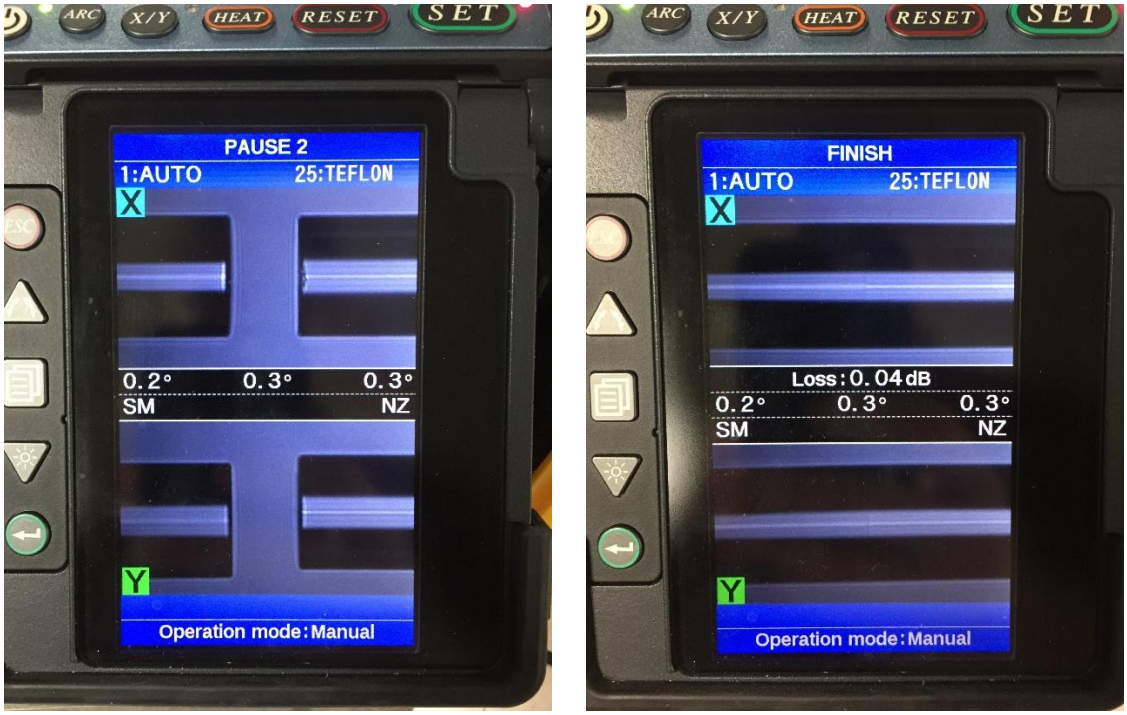

Figure 52: Single mode to single mode optical fiber splicing. Left: un-spliced, right: spliced.

The ODiSI-B requires 30 cm of unstrained/room temperature optical fiber in order for the cross correlation function of FFT to have a reference for orienting itself. This fiber may be installed in a Kevlar reinforced bifurcation tubing to provide support and protect it from breaking. It also reduces noise in measurements as any disturbance in air in the laboratory blows a bare fiber around. A picture showing a fiber installed in yellow Kevlar reinforced bifurcation tubing and green strain reducing boots can be found in Figure 53. Notice the LC/APC connector on one side of the yellow tubing. The other end of the fiber is epoxied onto a 1/8" OD, 0.040" ID stainless steel tube. The epoxy used is a vacuum grade high temperature 2 part epoxy, Hysol 1C.

Figure 54 gives a schematic of a method for installing an optical fiber into a high temperature system which requires a capillary tube to protect the fiber. The previously described epoxied fiber to stainless steel tube interface is swaged onto a Swagelok union-tee. The other end of the tee has a 1/8" OD, 0.040" ID 316SS tube swaged onto it as well. This tube has a 1/32" 316SS capillary tube silver soldered onto the top of the 1/8" tube, as seen in Figure 54 and Figure 55. The other end of this tube can then be installed in the system via a Swagelok union. The perpendicular port in the union tee can then be used to pull a vacuum and flush with inert cover gas.

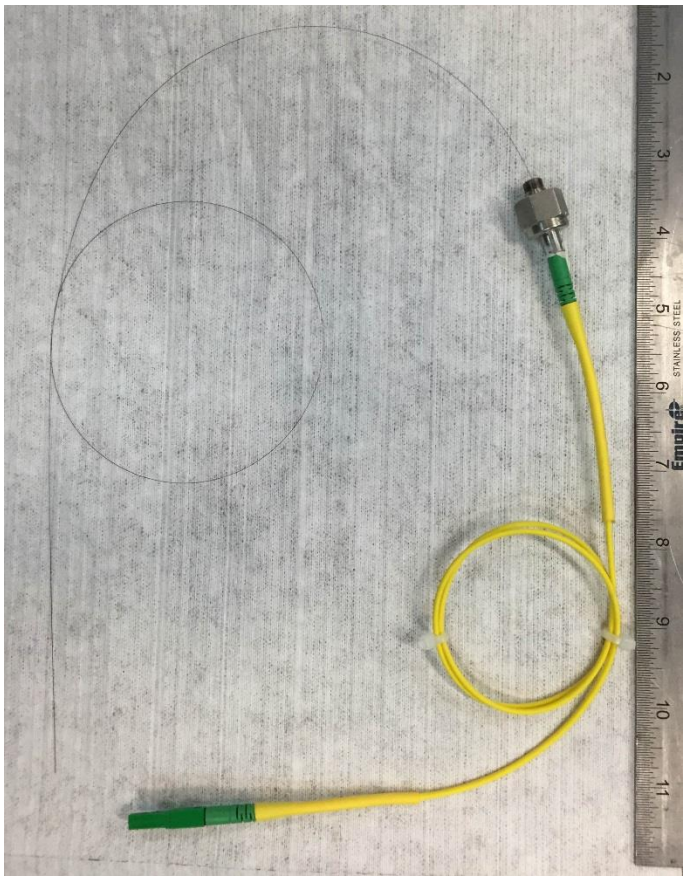

Figure 53: Optical fiber with strain reducing boots and bifurcation tubing

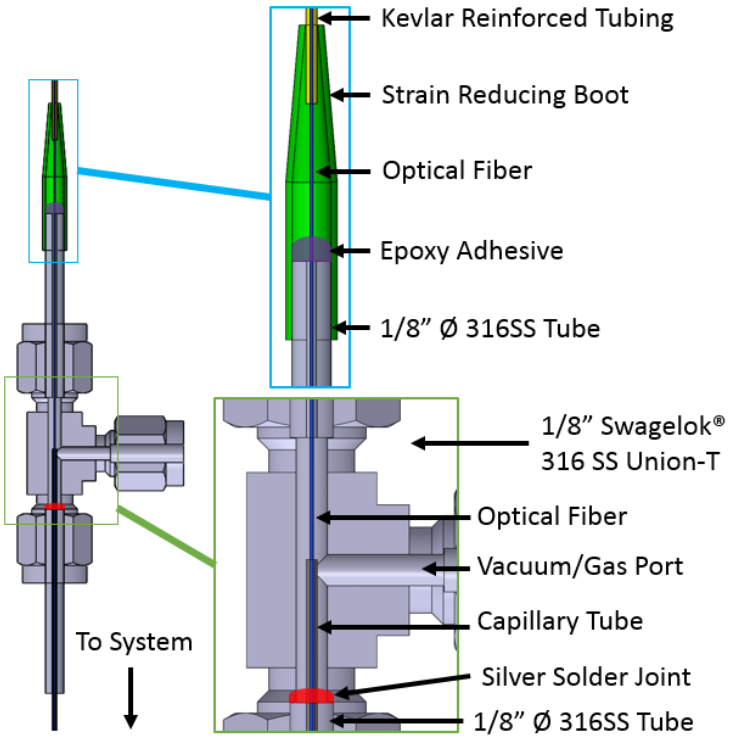

Figure 54: Optical fiber installed in system

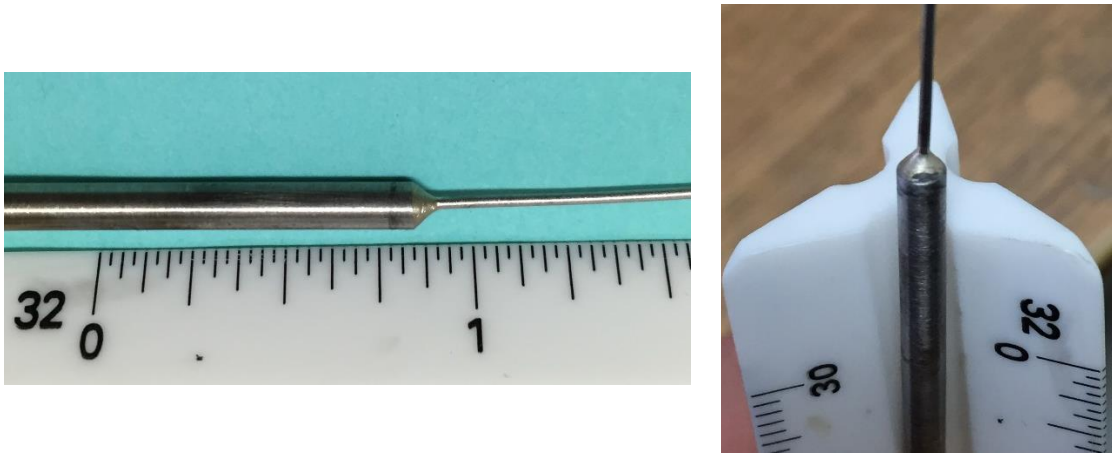

Figure 55: Silver solder joint, 1/8" tube to 1/32" capillary

The 1/8” stainless steel tube which attaches the fiber capillary to the system can be used to position the fiber in geometry that is difficult to install capillaries. Figure 56 shows a CAD drawing and photo of a fiber which was installed along the length of a cartridge heater in the sodium loop. The fiber had to be installed at an angle as the cartridge heater was positioned concentrically down the length of the loop tube. This setup limits any sharp bends in the fiber and insures there is minimal vibration caused by high flow rates. Figure 57 shows a view of the fiber in capillary with 1/8” tube positioning the capillary close to capillary.

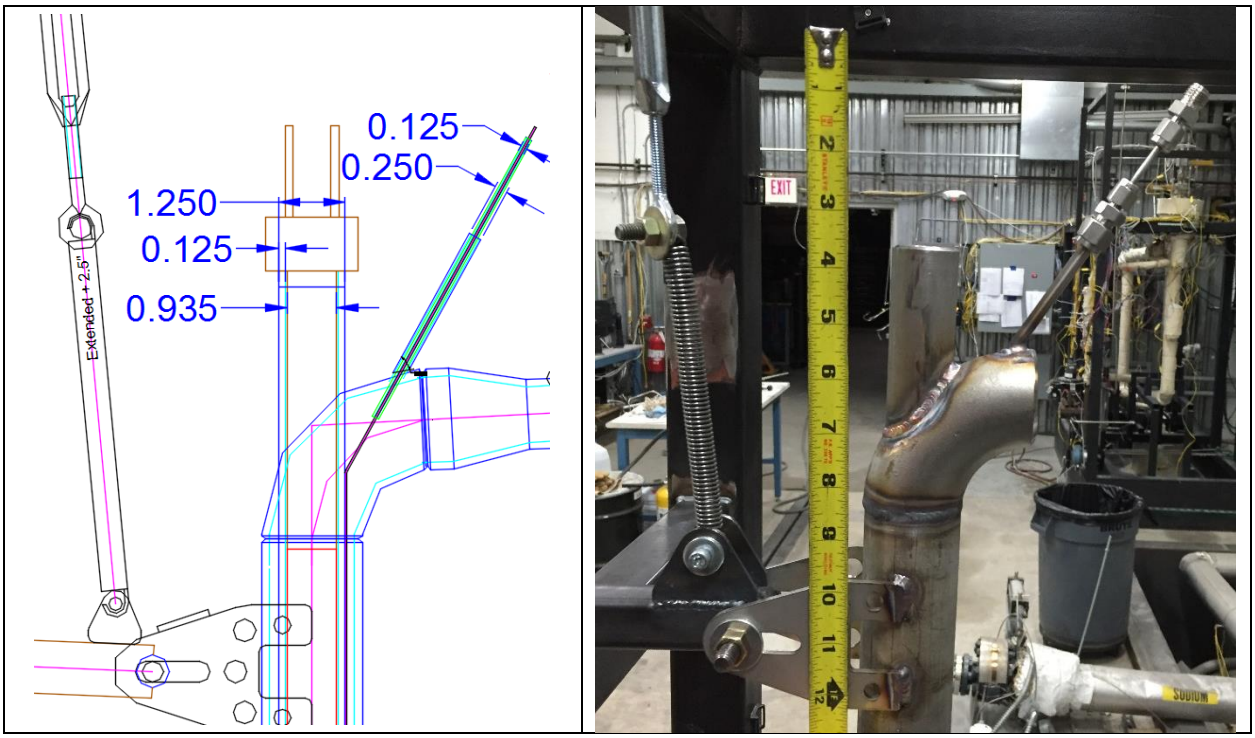

Figure 56: Optical fiber in capillary installed, 1/8" tube providing support for capillary

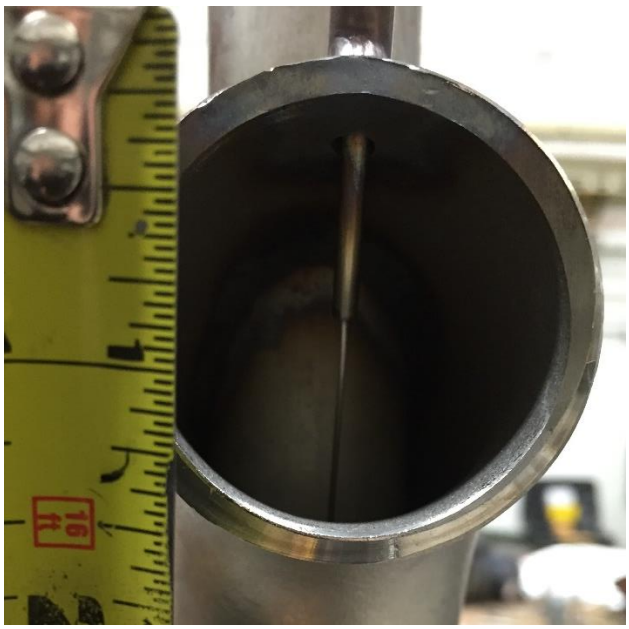

Figure 57: View of 1/8" support for capillary

An optical fiber must be terminated to properly diffuse the unscattered laser beam out of the optical fiber at the fiber end. Failure to terminate the fiber leaves a reflective surface at the end of the fiber which can affect the signal to noise ratio of the Rayleigh backscatter signal. Two options for termination include splicing on ~8+ cm of coreless optical fiber to the end or simply making a tight curl at the end of a fiber under test. Figure 58 presents these two termination methods. Splicing on a coreless termination fiber puts a large source of reflection at the splice and

at the end of the termination fiber. This can increase the signal to noise ratio of the temperature reading. A curled termination does not induce as much reflection at the fiber end. Typically 2 loops of ~5mm diameter sufficiently terminates the fiber. Note the loops should be on top of each other not one after the other to completely diffuse the light from the fiber core.

A CAD drawing of a curled termination in a protective housing can be found in Figure 59. The fiber capillary is silver soldered to a 1/8" tube which is swaged in place. A 3/8" to 1/8" reducing union can then be used to swage an approximately 3" long 3/8" tube which houses the curled termination. During fiber installation the fiber is pushed through the capillary leaving approximately 15 cm of fiber after the 3/8" to 1/8" reducer. With the protection housing tube removed the fiber can be curled twice at 5mm. Note that the curl should allow for adequate system thermal expansion above it so that the fiber is not locked between the epoxy at the inlet and the curl being pulled by the capillary. The termination curl can then be secured by applying an adhesive to the fiber so that it does not come undone. The end of the fiber after the termination curl can then be trimmed with side cutters.

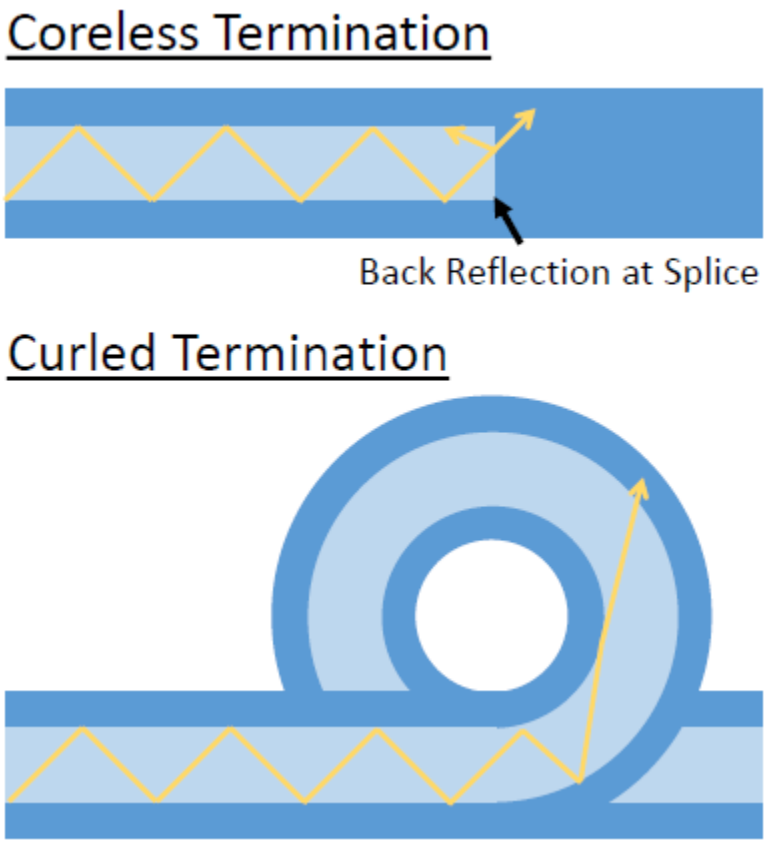

Figure 58: Coreless vs curled termination

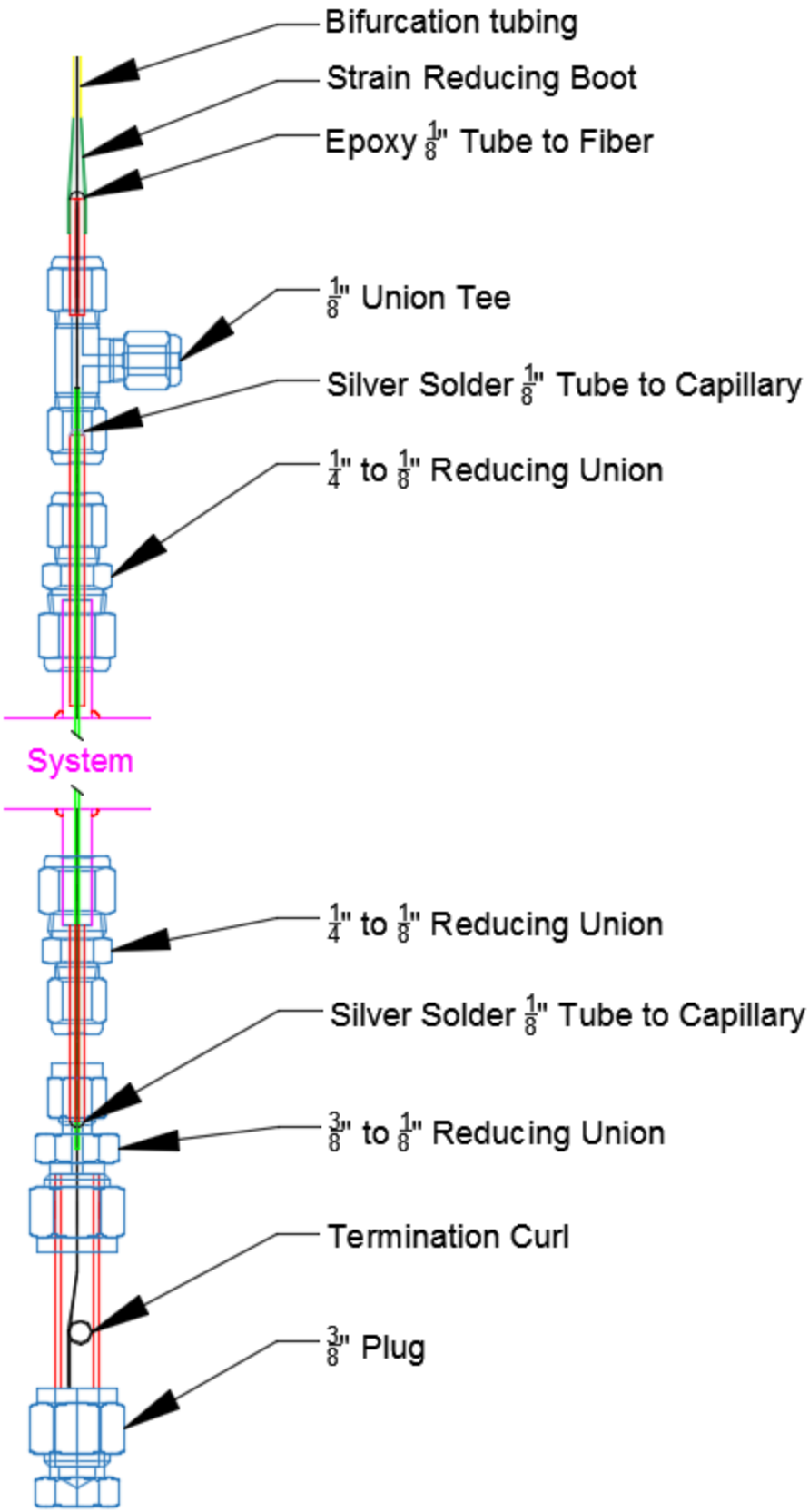

Figure 59: Setup for housing optical fiber termination curl

Following fiber termination the fiber can then be keyed using the ODiSI-B Sensor Configuration program. A screenshot of a fiber being keyed can be found in Figure 60. Notice the fiber under test is located between the yellow and red vertical lines (between 0.23 to 1.08 meters).

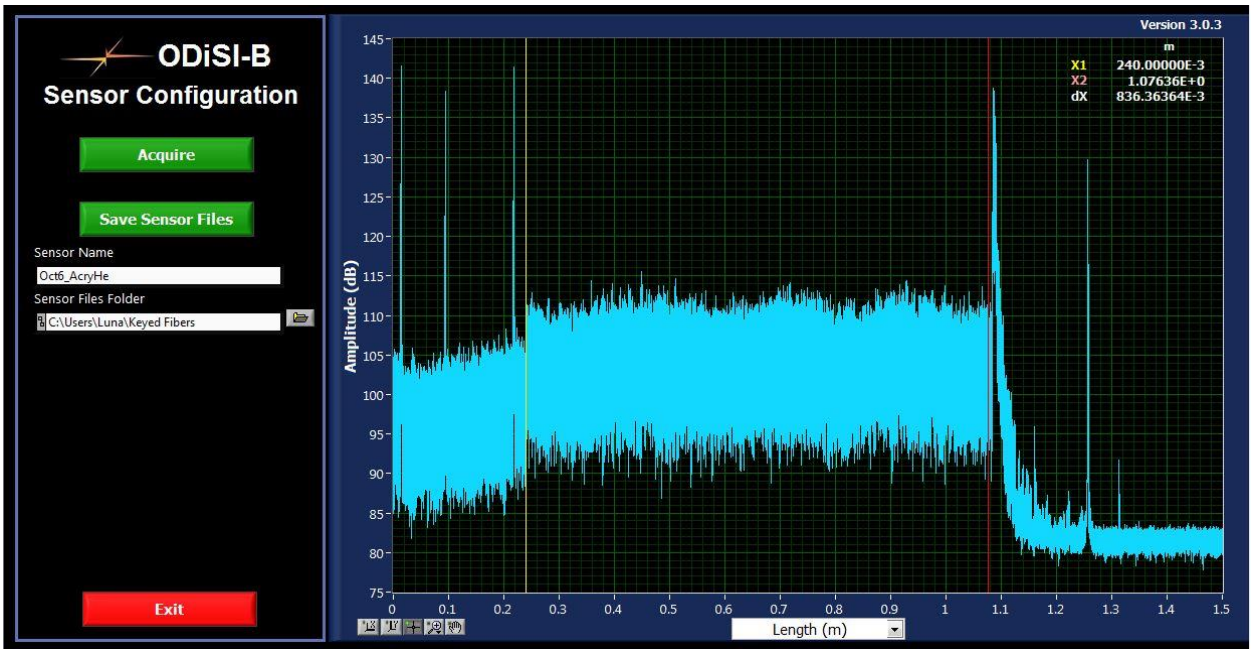

Figure 60: Keying a fiber with ODiSI-B

Optical Fiber Noise

Noise in each mode of the ODiSI-B was characterized by using a 1 meter length of acrylate coated fiber with curled termination end. The final 30 cm of the fiber was sealed in a ¼" stainless steel tube. The tube was covered with a layer of 2 cm thick kaowool insulation to reduce convective heat transfer and thus prevent temperature variation due to the environment. Histograms were made of the variation of temperature from mean over a 10 second acquisition period of the final 15 cm of the fiber, the results for each mode are given in Figure 61. The standard deviation of each fiber modes is given in Table 10.

In order to determine the difference in noise between coreless and curled termination end, 1 meter long temperature sensors were made with acrylate coated fiber using each termination technique. The fibers were again installed with the final 30 cm sealed in a 1/4" stainless steel tube with 2 cm thick kaowool insulation to reduce convection. 15 cm of coreless termination was used and 2x 5mm diameter curls were used for each respective technique. The Rayleigh backscatter profile from keying the fiber ends can be found in Figure 62. One can notice a distinct peak at 1.15 m where the coreless fiber ends. This large peak is not seen with the curled termination as there is no light left in the fiber at the fiber end after being diffused out of the fiber in the curl. To show the difference in termination induced noise a gauge at similar locations inside of the insulated area for each fiber temperature was used to take temperature data over a 10 second period using the standard 100 Hz scan mode. A histogram showing temperature variation from mean for each fiber can be found in Figure 63.

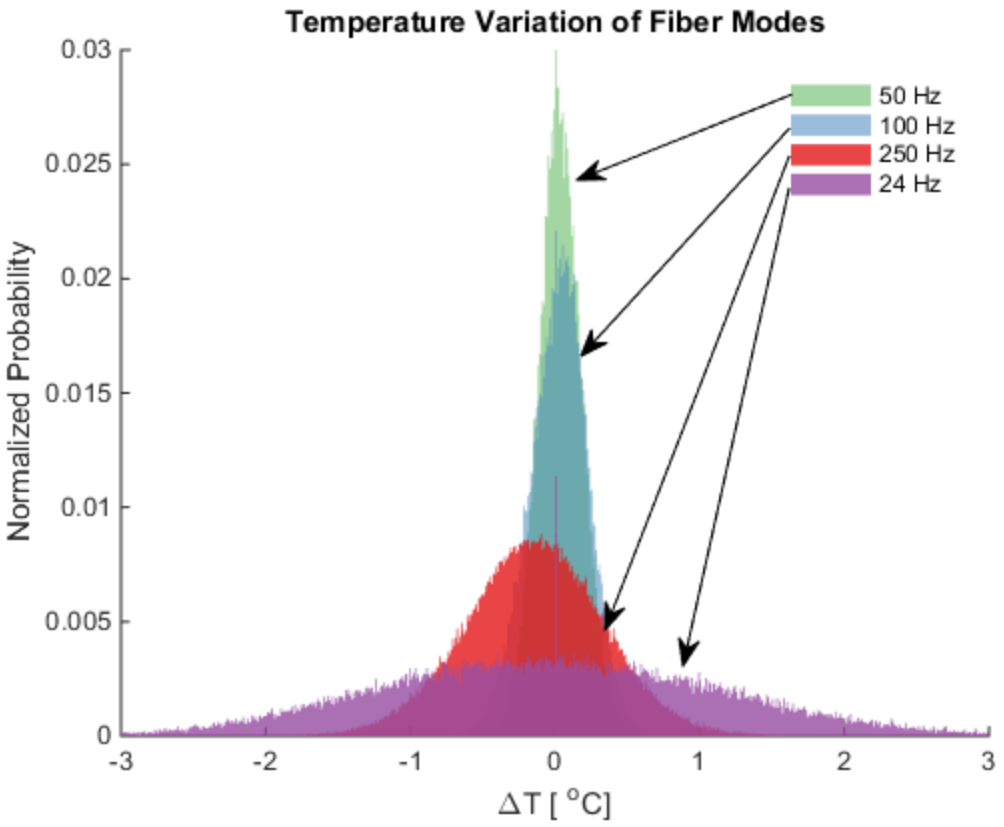

Figure 61: Histogram of temperature variation from mean over 10 second period

Table 10: Standard deviation of 10 second period of 15cm fiber at room temperature

ODiSI-B Mode	**Spatial Resolution [mm]**	**Acquisition Rate [Hz]**	**Standard Deviation [C]**
Extended Length	2.56	50	0.147
Standard	2.56	100	0.198
High Speed	2.56	250	0.480
High Resolution	0.64	24	1.187

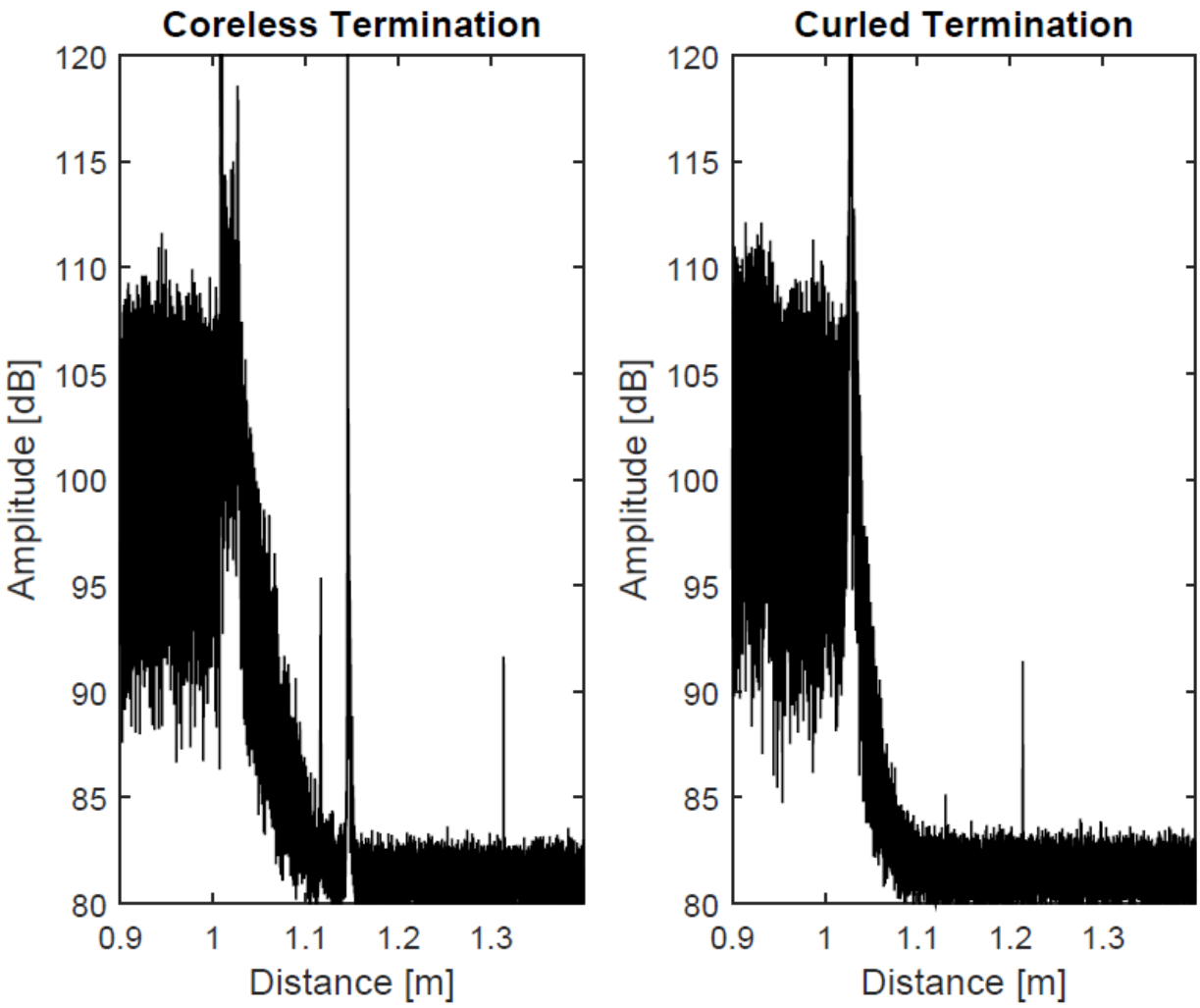

Figure 62: Coreless vs curled termination, 1 meter acrylate coated optical fiber

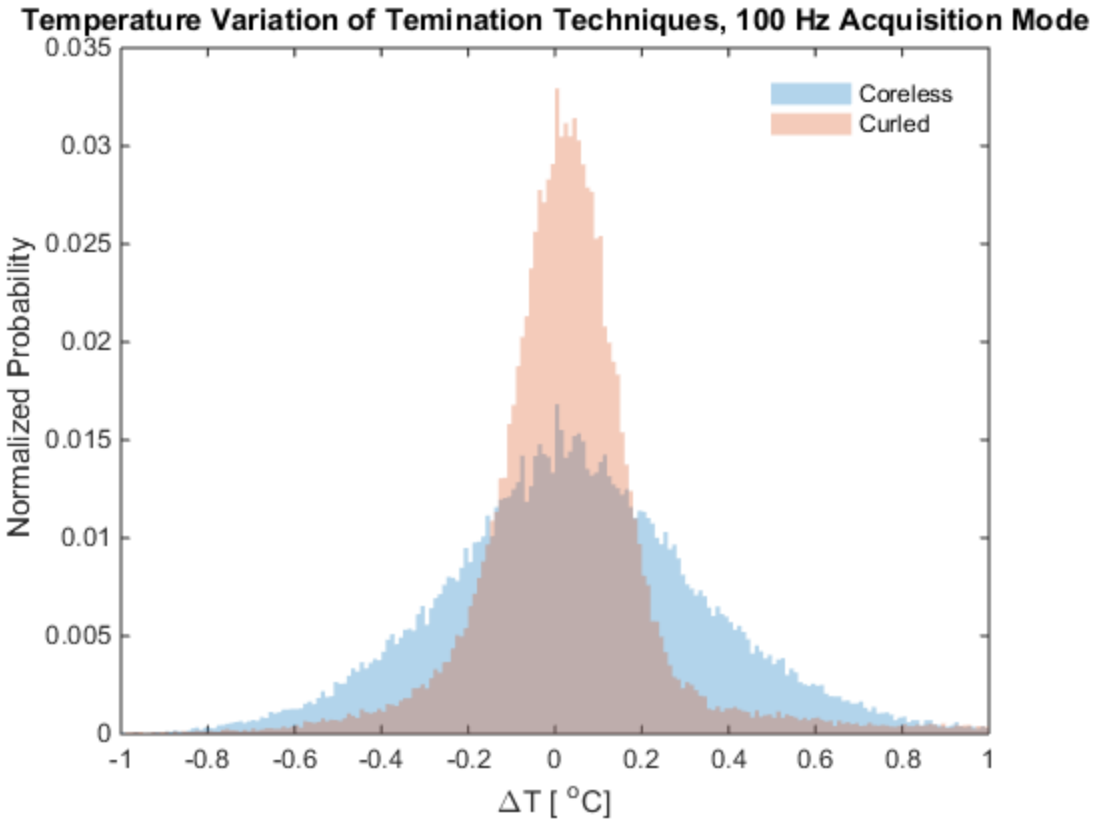

Figure 63: Temperature variation histogram of termination techniques

Optical Fiber Furnace

A Lindberg Model 55773 tube furnace with 1200 oC maximum temperature was used for high temperature optical fiber testing. An overall picture and schematic of the furnace can be found in Figure 64. The tube furnace has a length of 130 cm and a diameter of 18 cm. It accommodates up to 4 fibers at a time. In the furnace the fibers are supported with ¼" 316 stainless steel tubes. The tubes are supported on either end of the furnace with a mounting structure. 3 K type thermocouples were spot welded to a fifth tube positioned parallel and equidistant to the 4 fiber mounting tubes for furnace temperature acquisition.

The leftmost mounting structure can be seen in Figure 64 and Figure 65 and functions as the fiber inlet. The fibers are installed in the same manner shown in Figure 54 and Figure 59. As can be seen in Figure 65 a valve manifold allows for the independent control of the cover gas of each fiber tube. Thermal expansion coils allow the fiber to be fixed on either end of the furnace. When installing a fiber extra slack is pushed into the system, enough to account for the thermal expansion of the fiber tubes. The extra fiber sits on the circumference outer of the thermal expansion coils as shown in Figure 66. When the fiber tubes extend and pull the fixed fiber the fiber slack in the coils travels to the inner circumference, without breaking, as shown in Figure 66. Note that usually the termination side of the fiber is not rigidly fixed but designing for fixed fiber on either end of the furnace allows for experiments that measure optical properties on the other end of the furnace, not just backscatter.

To keep slack out of the 4 tubes in the furnace which house the fibers during thermal expansion a system shown on the right side of Figure 64 was designed. As seen in Figure 67 and

Figure 68 a rigidly mounted plate and clamping collars compress springs on each fiber tube. The spring compression force at maximum extension (1200 C) was chosen to keep the fiber tubes taught, even with the thermal expansion of 316SS at these high temperatures. Figure 69 gives the location of the thermocouple tube and 4 fiber tubes with a dimensioned drawing of the thermal expansion plate.

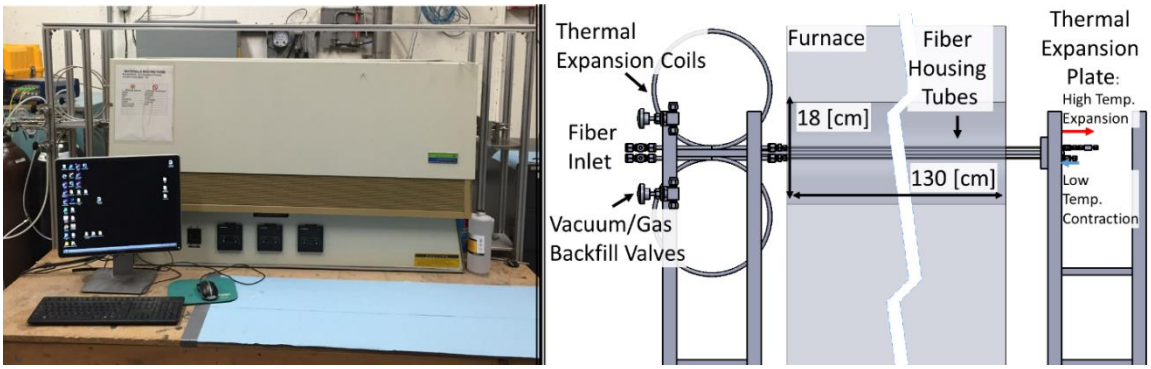

Figure 64: High temperature furnace testing of optical fibers, overall photo and schematic

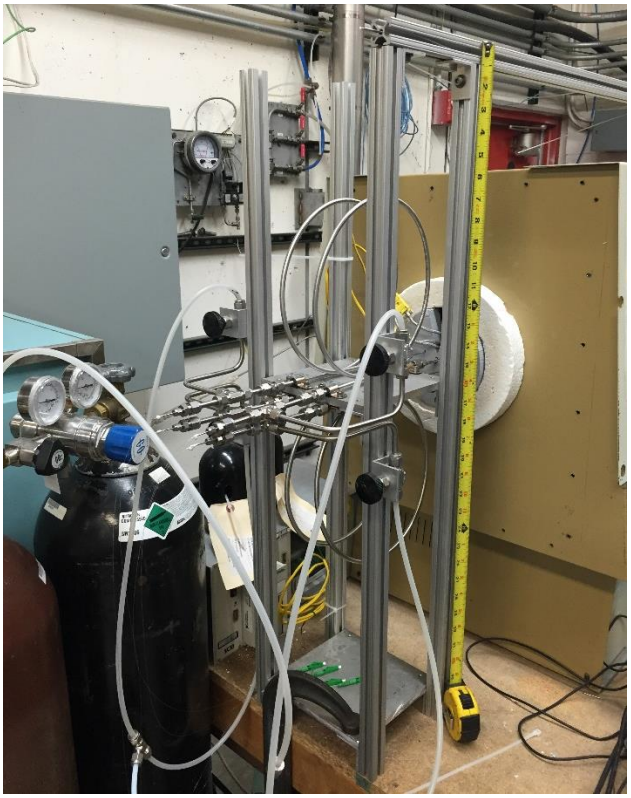

Figure 65: Optical fiber furnace inlet

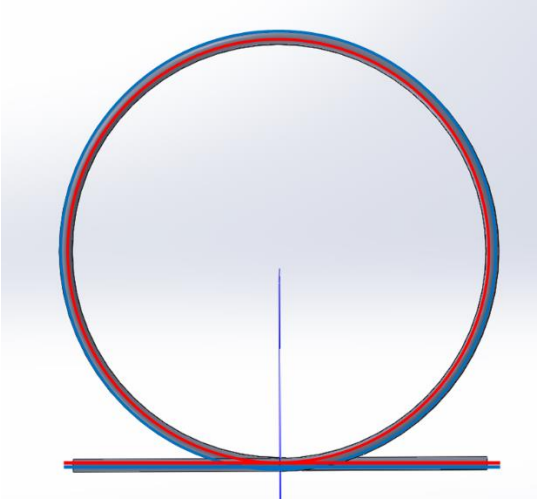

Figure 66: Fiber expansion loop. Blue: Initial fiber position, red: fiber with furnace at temperature

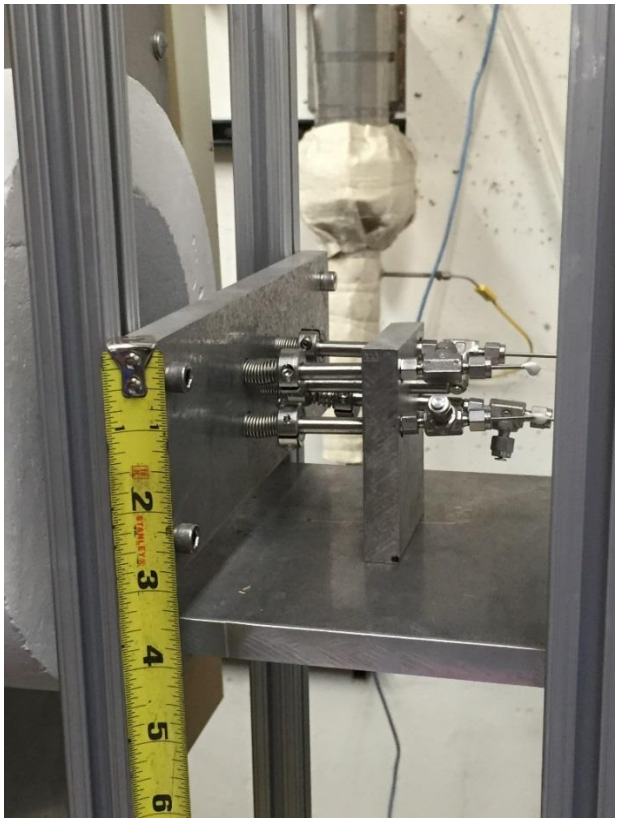

Figure 67: Thermal expansion spring plate picture

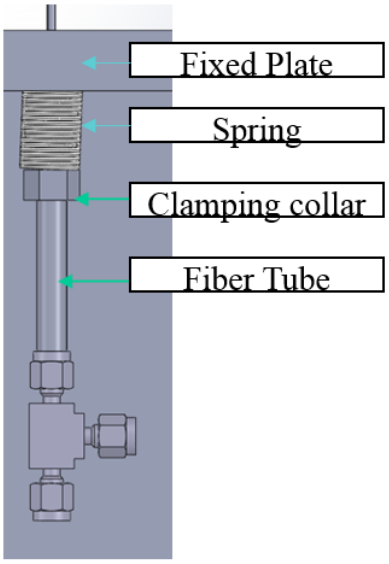

Figure 68: Thermal expansion spring plate CAD drawing

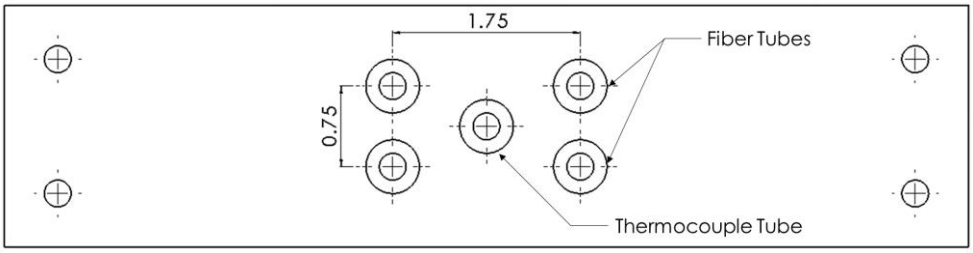

Figure 69: Thermal expansion plate, location of fiber and thermocouple tube mounting

Optical Fiber Frequency Shift vs Furnace Temperature

Wood et al at Ohio State found a second order polynomial function to calculate temperature from frequency shift for the acrylate coated fiber used in this work, given here as Eq. (7) [11].

$$T = (-1.33\times10-4)S^2-(0.748)S-0.229 \qquad (7)$$

Where T is temperature in degrees centigrade and S is the frequency shift in GHz.

Looking at equation 1, one notices that one must key a fiber at -0.229 C in order for the equation to read the correct temperature value with zero frequency shift. Therefore a fit function for the SMF-28e used in this work was found by fitting fiber frequency shift as a function of furnace temperature data. The fit function is referred to as Polynomial Fit 1 henceforth and is given as below in Eq. (8). The data used to acquire this fit is presented later in this section.

$$T = (\text{-}8.18\times10-5)S^2-(0.667)S+26.17 \qquad (8)$$

Optical fiber frequency shift as a function of furnace temperature for each fiber coating can be found in Figure 70. The quadratic fit found in Eq. (8) was also plotted and shows good agreement with the acrylate and polyimide/carbon coated fibers. A second order polynomial fit

was made for the polyimide coated fiber and is given in Eq. (9). This fit is referred to as Polynomial Fit 2 henceforth.

$$T = (-1.00\times10-4)S^2-(0.654)S+22.042 \quad (9)$$

High temperature testing was required prior to installation in the sodium loop to determine the fiber reliability and accuracy at temperature. Typically the maximum operating temperature of the sodium loop is 650 C. Furnace testing was thus performed at this temperature on each of the fibers listed in Table 9. A vacuum of <150 millitorr was pulled on each fiber tube in the furnace during heat up to ensure moisture and hydrocarbons from the coating burning off were removed from the environment. 20 PSIG helium was then backfilled after the fiber was at temperature for a period of 5 hours. The fibers were left in the furnace for a period of 300 hours per heat cycle.

One can see that there is a drift in frequency shift at 650 C for each fiber in Figure 70, where data from the first 50 hours of the first heat cycle have been plotted. Figure 71 shows a zoomed in view of this frequency drift.

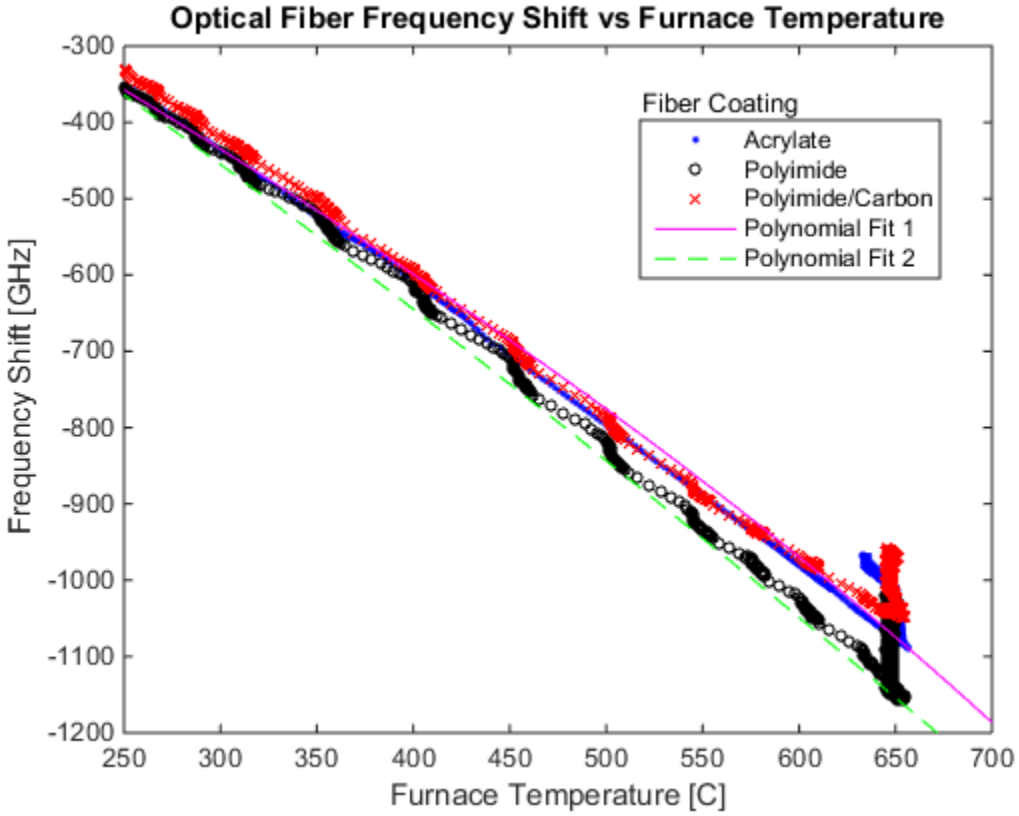

Figure 70: Frequency shift vs furnace temperature

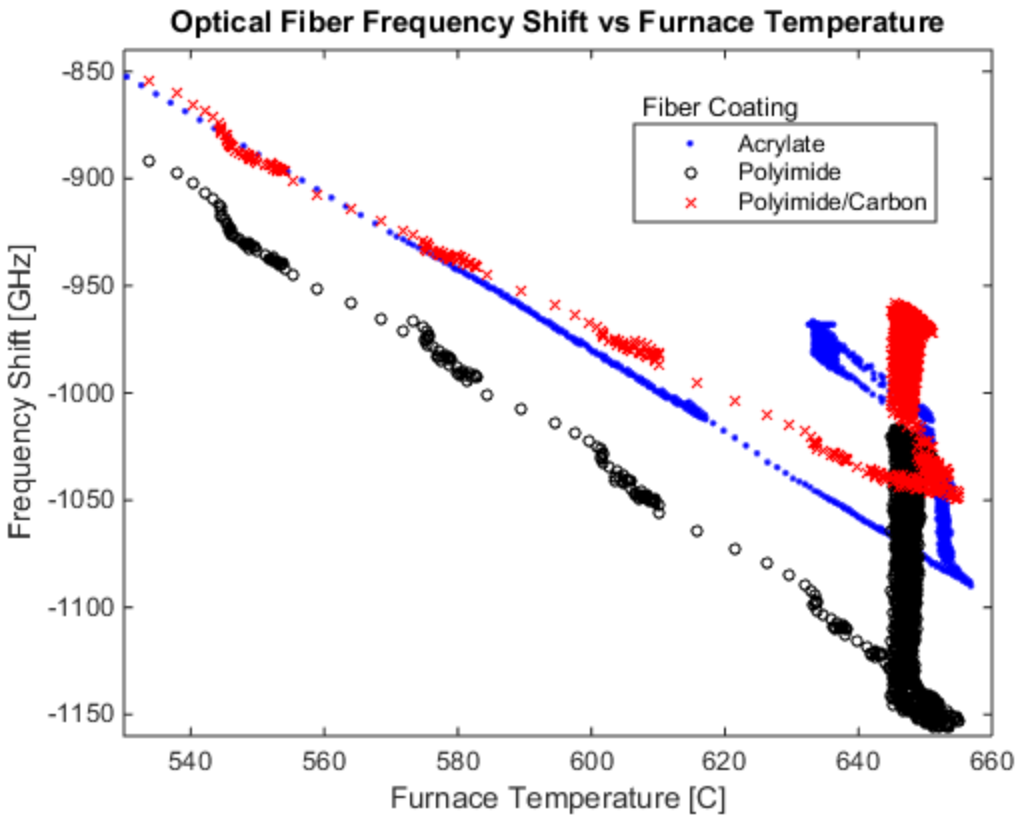

Figure 71: Frequency drift of fibers at temperature

In order to rule out the fiber optic coating's contribution to frequency drift a section of coating was removed from the optical fiber prior to testing. Fiber optic strippers were used to mechanically remove a 10 cm section of acrylate off of an acrylate coated fiber. The frequency shift versus furnace temperature for an optical fiber gauge located in the coating free region is shown in Figure 72. Frequency drift vs time for the bare fiber was plotted in Figure 73. One can again see the frequency drift occurring in a bare fiber during its first heat cycle. The drift amounts to around 60 GHz of drift at 650 C. This means that initially the fiber would read the correct 650 C system temperature, but over time would drift to incorrectly read temperatures of ~620 C. After bringing the fiber back to room temperature and rekeying there appears to be little to no drift at temperature, as can be seen in Figure 72 and Figure 73. A plot showing furnace temperature as a function of time for the first 70 hours of the testing is given in Figure 74. A plot showing the heatup and cooldown frequency shift as a function of furnace temperature can be found in Figure 75.

An annealing effect seems to be occurring at the scattering sites which appear to be permanent in the fiber during subsequent heat cycles. The frequency drift is consistently positive (lower temperature) thus the annealing seems to lead to a shrinkage in the fiber core as scattering sites are brought closer together. This means that if a fiber is installed in a system, such as a sodium loop, one can expect frequency drift and if the fiber is to be used for temperature acquisition over long periods of time (10 hours +) it should be annealed prior to installation. The fiber could be annealed in situ, however this requires the fiber to be exposed to system temperature for a period of 60+ hours, then brought to room temperature for rekeying. Annealing a fiber prior to installation poses a great challenge as the silica becomes extremely brittle after being exposed to high temperature. The silica breaks easily when attempting to install in anything other than a straight

tube geometry. If one is not able to anneal, a reference thermocouple may be installed in close proximity to the fiber in the system at temperature. This thermocouple allows one to adjust the fit curve over time as it appears to be a simple addition of frequency shift, as seen in Figure 75 the heatup and cooldown curves share the same shape and are just shifted with respect to frequency. A fit for an SMF-28e fiber after frequency shift was found using method of least squared residuals with an R-squared value of 0.99 for the data given in Figure 75. This fit is referred to as Polynomial 3 is included in Eq. (10).

$$T = (-1.28\times10-4)S^2-(0.690)S+87.15 \qquad (10)$$

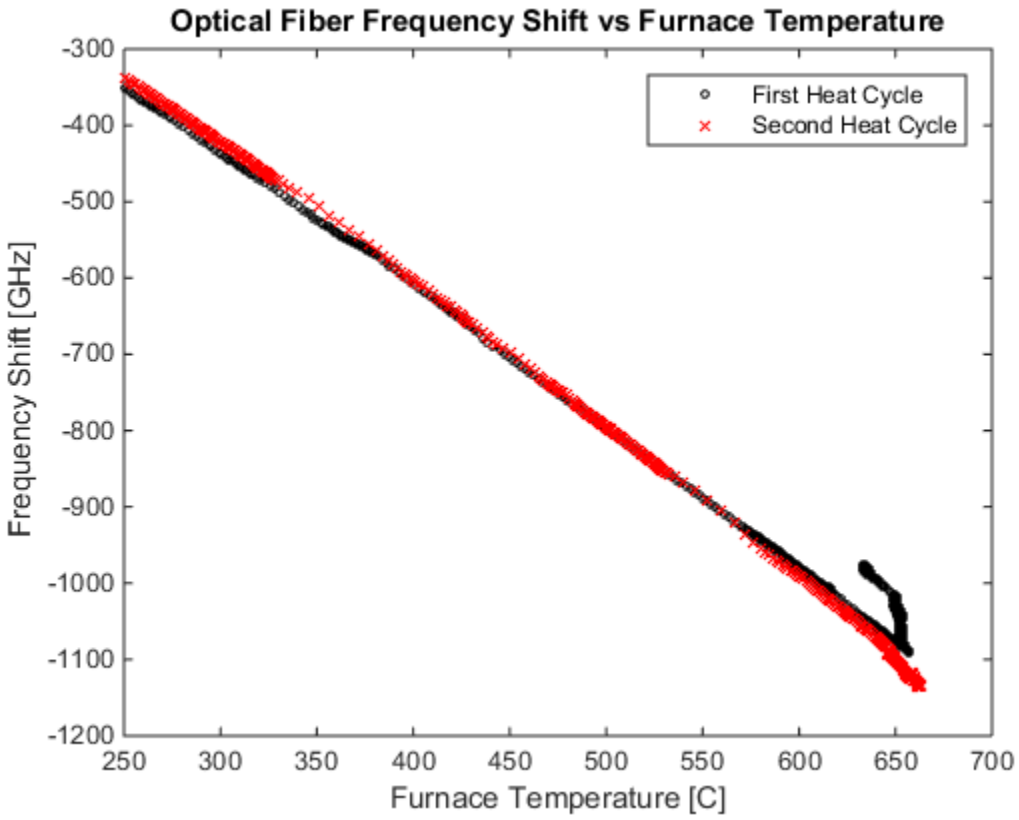

Figure 72: Optical fiber frequency shift vs furnace temperature. Acrylate coating stripped off before initial heat cycle.

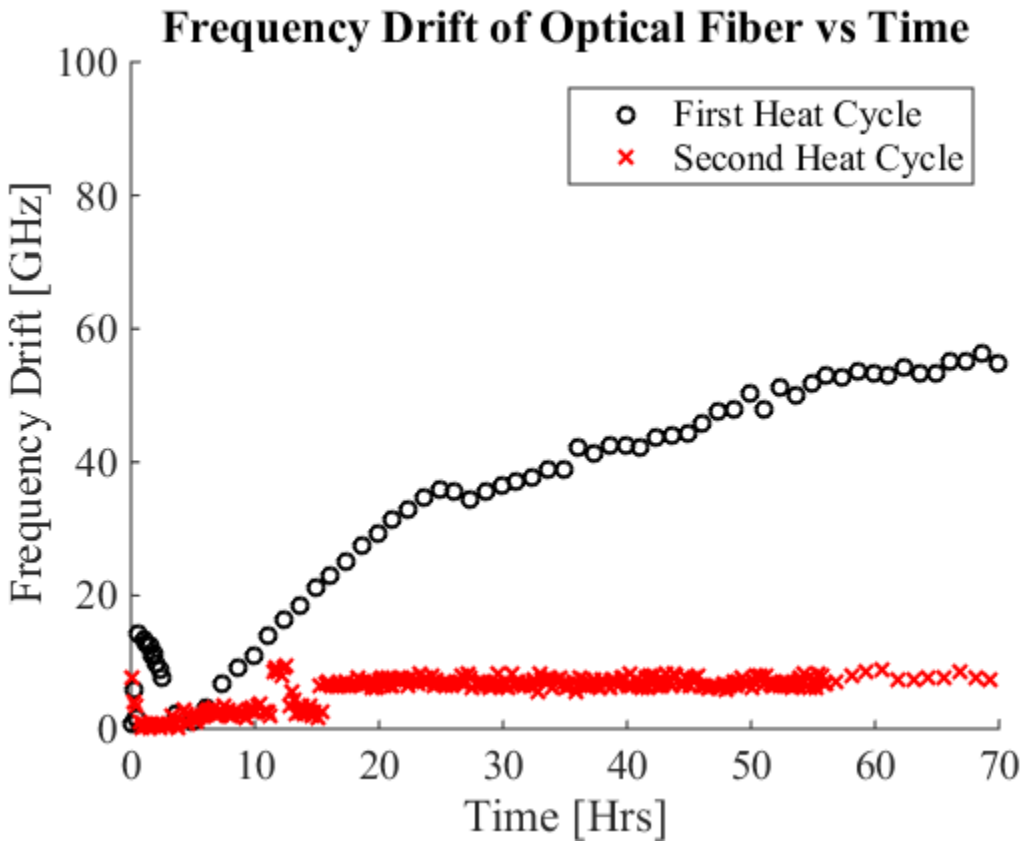

Figure 73: Frequency drift of optical fiber vs time

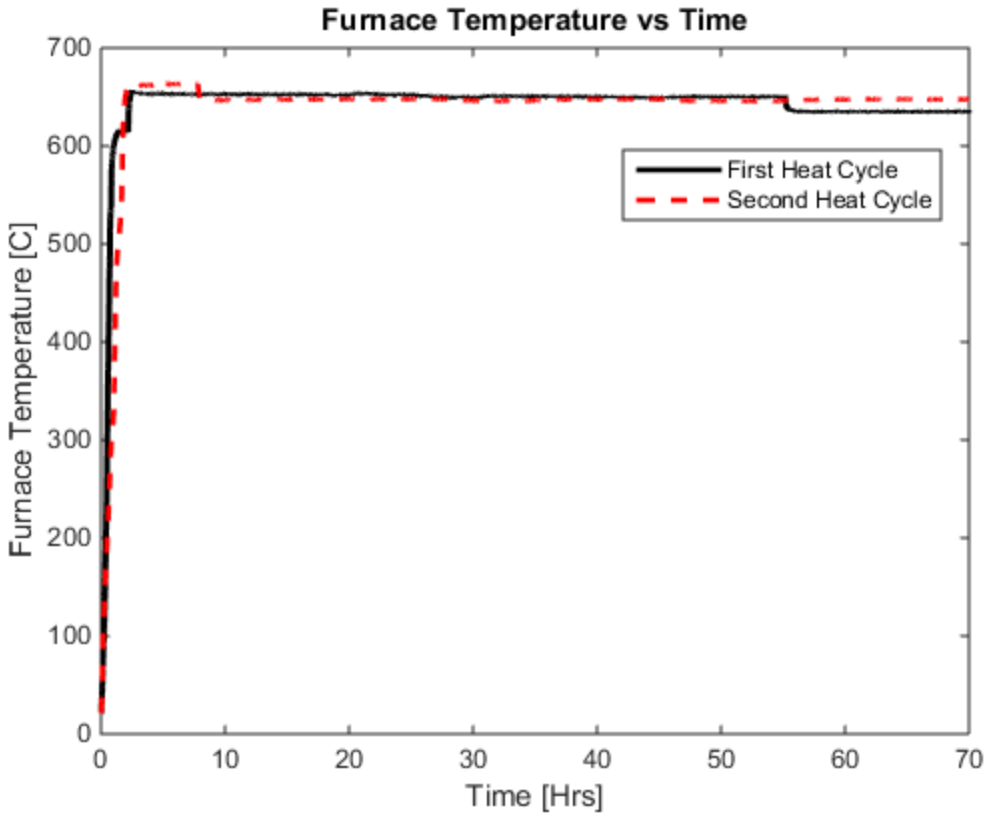

Figure 74: Furnace temperature vs time for acrylate coated fiber testing

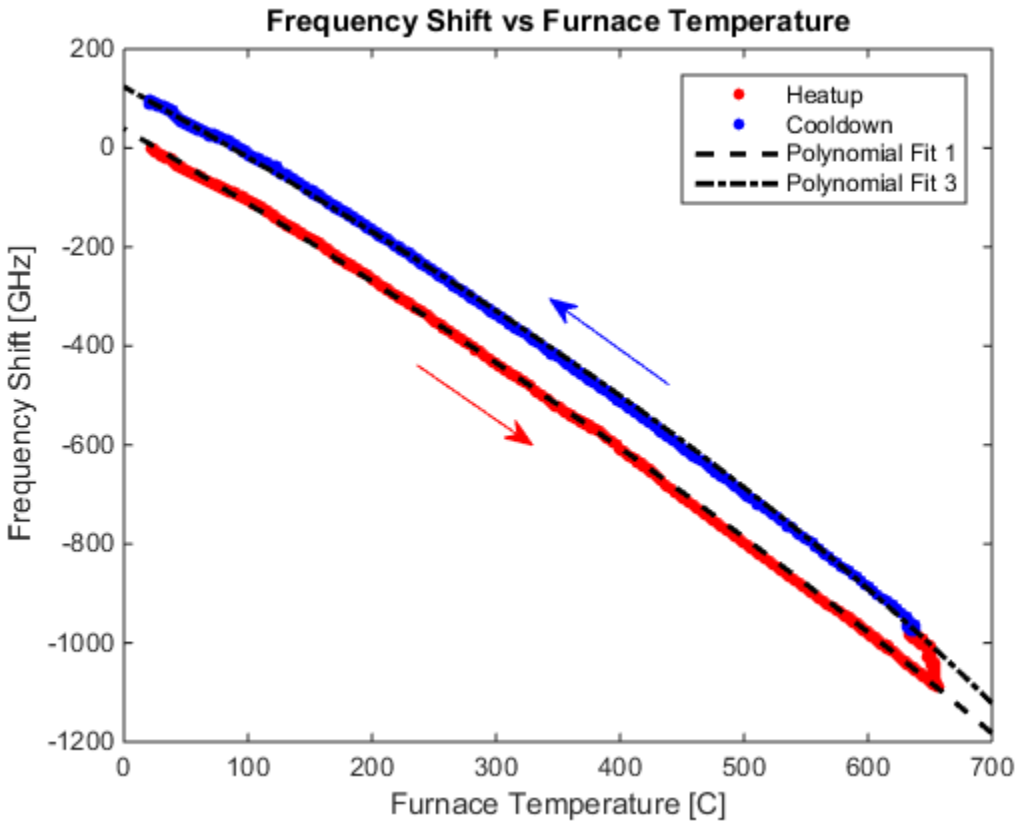

Figure 75: Frequency shift vs furnace temperature. Heatup vs cooldown, coating stripped fiber

The first and second heat cycle data from the previous figures were plotted on contour maps of fiber temperature vs location vs time, Figure 76 and Figure 77. The bare section where the acrylate coating was stripped off between 1 and 1.3 meters has been labeled. Notice that during the first 170 hours the initial heat cycle data is relatively noise free. There is a distinct discontinuity in the data at around 10 hours which was the fiber adhering and then releasing from the tube wall, as discussed later with Figure 79 and Figure 80. The noise beginning at around 170 hours in Figure 76 occurs in the same location, at approximately 1.5 meters, for the remainder of the test. This is likely due to scatter site mobility. The scatter sites have moved enough apart from eachother in the fiber core so that the interrogator can no longer cross correlate the correct Rayleigh backscatter peaks. It thus finds a higher correlation with scatter sites closer together, thus resulting in noise that is predominately low temperature, as seen in Figure 76.

After the first heat cycle of 300 hours the fiber was brought to room temperature and rekeyed before the second heat cycle. The bare section was labeled for posterity's sake, however it is safe to assume the coating has completely baked off the entire length of the fiber. There was little to no noise in the fiber data during the second heat cycle, as seen in Figure 77. This means the scatter sites are no longer mobile after annealing the fiber.

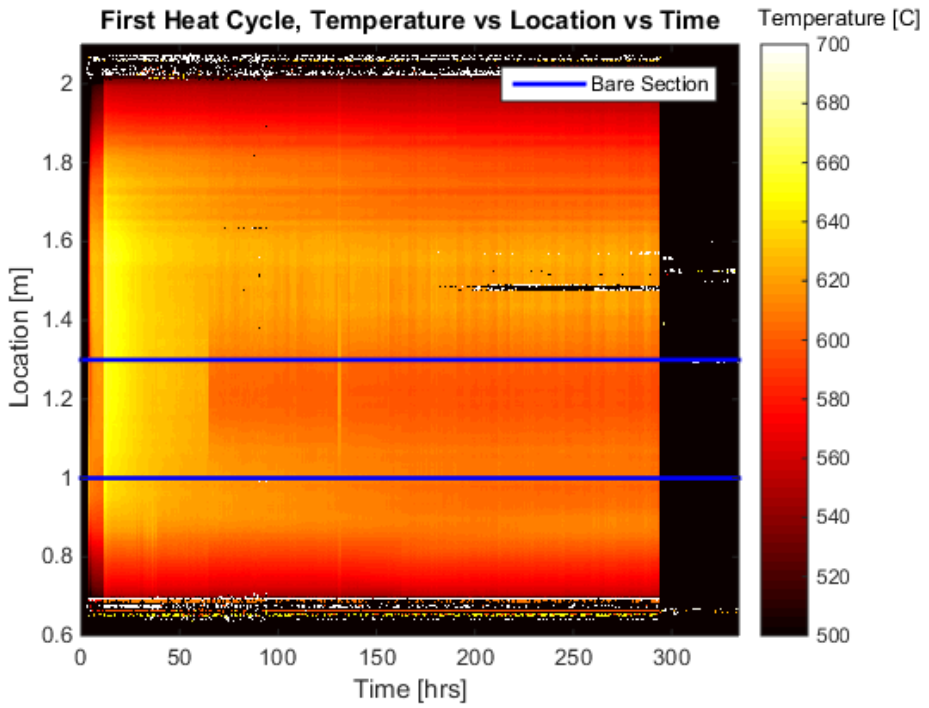

Figure 76: Temperature vs location vs time, first heat cycle of partially stripped acrylate coated fiber

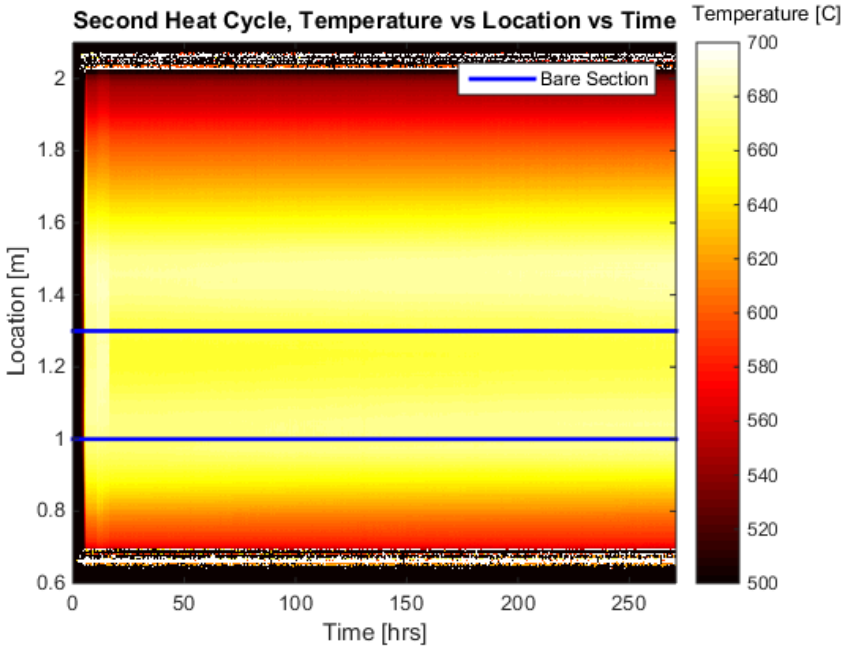

Figure 77: Temperature vs location vs time, second heat cycle of partially stripped acrylate coated fiber

A significant amount of noise was present at locations of high temperature gradients. One can see noise at the entrance and exit regions to the furnace as seen at 0.7 m and 2 m in Figure 76

and Figure 77. This noise is attributed to the very high temperature gradient seen in these regions, from room temperature to 650 ^{o}C over a few centimeters. As described before, the optical interrogator creates gauge locations along the fiber and measures the spectral shift with respect to reference at each of these locations. As these gauges are on the millimeter scale it is assumed that the entire gauge is exposed to the same temperature/strain condition. However when sharp gradients exist and the spectral shift becomes non uniform over the length of the gauge this results in poor correlation peaks relative to the noise floor. According to applications engineers at Luna Innovations, the interrogator cannot distinguish between the shifted spectral peak and the noise floor and therefore picks a random peak which has a higher correlation—producing wild and random temperature fluctuations. This issue does not affect the spectral shift readings outside of the high gradient areas.

Optical Fiber Coating Disintegration

Acrylate and polyimide coated optical fibers were tested throughout this work at high temperature. The acrylate had a maximum manufacturers rated temperature of 85 C while the polyimide had a maximum rated temperature of 300 C. Figure 78 presents a photo of a series optical fibers with each plastic coatings. The fibers were placed in a box furnace and the temperature was raised 50 C every hour. Before raising the temperature a fiber was removed for inspection. One can see that the acrylate coated fiber looks to begin disintegrating at 200 C with a change in appearance from translucent to an opaque brown color. The acrylate then begins to turn black and begin to flake off of the silica cladding at higher temperatures. The polyimide appears to begin disintegrating at 300 C with a gradual change in color from a translucent yellow to darker brown and then black.

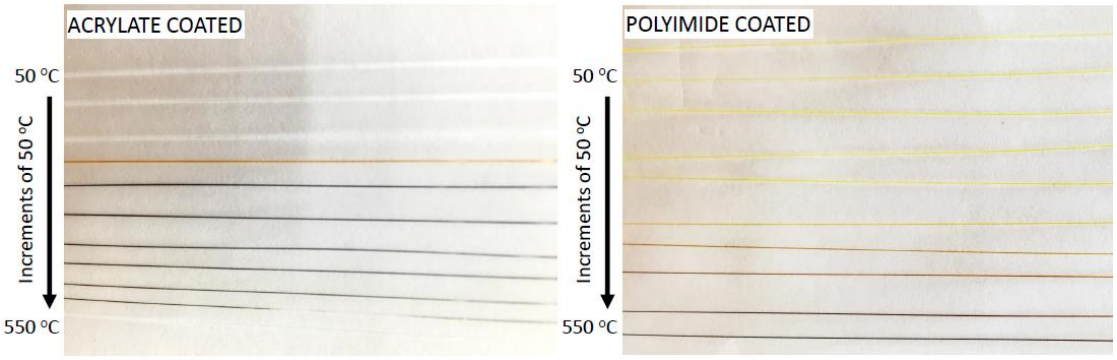

Figure 78: Plastic coating disintegrating at high temperature. Furnace raised 50 C every hour

The disintegration of the coating at high temperature can lead to issues if the coating begins to fuse to the side of the tube housing the fiber. This phenomenon was seen during a test of an acrylate coated fiber housed in a ¼" tube with 0.049" wall thickness. The fiber was in a furnace being heated to 650 C at approximately 10 degrees per minute. Figure 79 show the frequency shift as a function of furnace temperature for a fiber gauge which is located between the adhered fiber and the epoxied fiber inlet. Each gauge between these two fixed points reads a lower shift value (higher temperature) due to mechanical strain as the housing tube expands due to thermal expansion. Figure 80 shows the frequency shift as a function of fiber length immediately before and after a fiber releases, with the epoxied inlet and adhered location labeled.

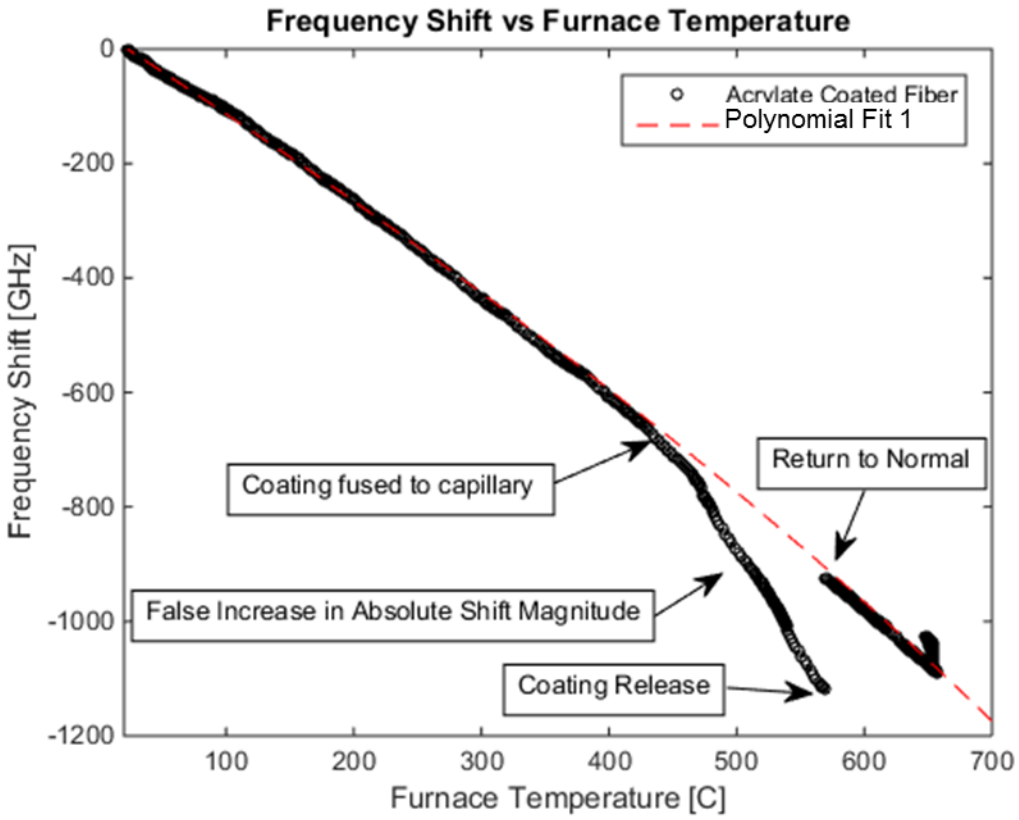

Figure 79: Acrylate coating fusing to housing tube at ~400 C then releasing at ~580 C

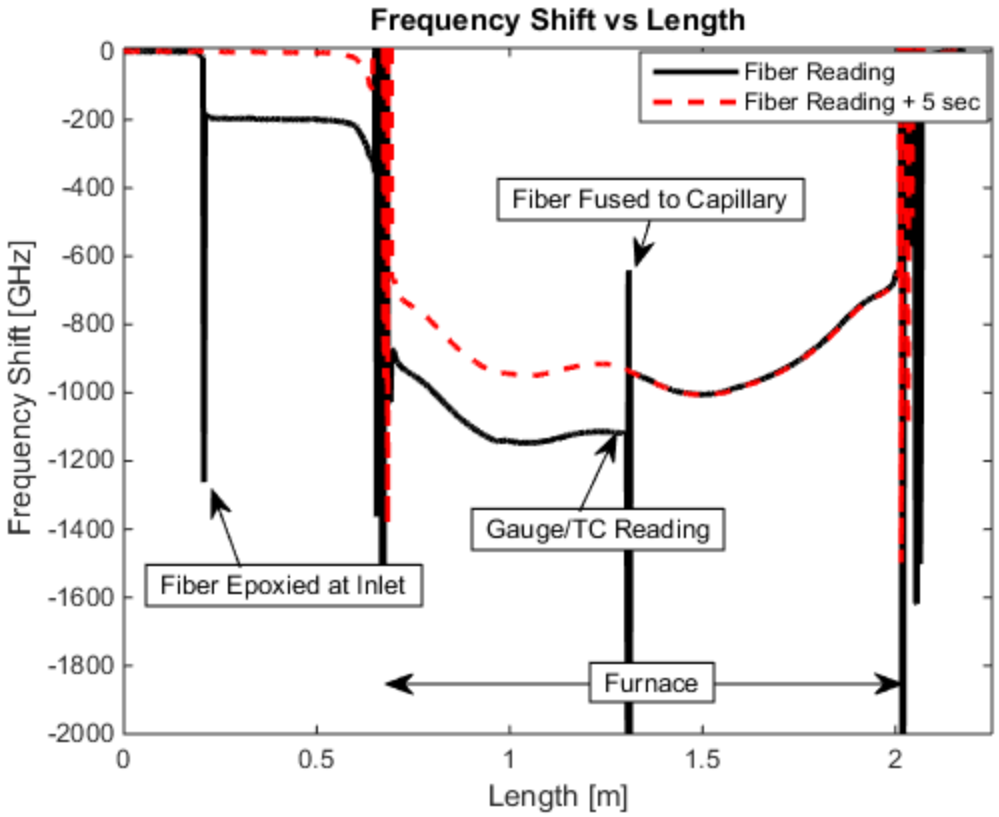

Figure 80: Frequency shift vs fiber length. Plot shows moment before and after fiber releasing from being fused to tube wall

Figure 81 gives the optical fiber gauge temperature data fitted with Polynomial Fit 2 along with the furnace thermocouple temperature as a function of time for a polyimide fiber. The fiber was encapsulated in a ¼" tube with a 20 PSIG backfill after 150 millitorr vacuum was pulled. For experiments where there is limited exposure of the fiber to high temperature the frequency drift issue previously discussed is not apparent. This test was run for 60 hours and ramped up to 700 ºC maximum oven temperature with a polyimide coated fiber. A section of the data in Figure 81 can be seen in Figure 82 for the high temperature polyimide coated fiber test from 12-22 hours. As can be seen when the oven ramps up to 500ºC there is a gradual drop in fiber temperature of around 15 ºC, which corresponds to a shift in frequency towards the reference of 30 GHz. Given the temperature is steady according to the thermocouple data of figure 17, and this phenomenon has been seen at this temperature in other test runs, this shift is likely attributed to a cladding-coating interface interaction. This temperature is a point at which the polyimide readily decays as was seen in Figure 78. Shrinkage of the polyimide as it carburizes is the most likely mechanism inducing the measureable mechanical strain on the optical fiber.

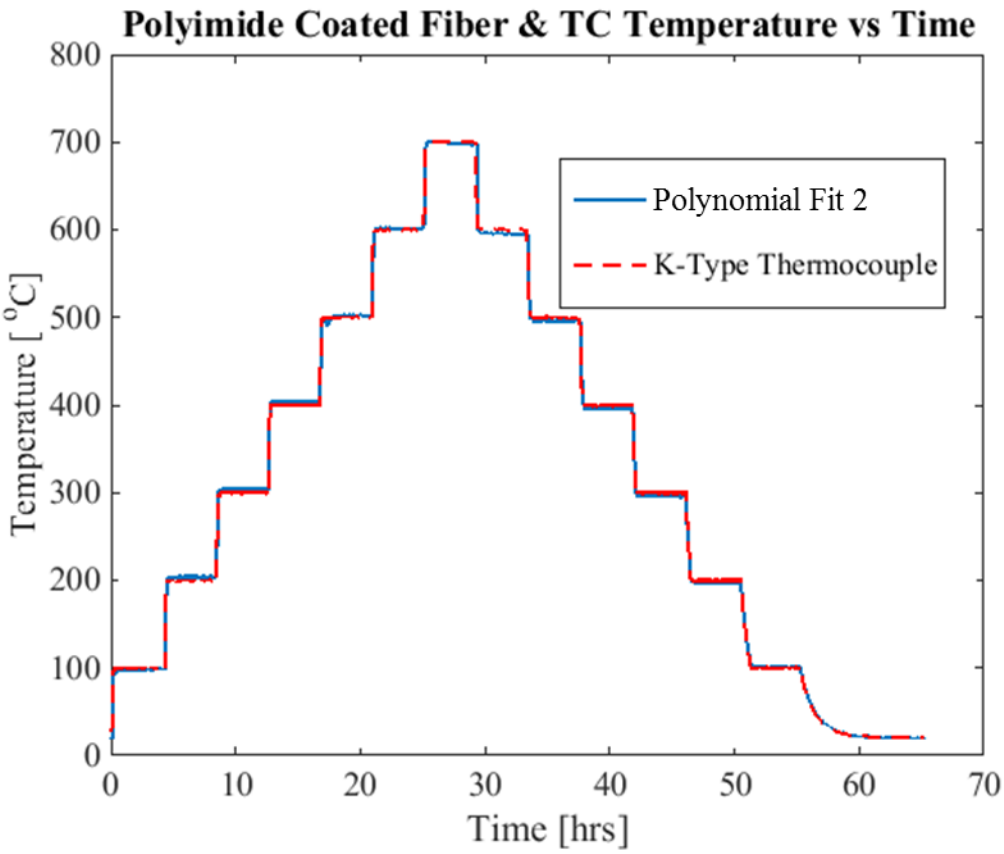

Figure 81: Furnace test of polyimide fiber up to 700 C.

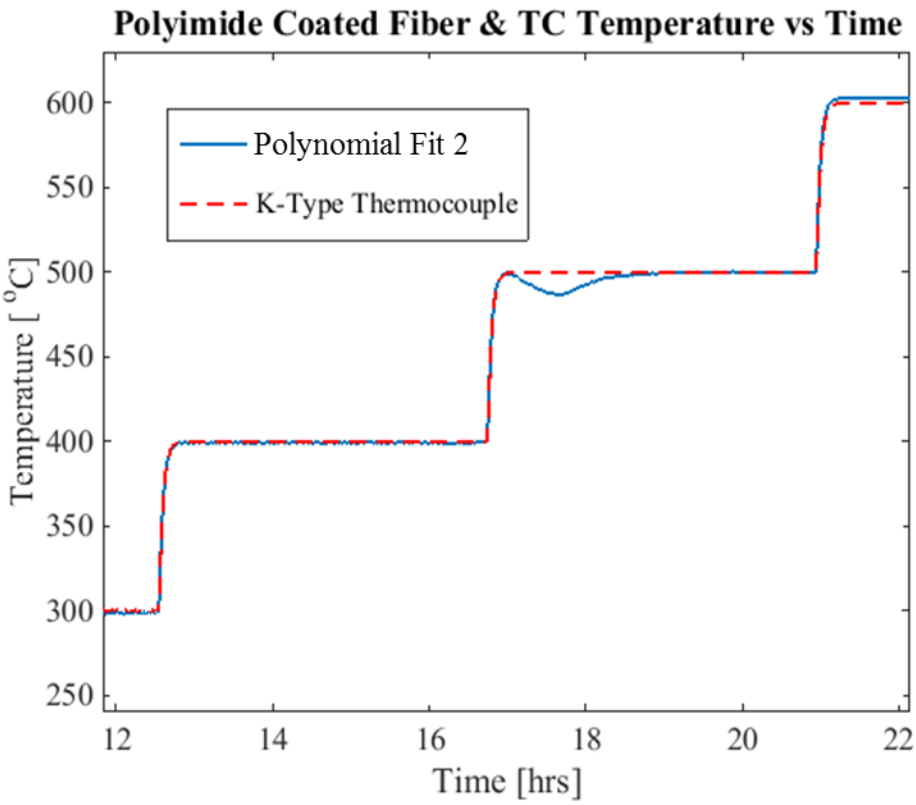

Figure 82: Polynomial coating shrinkage and release from cladding

Testing was done with the polyimide/carbon coated fiber in the sodium loop at 600 C, Figure 83. One can see where the fiber was inserted into the loop from 0.8 m to 2.3 m. Large spikes in temperature data are immediately apparent at particular locations in the temperature profile. Analysis was done on the optical fiber after testing was complete with an optical microscope, Figure 84. One can see that the polyimide coating has burned off leaving the carbon undercoat. The difference in thermal expansion between the silica fiber and carbon coating may have caused buckling the carbon as seen in Figure 84. This may have imposed micro bending in the silica core, thus inducing noise in the temperature profile. This issue was not as apparent without the carbon undercoat.

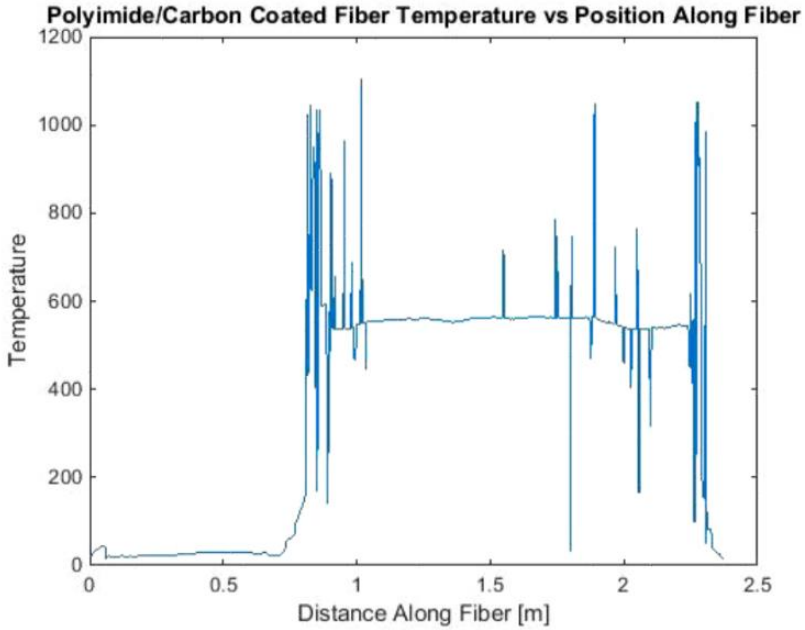

Figure 83: Temperature vs position of optical fiber deployed in sodium loop

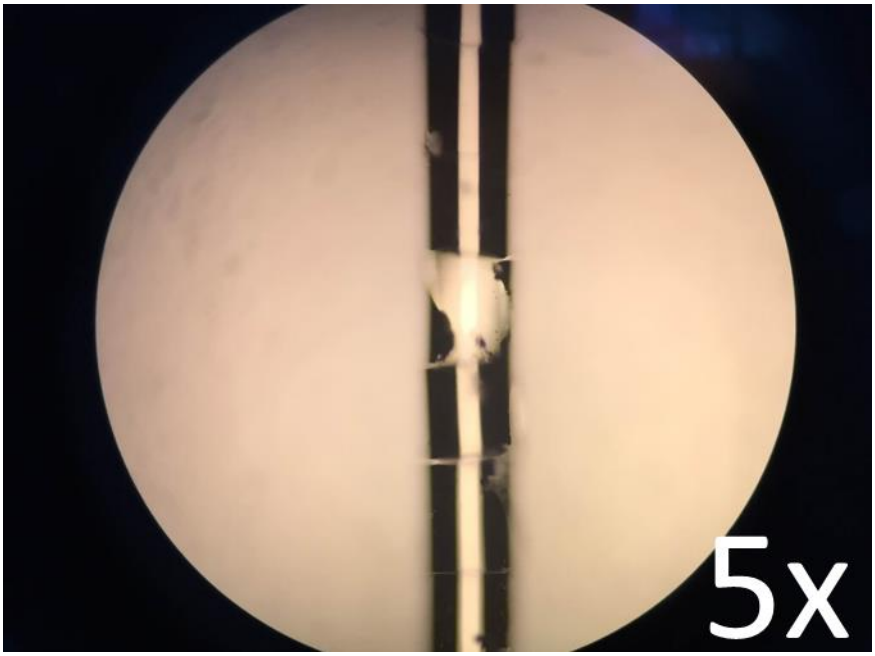

Figure 84: Polyimide/carbon coated fiber removed from sodium loop

Optical Fiber in Capillary Thermal Transient Response

Introduction

Deploying optical fiber sensors in harsh environments which would otherwise destroy the silica fiber requires the use of a protective sheath such as a stainless steel capillary. This capillary introduces a thermal barrier, reducing the response time of the optical fiber and with it the ability to observe phenomena which occur at high frequency. Therefore work was done to assess the effect the protective capillary has on thermal response time of the optical fiber temperature sensor. This was done by using a laser to impose a periodic heating cycle on a fiber in capillary with inert gas back fill and on a conventional K type thermocouple of similar geometry.

A method of applying constant laser heating power with an optical chopper in series to induce a known laser frequency on the surface of the temperature sensor has been devised. The discrete Fourier transform of the time dependent temperature signal can then be taken to analyze the frequency signal to extract the known laser frequency from the sensor data. The optical chopper frequency is increased until the discrete Fourier transform (DFT) does not reveal a peak with significant prominence over the noise floor. This can be calculated by finding the signal to noise ratio of the expected frequency peak in the DFT. This maximum frequency can be thought of as the maximum frequency response of the sensor and this can be used to optimize the sensor for use in high thermal transient systems. In order to determine the feasibility of implementing an optical fiber system to accurately capture high frequency thermal phenomena the maximum frequency response of an optical fiber in capillary should be found.

Laser Flash Method Frequency Response Setup

In order to protect the optical fiber from potentially hazardous system conditions it must be sealed from the environment. A method for encapsulating the optical fiber in a type 316 stainless steel capillary tube was discussed earlier and was shown in Figure 54 and Figure 59. The capillary tube used in this experiment was from Valco Instruments Co. and has an outer diameter of 0.80 mm (1/32”) and an inner diameter of 0.51 mm (0.020”). The manufacturer uses a hexane based solvent to clean the inner wall of the capillary tubing to eliminate any contaminants.

A Model 95 argon ion laser from Lexel Laser Inc. was used to provide radiative heating for the laser flash method. A Digired C-980 Optical Chopper was placed in series with the laser beam, as seen in Figure 85, to modulate the laser beam at a known frequency. The laser was setup to operate at 488 nm wavelength and was tuned with a Molectron PowerMax 5200 optical power meter to maintain a consistent laser power after the optical chopper.

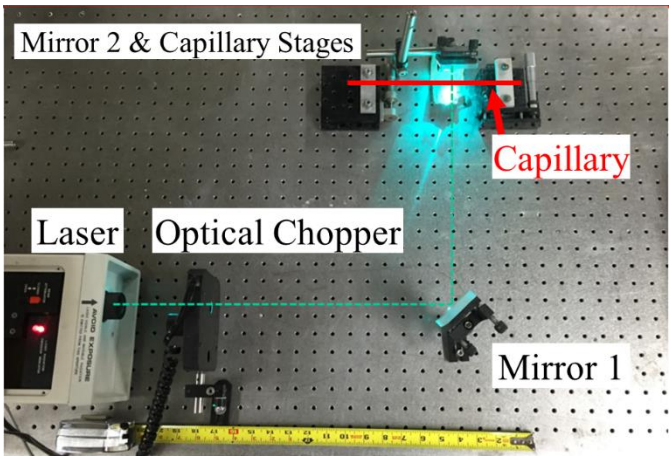

Figure 85: Labeled photograph of setup for laser flash method.

Figure 85 shows mirror 1 and 2 directing the laser beam perpendicular and downward from original emitted direction, respectively. A pair of two axis optical stages were used to rigidly mount the fiber-in-capillary setup, shown with a red line for clarity in Figure 85, at a height of approximately 2.5 cm above the optics table. A photodiode was mounted under mirror 2 and was used to trigger the ODiSI-B to begin acquiring Rayleigh backscatter data when the laser was actuated on. The mirrors and stages were used to center the manufacturer rated 1.3 mm diameter laser beam on the temperature sensor.

Figure 86 shows a typical temperature vs location profile for both helium and nitrogen backfilled fiber in capillaries with laser beam power at 1700 mW. In order to perform the Fourier transform to reveal the frequency spectrum a reference gauge was chosen for the fiber at the peak of the temperature curve, as labeled in Figure 86. This gauge's temperature vs. time data (for a period of 10 seconds at steady state) was transformed to the frequency domain for analysis.

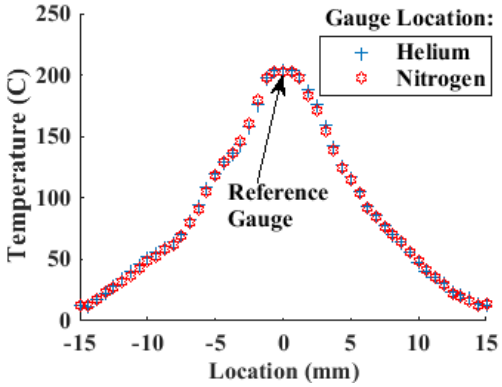

Figure 86: Temperature vs location for fibers in capillary with helium and nitrogen backfill. High resolution acquisition mode. Chopper frequency set to 7 Hz. Laser power set to 1700 mW. Reference gauge at 0 mm.

Temperature Sensors Tested

The three temperature sensors tested with the laser flash method described above were: K type sheathed thermocouple, optical fiber in 1/32" capillary with helium cover gas, and an optical fiber in 1/32" capillary with nitrogen cover gas.

The K type thermocouple used throughout this work had a 316SS sheath with an OD of 1/32” and an ID of 0.025”. This is close to the capillary tube used to house the fibers with an OD of 1/32” and an ID of 0.020”. The potting material filling the thermocouple sheath was MgO.

SMF-28e optical fiber was used throughout these experiments. The acrylate coating was stripped off of the fiber located inside of the capillary tube. The bare optical fiber was placed in the capillary tube and helium set to 20 PSIG at the regulator on the bottle was allowed to enter the capillary environment through the cover gas port labeled in Figure 54. The helium was allowed to exit the capillary through the termination end cap. The helium was allowed to flow for a period of approximately 10 seconds, thus pushing out the air in the capillary. The termination end was then sealed and the regulator set to 20 PSIG helium. This process was also done with nitrogen backfill.

The high resolution mode, with 23.8 Hz acquisition rate was used throughout these experiments. This gives a Nyquist frequency of 11.9 Hz. The temperature gradient imposed by the laser was too great for the other modes with a larger gauge spacing and faster acquisition rate.

Results

Temperature data was sampled by the 1/32” thermocouple probe at 50 Hz. Temperature was at steady state to eliminate superfluous noise when the discrete Fourier transform was calculated for a period of 10 seconds to acquire a frequency spectrum as seen in Figure 87. The optical chopper was set to modulate the laser power over a range from 4 to 8 Hz at 1 Hz intervals. Laser power was set to 1700 mW. The amplitude for the following Fourier transformed frequency spectrums in this paper are normalized with respect to the peak at the lowest chopper frequency.

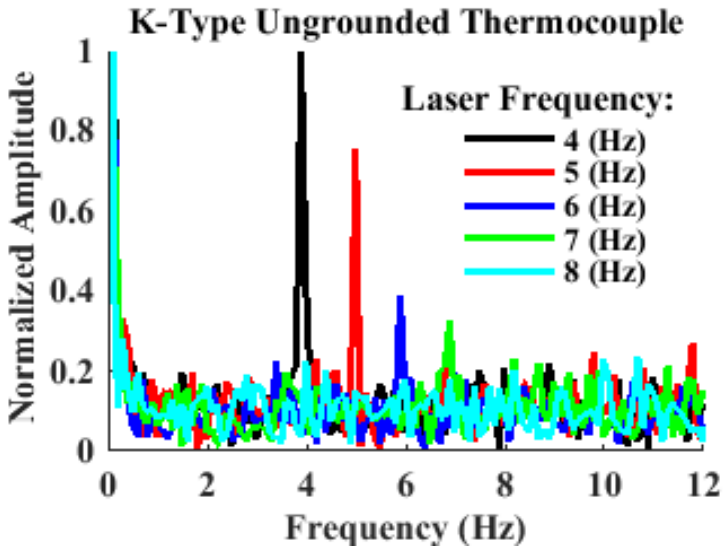

Figure 87: Discrete Fourier transform from time to frequency domain. K type ungrounded thermocouple probe. Laser power set to

Figure 88 and Figure 89 depict the frequency spectrum for a bare fiber in capillary with 20 PSIG helium and nitrogen backfill, respectively. Laser power was set to 1700 mW, the same as the thermocouple probe.

A maximum detectible laser frequency of 11.7 Hz was found for helium backfilled capillaries. A maximum detectible laser frequency of 8 Hz was found for nitrogen backfill.

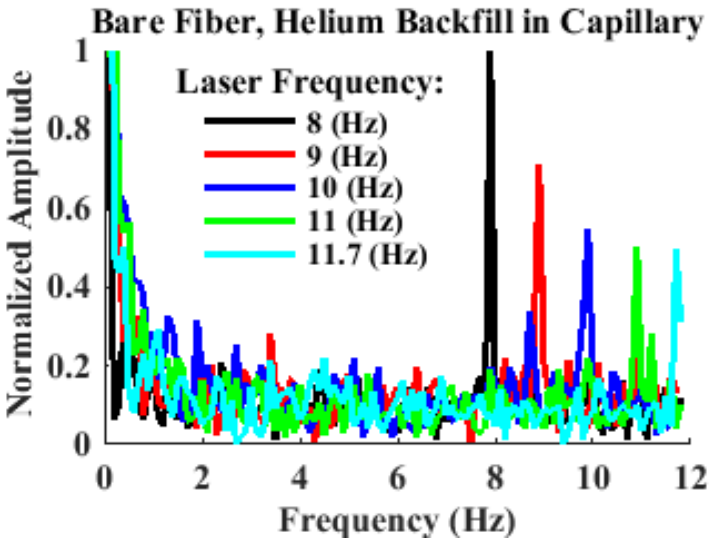

Figure 88: Discrete Fourier Transform from time to frequency domain. Fiber in capillary with 20 PSIG helium backfill. Laser power set to 1700 mW.

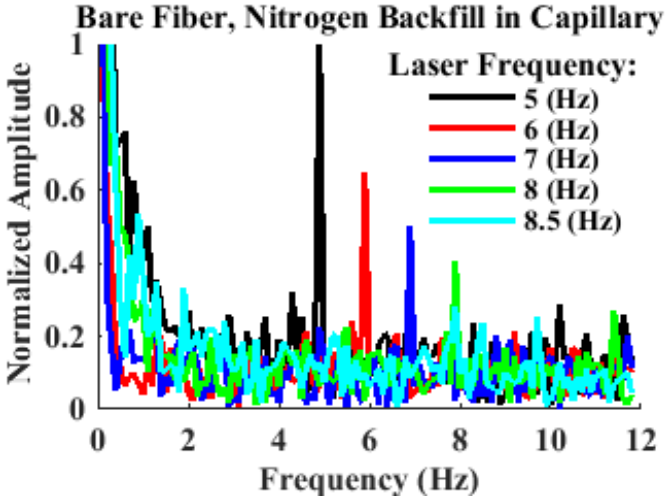

Figure 89: Discrete Fourier Transform from time to frequency domain. Fiber in capillary with 20 PSIG nitrogen backfill. Laser power set to 1700 mW.

The results from the frequency spectrum given above have been summarized in Figure 90 by finding the signal to noise ratio of the peaks with respect to the noise floor for Figure 87, Figure 88, and Figure 89. This gives the qualitative results that the optical fiber sensors in capillary with inert cover gas can discern high frequency phenomena as good as conventional thermocouples.

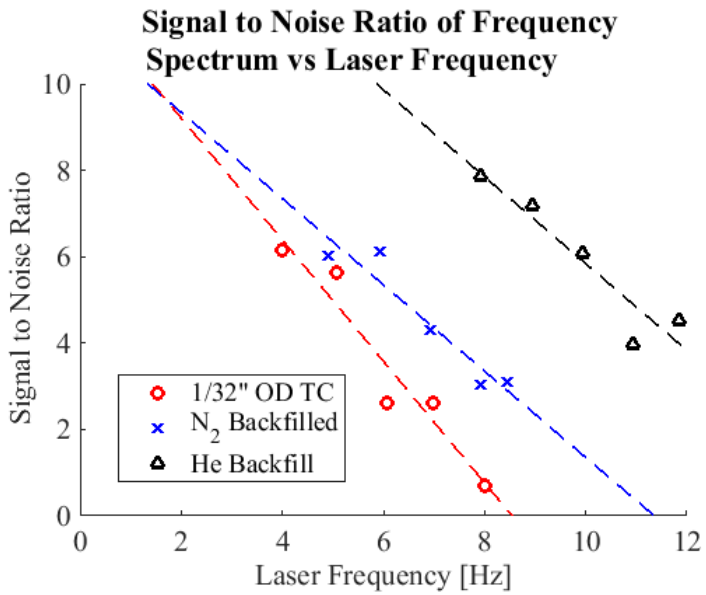

Figure 90: Signal to noise ratio of frequency spectrum for temperature sensors tested

Maximum Temperature gradient

While performing the above experiments it was found that there was a maximum temperature gradient for each acquisition mode, depending on the mode's gauge length. Outlying temperature data, usually orders of magnitude off, results at a particular gauge length when there is a great temperature gradient occurring within the confines of the gauge- causing the system's algorithm to not be able to cross correlate the distinct frequency shift properly [8]. Therefore, in order to determine the maximum temperature gradient for each mode, the laser power was slowly increased until an outlying data point was found and the temperature between the gauge lengths next to the outlier was used to determine the gradient, as can be seen in the sample data of Fig. 4.

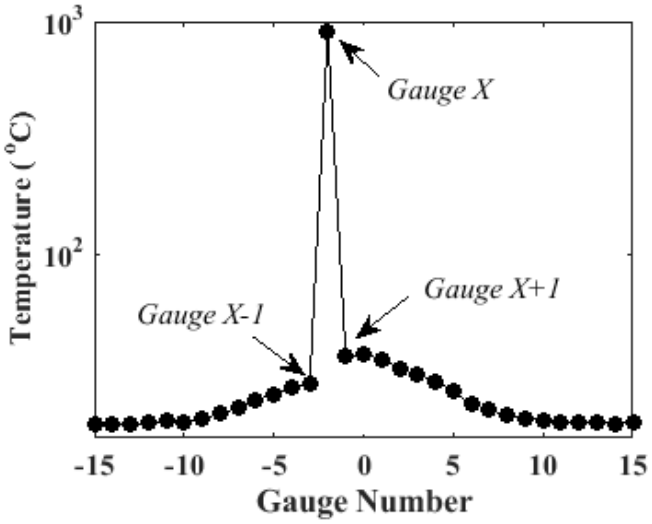

Figure 91: Error in cross correlation of Rayleigh backscatter peak at Gauge X

Notice that the outlier occurs at Gauge X. The maximum temperature gradient can then be found using Eq. (11).

$$\left[\frac{\Delta T}{\Delta l}\right]_{max} = \frac{T_{X+1} - T_{X-1}}{Gauge\ Spacing} \tag{11}$$

Where T_{X+1} and T_{X-1} refer to the temperatures at the labeled gauges in Figure 91 and the *Gauge Spacing* is a system property defined in Table 8 as sensor spacing. The maximum temperature gradient was calculated for each sensing mode by increasing laser power from 0 to 600 mW aimed at a carbon/polyimide coated fiber without capillary. The rate of power ramp up was performed by hand by increasing the current input to the laser at approximately 10 mW/s. The temperature profile was monitored in real time during this ramp up and when outlying temperature data was detected, 5 consecutive outliers and their respective gradients were collected for each mode and can be found in Table 11.

Table 11: Maximum measurable temperature gradients

Sensing Mode: *Acquisition Rate / Gauge Length*	**Maximum Temperature Gradient** ($^{\circ C}/_{mm}$)
23.8 (Hz) / 1.25 (mm)	84.50 ± 12.34
50 (Hz) / 5 (mm)	2.73 ± 0.28
100 (Hz) / 5 (mm)	2.46 ± 0.11
250 (Hz) / 5 (mm)	2.16 ± 0.38

Fiber in Capillary Thermal Response Time Computer Model

A study was performed with Ansys to determine the approximate thermal response time of an optical fiber temperature sensor in stainless steel capillary when exposed to a 5°C thermal transient. The thermal time constant is the speed at which a temperature sensor can respond to a change in system conditions. This time constant is calculated by finding the amount of time it takes to reach a factor of 1-1/e of the system condition (approximately 0.632). Therefore the thermal response time constant of a 5°C step change is calculated as the time it takes for the temperature to increase 3.16°C from initial temperature (0.632 * 5°C).

Figure 92 shows the computer model geometry and Table 12 includes material properties used for this simulation. A 1.5 mm length of capillary was used for simulation with an initial temperature of the entire geometry set to 600°C. A boundary condition of 605°C was then applied to a 0.5 mm length in the center along the circumference of the stainless steel capillary. Temperature was monitored in the center of the silica fiber to determine the time constant. The immediate 5C increase in boundary temperature is assumed reasonable given sodium's high convection coefficient (~30,000 W/m^2 K) and low Prandtl number (<0.1). Results for thermal response time for a variety of capillary geometries can be found in Table 13.

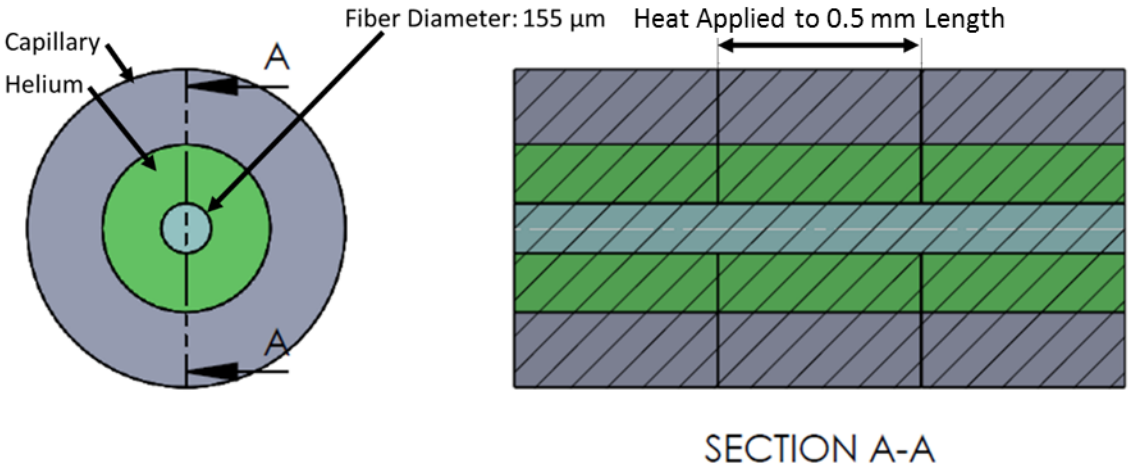

Figure 92: Fiber in Capillary Front View and Cross Section

Table 12: Fiber in Capillary Simulation Material Properties

Material	Density [kg/m3]	Therm. Conductivity [W/mK]	Cp [J/kg K]
SS 316	8000	20	500
Helium	.164	.138	5190
Silica	2650	1.3	700

Note that given the relatively thin wall thickness of some to the capillary geometry simulated it is wise to approximate the approximate durability of the stainless steel in sodium over extended periods of time. Assuming sodium impurity level of 10 ppm oxygen and flow rate of 30 ft/sec one may assume a 1 mil/yr corrosion rate of the stainless steel, Figure 93 [8]. The approximate longevity of each of the geometries explored was included in Table 13.

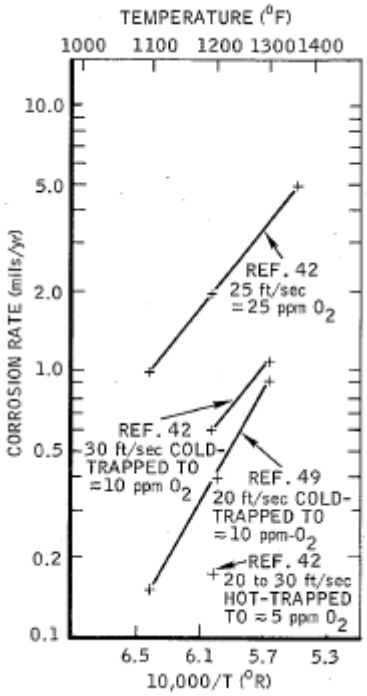

Figure 93: Corrosion Rate of 316SS in Flowing Sodium [8]

Table 13: Geometry Studied

Capillary #	OD [in]	ID [in]	Wall Thickness [in]	Aprox. Capillary Longevity [yr]	5 [C] Transient Response Time [sec]
1	0.06250	0.01000	0.02625	26.3	0.0820
2	0.03125	0.01000	0.01063	10.6	0.0355
3	0.03125	0.01650	0.00800	8.0	0.0475
4	0.03125	0.02000	0.005625	5.6	0.0550
5	0.02000	0.01000	0.00500	5.0	0.0260

THERMAL STRIPING ANALYSIS

Introduction

A unique challenge in sodium systems is thermal striping. This phenomenon is characterized by temperature oscillations occurring on the order of 0.1-10 Hz at hot and cold stream junctions [12]. This oscillating temperature field is created by jet instabilities and turbulence in the flows and exacerbated by sodium's low Prandtl number. These rapid and continuous temperature perturbations may result in structural damage due to increased thermal stress cycling. This is due to the austenitic steel construction material possessing a high thermal expansion coefficient and relatively low thermal conductivity, as compared to sodium. While thermal striping has been studied with conventional thermocouples, new advancements in temperature sensors allow for finer spatial and temporal resolutions of this phenomenon.

There have been many industrial case studies and experiments performed to study thermal striping as a failure mechanism in liquid sodium systems. In France's SPX-1, a failure of a circumferential weld downstream from a mixing tee in an auxiliary pipe of the secondary circuit was traced to thermal striping [13]. Additional recorded industrial failures include thermal striping induced cracking in a Phenix sodium pump vessel in France, control rod tube in the Prototype Fast Reactor in the UK, and a cold trap in the BN-600 reactor in Russia [14].

The first experimental studies on thermal striping commenced in 1982 with a project that characterized the conditions under which thermal striping caused structural damage to various structural configurations [15]. Further experimentation was performed by Kawamura et al. [16] and Yuki et al. [17] which focused primarily on thermal striping in tee junctions. The frequency behavior of thermal striping was explored by Ogawa et al. [18] and the effect of thermal striping frequency on surrounding structure by Jones and Lewis [19]. Thermocouples have been used in prior thermal striping experiments for temperature data collection prior to using optical fibers in this work.

Experimental Setup

The striping section can be seen labeled in the diagnostic loop of the schematic in Figure 94 and a more detailed drawing of the striping section can be found in Figure 95. This geometry directs two streams of sodium at independently variable flow rates and temperatures to impinge upon one another at a 90 degree angle to facilitate thermal striping behavior. Sodium from the plugging meter leg of the diagnostic loop feeds into the hot side of the striping section while sodium from the cold trap leg feeds the cold side of the striping section. A counter flow pressurized air heat exchanger, labeled "Striping Cooler" in Figure 94, has an electronically controlled variable orifice valve to provide fine control of the cooling air coming from the compressor. A K-type thermocouple immersed in the cold side sodium provided feedback for PID control of the cooling air valve. The hot sodium leg temperature, as well as the rest of the loop, is controlled via PID actuated heaters with a computer.

The two entry tubes have an inner diameter of 0.94 cm while the larger main mixing tube has an inner diameter of 2.21 cm. Three optical fibers were mounted concentrically in these tubes as seen, labeled fiber A1, A2 and A3 in Figure 95. The dimensionless entry length for turbulent flow can be used as an estimate to determine if flow is fully developed at a particular Reynolds number, Eq. (3) [20].

$$\frac{l_e}{d} = 4.4(Re)^{1/6} \tag{3}$$

Where l_e is the entry length and d is the tube inner diameter. Therefore, using the straight tube dimension given in Figure 95 of 8.82 cm and the tube inner diameter of 0.94 cm, one can calculate the maximum Reynolds number for fully developed flow to be only ~94. Thus the turbulent flow throughout these experiments is considered undeveloped or developing.

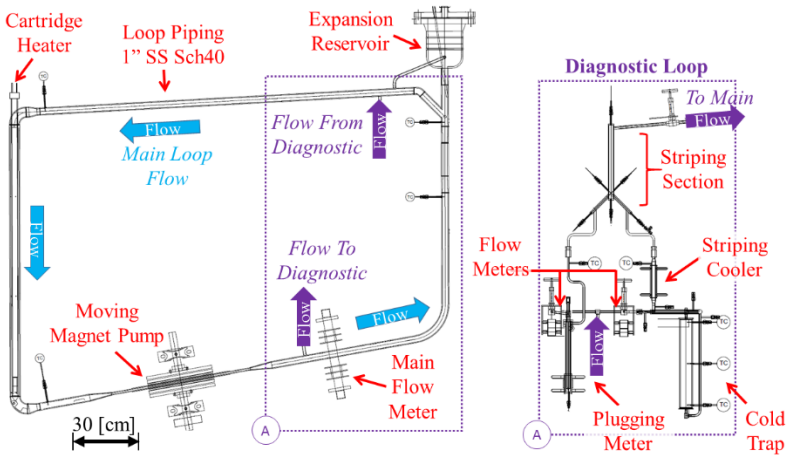

Figure 94: Sodium loop with thermal striping experiment

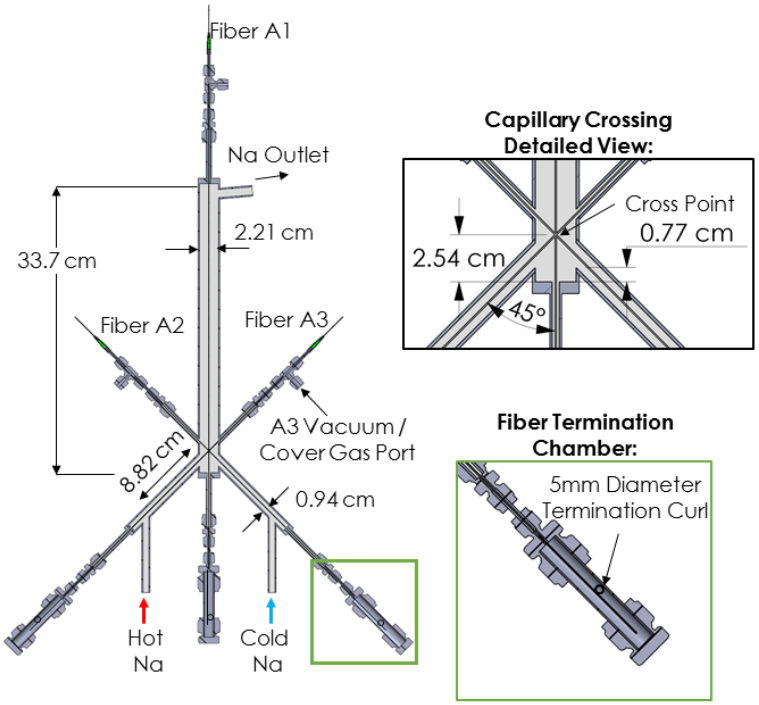

Figure 95: 90 degree junction thermal striping experimental setup

Classification of Flow Shape at Junction

It is important to predict and locate the position of thermal striping induced temperature oscillations at a flow junction because some regions are more sensitive to rapid temperature fluctuations than others. When high temperature oscillations occur in the bulk sodium they are a benign thermal phenomenon. Conversely, when close to a mechanical containment they can induce thermal stress and possibly component failure.

In order to classify flow patterns at the 90 degree intersection, momentum rates were calculated using Eqs. (4) and (5) for the hot and cold streams, respectively.

$$M_H = \frac{\pi}{4} D_H{}^2 V_H{}^2 \rho_H \tag{4}$$

$$M_C = \frac{\pi}{4} D_C{}^2 V_C{}^2 \rho_C \tag{5}$$

Where D, V and ρ are defined as the hydraulic diameter, velocity and density of the hot and cold inlet streams.

Momentum flow ratio of hot to cold flow at the junction can be found with Eq. (6).

$$M_R = \frac{M_H}{M_C} = \frac{V_H{}^2 \rho_H}{V_C{}^2 \rho_C} \tag{6}$$

These flow equations are based on characteristic equations for T-junction intersections found in a report by the Japan Society of Mechanical Engineers [21]. Table 14 provides categorization of T-junction flow, with categories for wall, re-attached, turn and impinging jet as a function of momentum ratio [22]. An illustration detailing the flow pattern of the jet categories is included in Figure 96. Note that the momentum ratio bounds for each flow category is for a T-junction without obstruction immediately following the junction. The experimental geometry used in this work does not match this exactly thus the values given in Table 14 give only an estimate of what the characteristic shape of the jet should be.

Table 14: Categorization of T-junction jet ratio

Flow Category	M_R
Wall jet	>4
Re-attached jet	1.35-4
Turn jet	0.35-1.35
Impinging jet	<0.35

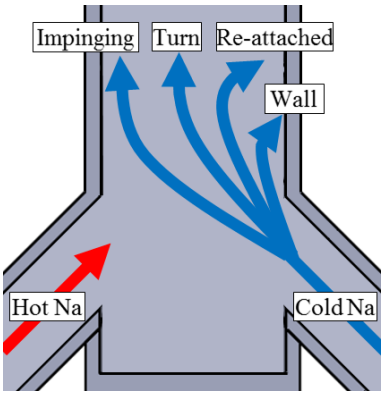

Figure 96: Flow categories illustrated for 90-degree junction

Testing Parameters

Flows which represent impinging, turn, re-attached and wall jets were created to study thermal striping. This was done by varying the hot and cold sodium flow rates to produce momentum ratios which fall in the range of each flow category given in Table 14. The parameters for this experiment, hereby referred to as Experiment 1, are included in Table 15 for reference. For tests 1-8, the temperature differential was kept at a constant gradient of around 75 °C while the

velocity of the hot stream was adjusted. Both the hot and cold streams were kept in the turbulent flow regime in their entry lengths. Test 9 possessed a temperature gradient of 53.4 °C between the hot and cold flows. The momentum ratio was calculated for each flow condition in Table 15. The Reynolds numbers are also calculated for each entry leg using the bulk flow rate. Note that values for density and viscosity of sodium to calculate Reynolds numbers and momentum ratios at a particular temperature can be found in Argonne National Laboratory's report "Thermodynamic and Transport Properties of Sodium Liquid and Vapor" [23].

Table 15: Experiment 1, variable turbulent velocity and constant temperature differential

Test #	T_{hot} [°C]	T_{cold} [°C]	ΔT [°C]	Q_{hot} [L/min]	Q_{cold} [L/min]	Re_{hot} [-]	Re_{cold} [-]	M_R [-]
1	583.1	507.6	75.5	0.700	1.516	5625	11274	0.209
2	584.0	506.7	77.3	1.026	1.516	8257	11263	0.448
3	582.0	508.2	73.8	1.120	1.516	8991	11282	0.534
4	584.0	507.8	76.2	1.213	1.516	9759	11277	0.626
5	583.0	508.0	75.0	1.365	1.516	10968	11279	0.793
6	583.0	508.0	75.0	1.516	1.516	12187	11279	0.979
7	583.0	508.2	74.8	1.936	1.516	15562	11282	1.596
8	576.0	508.2	67.8	2.403	1.516	19185	11282	2.463
9	625.4	572.0	53.4	4.386	0.9214	36593	7329	22.30

The ODiSI-B is only able to sample one fiber at a time. Therefore, the fibers were read sequentially for 10 seconds each. Sampling was done when flow rates and the hot and cold entry stream temperatures reached steady state thus striping conditions for each fiber should be similar. Sampling fibers in parallel is ideal and could be done in the future with additional synchronized fiber interrogator units. The temperature acquisition rate was 23.8 Hz. The Nyquist frequency was then 11.9 Hz. The spacing between optical fiber gauges was 0.653 mm. This acquisition rate and gauge spacing is set by the manufacturer. A faster acquisition rate results in more noise during striping as the system is not able to accurately cross correlate the Rayleigh backscatter peaks in the high temperature gradient region of the thermal striping region. According to literature, frequencies less than 10 Hz dominate the spectral frequency power, thus the thermal striping phenomenon should be adequately captured with the optical fiber sensor [12].

Results

Temperature Range

Two dimensional contour plots showing the maximum range of temperature oscillations seen for tests 1-9 of Experiment 1 have been included in Figure 97. The tests are labeled by their respective momentum ratio. These 2D plots were created from the 1D fiber data by performing a linear interpolation between the data from fibers A1, A2 and A3. This was done by creating a 50 x 110 (x by y) cell mesh with spatial coordinates spanning 2.2 cm in the x direction and 5 cm in the y directions. These dimensions represent the 2.2 cm inner diameter of the mixing tube and the corresponding vertical 5 cm span of the fibers, see Figure 95. The temperature range data was then

linearly interpolated onto the mesh using a "natural" interpolation. Natural interpolation is a triangulation-based natural neighbor interpolation method included with MathWorks' MATLAB software. The region located outside of the mesh where no data is available for interpolation is set to "not a number", or NaN, to avoid affecting the data at the periphery. Note the dotted lines plotted depicting the fiber locations in Figure 97, with each fiber gauge represented by a dot.

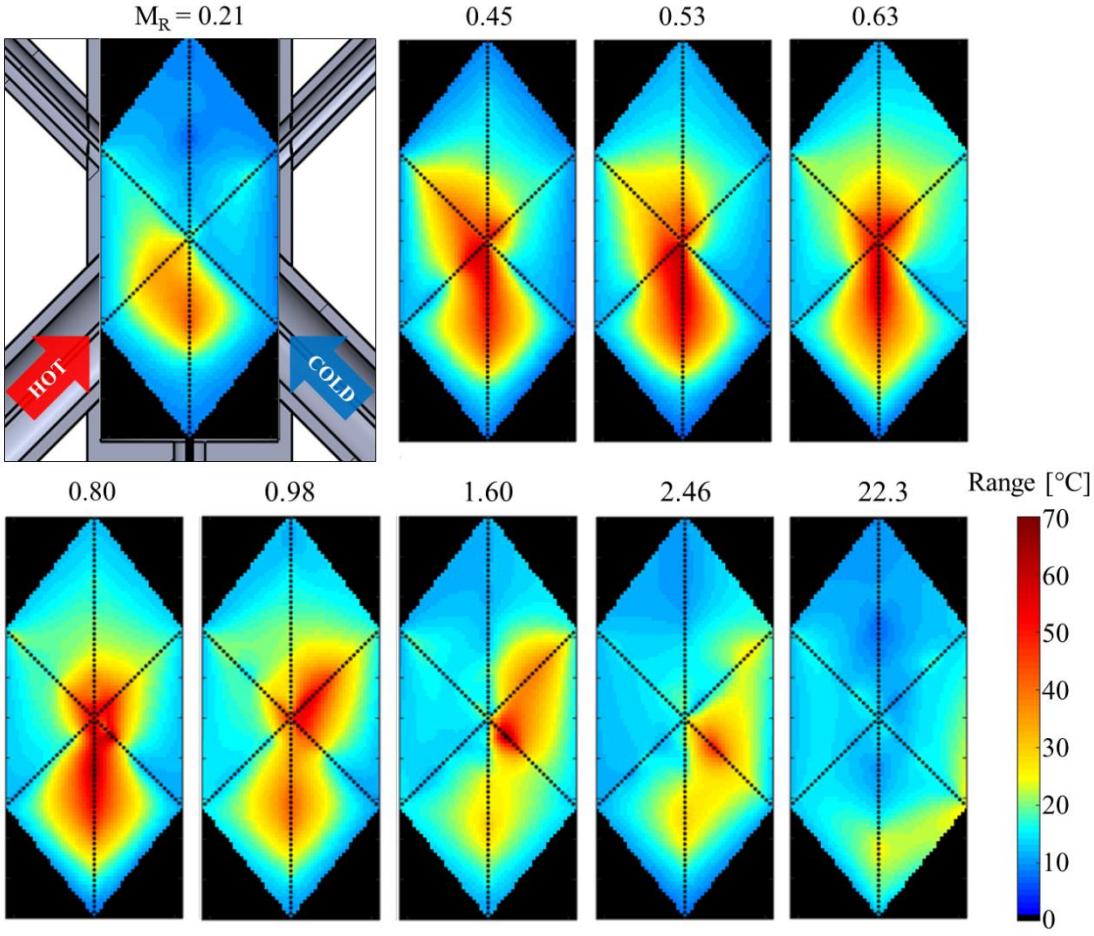

Figure 97: Experiment 1 temperature oscillation range over acquisition period

One can see that a momentum ratio of 0.21 results in large temperature oscillations towards the hot side mixing tube wall. This is representative of the shape of an impinging jet with a momentum ratio less than 0.35, as predicted by Table 14. A lower momentum ratio should produce oscillations even closer to the hot side wall. This flow regime could be characteristic of mechanical failures on the far side of an impinging flow. Thus it would be prudent to perform component inspection on the opposite side of the branch to main tube interface when operating at momentum ratios less than 0.35 for extended periods of time.

The turn jet momentum range is also well represented with Experiment 1's flow parameters. Temperature oscillations occur with maximum intensity near the center of the mixing tube, as seen for momentum ratios from 0.45 to 0.98 in Experiment 1. At a momentum ratio of 0.63 the temperature oscillations are centered in the bulk sodium of the converging junction. If a mechanical component were situated at the tube center this would be cause for concern as thermal oscillation range is quite large. Figure 98 displays the gauge on fiber A1 with maximum standard

deviation and maximum range of temperature readings as a function of momentum ratio. The turn jet region is marked, highlighting that the large temperature oscillations occur in the center for this characteristic flow.

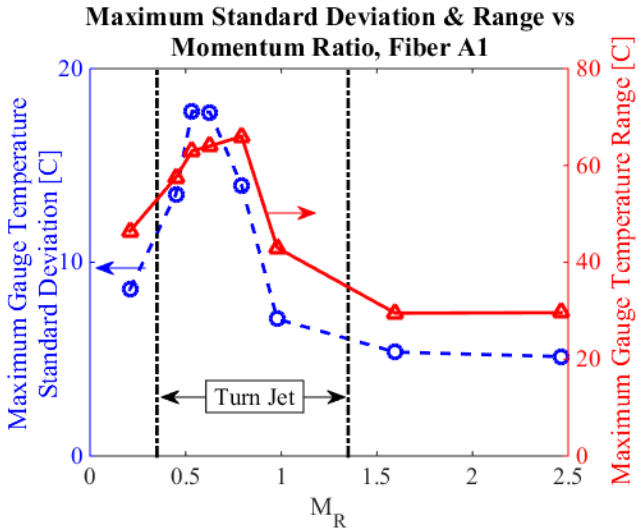

Figure 98: Maximum standard deviation and range vs momentum ratio. Experiment 1 tests 1-8, fiber A1

Looking at the momentum ratios of 1.60 and 2.46, the flow demonstrates the re-attachment behavior on the cold side of the tube with relatively high oscillation range. This flow condition could yield high thermally induced stress downstream of the junction on the cold inlet side. With respect to a momentum ratio of 1.60, one can see in Figure 97 there are temperature oscillations of approximately 30 °C proximal to the mixing tube at a position of around 2.5 entry tube diameters downstream of the entry. If this junction had a weld or other relatively fragile geometry located at this position it could create thermal fatigue and possibly failure.

As the momentum ratio was increased to 22.3 the flow oscillations are constrained to the cold stream wall. While the temperature oscillation range was not as large, possibly due to the lower temperature differential for this particular test, this flow shape is troublesome because the oscillations are centered at the mechanical junction between the inlet and mixing tubes. This is typically a weak area in a system given that a weld is usually located at this location. This weld may be under thermal creep and fatigue stresses from other sources such as thermal expansion of the structure. Oscillations seem to be occurring upstream of the flow inlet, which was also seen by Tanaka et al. in computer simulations of thermal striping at a tee section [24]. Using Eqs. (4-6) one can calculate the momentum ratio in the Tanaka experiment as 19.5. This value is near the experimental momentum ratio of 22.3 categorizing this flow as a wall jet. These oscillations upstream were attributed to intermittent reverse flow from the branch pipe (cold stream) upstream. Thermal fatigue at the upstream edge of the branch pipe should be checked if this were an industrial component.

To determine the temperature differential effect at constant flow rate, additional tests were performed, referred to as Experiment 2. The flow rate of the hot stream was held at 1.283 L/min and the temperature was kept at approximately 600 °C. The flow rate of the cold stream was held at 1.516 L/min and the temperature was varied from 560 °C to 510 °C. These parameters gave a constant momentum ratio of approximately 0.70. The results for Experiment 2 were included in

Figure 99, where contour plots depicting maximum temperature oscillation range have been given. The sodium inlet temperature differential is included in the label for each contour plot. One can see the increase of striping magnitude as the temperature differential increases while the characteristic turn jet shape is maintained. This demonstrates that momentum ratio defines the location of thermal striping oscillations more than the temperature differential between impinging streams.

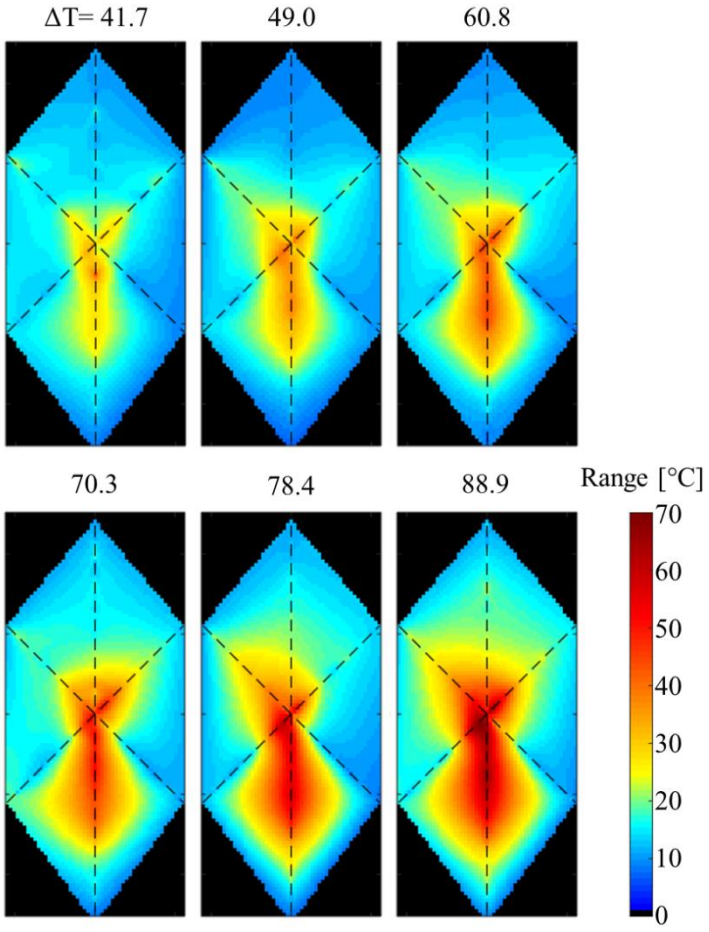

Figure 99: Experiment 2, Constant flow rate, variable inlet temperature differential

Frequency Analysis

It is important to explore the frequency at which thermal striping occurs. A frequency analysis reveals both the number of temperature range cycles over a component lifetime and the effectiveness of heat transfer across the sodium to structural component interface. This effectiveness is dictated by thermal resistance at the sodium to component interface. This resistance buffers high frequency thermal oscillations, thus lower frequency thermal striping behavior is more malignant [14] [18].

To give an example of temperature as a function of time and space in thermal striping, data from Experiment 1, test 4 was explored. The mean temperature was found for each gauge in fiber A1 over the 10 second experiment period. The gauge temperature difference from each gauge's mean was then plotted as a function of time in Figure 100. A periodic nature of temperature oscillation is evident in the data, as it varies from -35 °C to 35 °C from mean at seemingly regular

intervals. The power spectral density (PSD) for fibers A1, A2 and A3 at the location of maximum temperature oscillation for each fiber in test 4 is plotted in Figure 101.

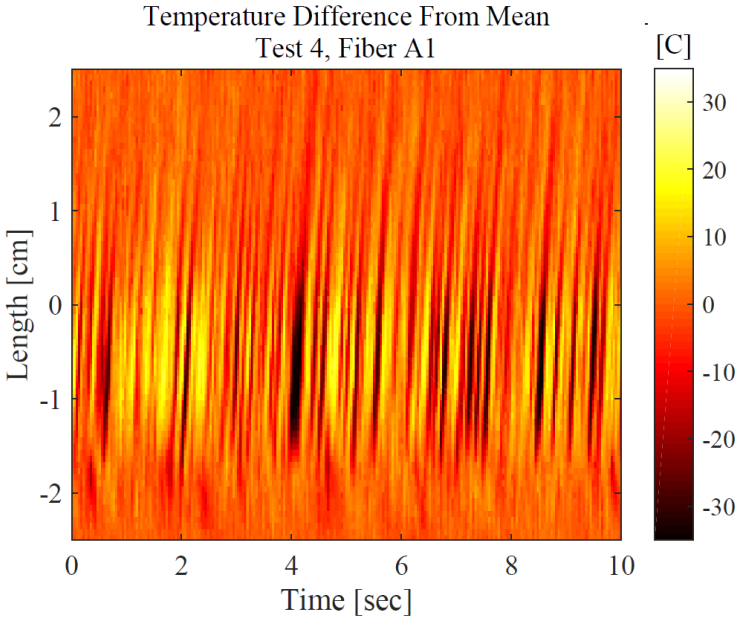

Figure 100: Fiber A1 temperature difference from mean vs length vs time. Experiment 1, test 4.

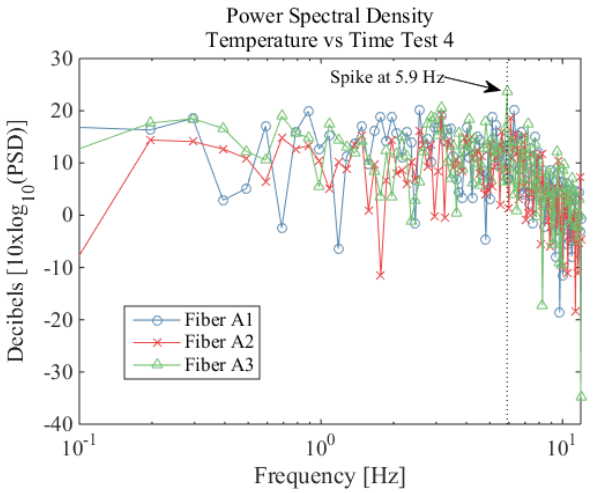

Figure 101: Power spectral density of Fiber A1, A2, and A3. Experiment 1, test 4.

The PSD reveals the power present in the temperature signal as a function of frequency. White noise is apparent from frequencies of 0.1-6 Hz with a drop in spectral power from around 6 Hz to the Nyquist frequency of 11.9 Hz. A spike in spectral power is seen at 5.9 Hz which seems to match the visibly apparent frequency of temperature oscillations of Figure 100. In order to further analyze this, an autocorrelation was performed on the fiber A1 temperature versus time data used in Figure 101. The results of this autocorrelation can be found in Figure 102. Notice that the first non-zero lag amount with a positive peak in correlation is at 0.168 seconds. Calculating the inverse of this yields ~5.9 Hz, which matches the peak in the PSD, as expected. Also notice in Figure 102 that the subsequent positive correlation spikes are multiples of 0.168 seconds and any negative correlation trough is halfway between these peaks. Ogawa et al. also found a prominent

frequency peak at 6 Hz during thermal striping experiments at a tee junction using water for a variety of flow configurations [18].

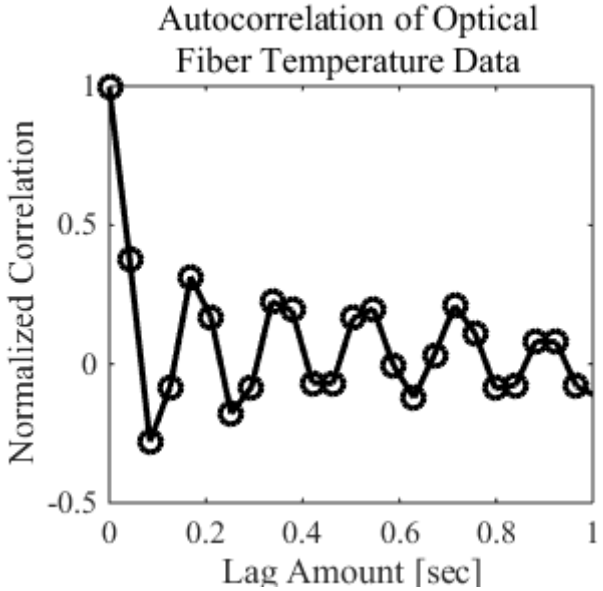

Figure 102: Autocorrelation of optical fiber A1 gauge at maximum temperature oscillations. Experiment 1, test 4.

OPTICAL FIBER CROSS CORRELATION VELOCIMETRY

Introduction

Given the high spatial and temporal resolution of the optical fibers, one can perform cross correlation velocimetry (CCV) on the temperature as a function of time and space to obtain the average flow rate. This technique works by finding the time separation of a distinct temperature pattern between two temperature sensors with cross correlation. Given the sensors are spaced at a known distance in a flow stream the velocity can then be calculated. This technique was developed by Cox in 1977 to study velocity in turbulent flames [25]. It has since been applied successfully to calculate water flow rate in an experimental scale model of a boiling water reactor with an array of thermocouples [26]. The oscillatory nature of the temperature in thermal striping provided a good application for CCV in this work.

Method

The method of cross correlation velocimetry utilizes the transport of a small volume of fluid at a particular temperature by advection across temperature sensors to determine flow rate. To perform CCV analysis a reference temperature gauge is chosen at the origin of a distinct temperature oscillation, in this case the convergence of two flows producing thermal striping. A plot with sample data showing temperature versus time data for fiber A1 at a reference gauge 6.54 mm below the crossing point in **Error! Reference source not found.** and a subsequent gauge at the crossing point is seen in Figure 103. Temperature oscillations produced by thermal striping create a temperature variation which is transported by the bulk sodium flow. Thus one can imagine shifting the downstream gauge data in time over to match the reference gauge to acquire high correlation between the data. This time shift is referred to as “lag” in time series analysis.

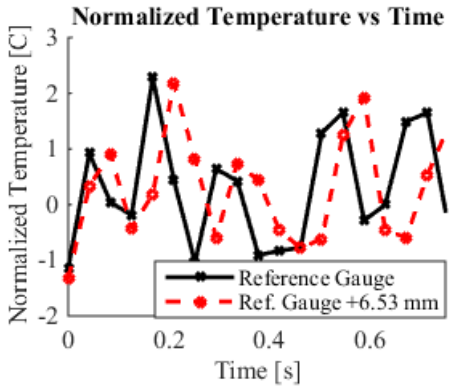

Figure 103: Optical fiber temperature versus time data

This process can be automated using the equation for cross correlation, Eq. (7) [27].

$$C_{12}(\tau) = \frac{1}{P-\tau}\sum_{n=1}^{P-\tau} T1_n T2_{n+\tau} \qquad (7)$$

Where the above variables are defined as:

C_{12}	≡	Cross correlation of gauge 1 to 2
P	≡	Measurement time period
τ	≡	Lag
T1, T2	≡	Temperature measurement at gauge 1 and 2

Thus the correlation values for time lag can be calculated with respect to reference for a series of down-stream gauges, as seen in Figure 104. High correlation can be seen in Figure 104 at particular distances with respect to reference for lag values. The frequency of the optical fiber reading in Figure 104 is 23.8 Hz thus the minimum lag value able to be calculated is 42 milliseconds. The gauge with the highest correlation at a particular lag value can then be used to calculate velocity as the gauge spacing is known.

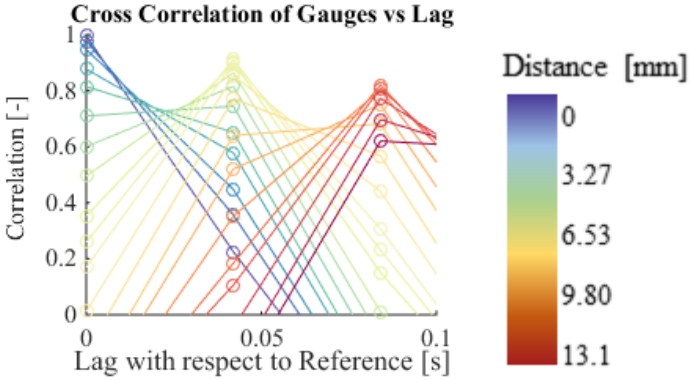

Figure 104: Cross correlation of gauges with respect to reference gauge

Testing Parameters

The parameters used for calculation of sodium flow rate by cross correlation velocimetry are given in Table 16. Temperature data from fiber A1 was used for CCV as it was situated parallel to bulk sodium flow in the mixing tube. The columns of Table 16 contain the electromagnetic flowmeter reading, mixing tube Reynolds number, momentum ratio of the streams, temperature differential of the streams, and percent error of the CCV as compared to the electromagnetic flow

meters. Note that each test was done with the same acquisition rate and period as the flow shape categorization experiment. Note also that all tests from the flow shape categorization experiment were included in calculating the sodium flow rate by CCV, except for test 9 where the momentum ratio of 22.30 characterized the flow as a wall jet thus failing to yield satisfactory oscillation of temperatures near the mixing tube center (location of fiber A1).

Table 16: Cross correlation velocimetry flow parameters

Q [L/min]	Re [-]	M_R [-]	ΔT [C]	Error [%]
0.653	1775	0.98	90.0	6.97
0.653	1799	0.98	75.0	37.23
0.653	1838	0.99	50.0	37.58
0.653	1876	0.99	23.0	31.60
1.286	3438	0.12	90.0	14.25
1.250	4223	0.97	121.0	24.49
1.918	5050	0.97	102.0	15.53
1.918	5129	0.98	85.5	11.70
1.918	5248	0.98	58.0	10.38
1.583	5354	0.41	117.0	5.69
1.918	5369	0.99	31.5	10.26
1.918	5438	1.00	15.5	11.22
1.918	5470	1.00	11.0	10.74
1.917	6489	0.97	123.0	6.02
1.917	6620	0.97	90.0	1.89
2.216	7643	0.21	75.5	20.53
2.542	8769	0.45	77.3	5.79
2.637	9089	0.53	73.8	1.39
2.731	9417	0.63	76.2	3.03
2.800	9661	0.70	88.9	2.13
2.800	9757	0.70	78.3	3.37
2.800	9810	0.70	70.3	4.60
2.800	9901	0.71	49.0	1.15
2.883	9936	0.79	75.0	7.89
2.800	9997	0.71	41.7	4.76
3.034	10459	0.98	75.0	2.80
3.453	11910	1.60	74.8	0.40
3.522	11963	0.62	96.0	9.27
3.708	12653	0.78	96.0	13.21
3.917	13494	0.97	105.0	14.20
3.919	13470	2.46	67.8	5.27

Results

Cross correlation velocimetry was performed on optical fiber A1 temperature data taken throughout the course of this work. All data collected for this work which had momentum ratios less than 4 were used. This ratio provided sufficient oscillatory behavior at the tube center with impinging and turn jet flow characteristics. Wall jets did not provide sufficient oscillations in the center of the mixing tube where the concentrically mounted optical fiber A1 was located. An optical fiber gauge located 10 gauges (6.53 mm) below the cross point labeled in Figure 95 was used as a reference gauge for which subsequent gauges downstream were cross correlated with respect to reference, as described in the methods section previously.

Figure 105 shows the CCV calculated flow rate as a function of the electromagnetic flow meter reading. The flow parameters and associated error of the CCV measurement with respect to the electromagnetic flowmeter can be found in Table 16. Note that a wide range of temperature differentials between the inlet streams were used, from 11 °C to 123 °C. The application of CCV was not the goal when acquiring the data for this work, it was simply an auxiliary feature the oscillating temperature profile of the striping afforded. Thus, a more specific study must be performed to determine optimal flow characteristics to achieve accurate and consistent CCV.

One can see in Table 16 that even at the minimum temperature differential of 11 C there is only a 10.74% error in CCV measurement. Additionally, Reynolds numbers of bulk flow in the mixing tube below the turbulent regime of ~5000 yielded satisfactory CCV results. Using a longer acquisition period for data collection than 10 seconds may help bring down percent error. This work demonstrates that optical fiber temperature sensors may be used to calculate bulk flow rate over a wide range of flow parameters at a junction of two streams at different temperatures.

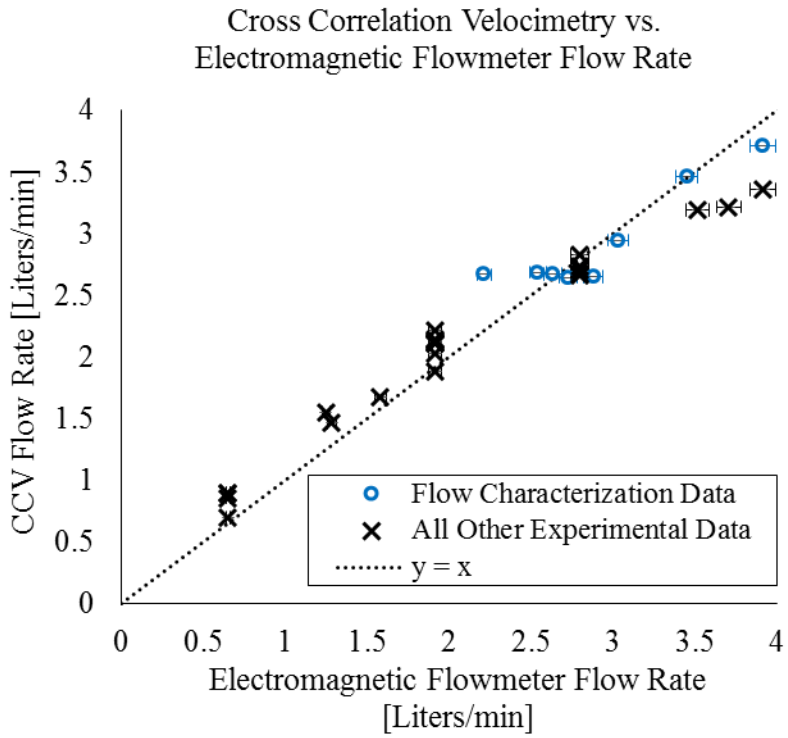

Figure 105: Cross correlation velocimetry flow rate as a function of electromagnetic flow meter reading

REFERENCES

[1] M. G. Hvasta, "Designing and Optimizing a Moving Magnet Pump for Liquid Sodium Systems," PhD Thesis, University of Wisconsin-Madison, 2013.

[2] L. G. Volchkov, "Operation of a Cold Trap for Sodium Impurities," *Atomic Energy,* vol. 35, pp. 1094-1099, 1973.

[3] K. Furukawa, "Liquid Sodium Technology Development," *Journal of Nuclear Science and Technology,* pp. 501-515, 1966.

[4] W. H. Bruggeman, "Purity Control in Sodium-cooled Reactor Systems," *Journal of the American Institute of Chemical Engineering,* pp. 153-156, 1956.

[5] RDT Standard, U.S. Energy Research and Development Administration, "Plugging Temperature Indicator Assembly for Sodium Service," 1975.

[6] B. Nollet, "Electrochemical Oxygen Sensor Development for Liquid Sodium," UW-Madison PhD Thesis, 2013.

[7] R. Thompson, "Testing and Performance of Electrolytic Oxygen Meters for Use in Liquid Sodium," Journal of Nuclear Materials, 1983.

[8] O. J. Foust, Sodium-NaK Engineering Handbook.

[9] R. Hui and M. O'Sullivan, Fiber Optic Measurement Techniques, Burlington: Elsevier, 2009.

[10] D. Samiec, "Distributed Fibre-Optic Temperature and Strain Measurement with Extremely High Spatial Resolution," *Photonik International,* pp. 10-13, 2012.

[11] Wood, "Evaluation of the Performance of Distributed Temperature Measurements with Single Mode Fibe Using Rayleigh Backscatter up to 1000 C," IEEE Sensors Journal, 2014.

[12] I. Jones, "The Frequency Response Model of Thermal Striping for Cylindrical Geometries," *Fatigue & Fracture of Engineering Materials & Structures,* vol. 6, pp. 871-882.

[13] O. Gelineau and M. Sperandio, "Thermal Fluctuation Problems Encountered in LMFBRs," in *Specialistic Meeting on Correlation between Material Properties and Thermohydraulics Conditions in LMFBRs,* Aix-en-Provence, France, 1994.

[14] P. Chellapandi, S. C. Chetal and B. Raj, "Thermal Striping Limits for Components of Sodium Cooled Fast Spectrum Reactors," *Nuclear Engineering and Design,* vol. 239, no. 12, pp. 2754-27656, 2009.

[15] J. E. Brunings, "LMFBR Thermal-Striping Evaluation," Rockwell International, Canoga Park, 1982.

[16] T. Kawamura, K. Shiina, M. Ohtsuka and I. Tanaka, "Experimental Study on Thermal Striping in Mixing Tees With Hot and Cold Water," in *10th International Conference on Nuclear Engineering,* Arlington, 2002.

[17] K. Yuki, H. Hashizume, M. Tanaka and T. Muramatsu, "Investigation of Thermal Hydraulic Mixing Mechanism in T-junction Pipe with a 90-degree Bend in Upstream Side for Mitigation and Controlling of Thermal-striping Phenomena," 2006.

[18] H. Ogawa, M. Igarashi, N. Kimura and H. Kamide, "Experimental Study on Fluid Mixing Phenomena in T-Pipe Junction with Upstream Elbow," in *NURETH-11*, Avignon, 2005.

[19] I. S. Jones and M. Lewis, "A Frequency Response Method for Calculating Stress Intensity Factors due to Thermal Striping Loads," *Fatigue & Fracture of Engineering Materials & Structures,* vol. 17, no. 6, pp. 709-720, 1994.

[20] B. R. Munson, D. F. Young, T. H. Okiishi and W. W. Huebsch, Fundamentals of Fluid Mechanics, Wiley, 2009.

[21] The Japan Society of Mechanical Engineers, "Guideline for Evaluation of High-Cycle Thermal Fatigue of a Pipe," 2003.

[22] S. Qian, J. Frith and N. Nasahara, "Classification of Flow Patterns in Angled T-Junctions for the Evaluation of High Cycle Thermal Fatigue," *Journal of Pressure Vessel Technology,* vol. 137, no. 2, 2014.

[23] J. K. Fink and L. Leibowitz, "Thermodynamic and Transport Properties of Sodium Liquid and Vapor," Reactor Engineering Division Argonne National Laboratory, Lemont, 1995.

[24] M. Tanaka, H. Ohshima and H. Monji, "Thermal Mixing in T-Junction Piping System Related to High-Cycle Thermal Fatigue in Structure," *Journal of Nuclear Science and Technology,* vol. 47, 2010.

[25] G. Cox, "Gas Velocity Measurement in Fires by the Cross-Correlation of Random Thermal Fluctuations," *Combustion and Flame,* vol. 28, pp. 155-163, 1977.

[26] Q. NguyenLe and M. Ishii, "In-Vessel Fluid Flow Measurements Using Thermocouples Cross-Correlation," in *6th International Conference on Nuclear Engineering*, San Diego, 1998.

[27] V. Motevalli, C. Marks and B. McCaffrey, "Cross-Correlation Velocimetry for Measurement of Velocity and Temperature Profiles in Low-Speed, Turbulent, Nonisothermal Flows," *Journal of Heat Transfer,* vol. 114, pp. 331-337, 1992.

[28] R. G. Thompson, "Testing and Performance of Electrolytic Oxygen Meters for Use in Liquid Sodium," *Journal of Nuclear Materials,* p. 115, 1983.